Università degli Studi di Palermo

AREA QUALITÀ, PROGRAMMAZIONE E SUPPORTO STRATEGICO
SETTORE STRATEGIA PER LA RICERCA
U. O. DOTTORATI

Dottorato di Ricerca in Scienze Fisiche e Chimiche

Dipartimento di Fisica e Chimica - Emilio Segrè

Settore Scientifico Disciplinare PHYS-05/A

Radiation and Surface-Driven Evolution of Prebiotic Astrophysical Ices

IL DOTTORE

Rashida Aslam

IL COORDINATORE

Prof. Marco Cannas

IL TUTOR

Prof. Gioacchino Massimo Palma

LA TUTOR

Angela Ciaravella

CICLO XXXVIII

ANNO CONSEGUIMENTO TITOLO 2026

Finanziato dall'Unione europea NextGenerationEU

Ministero dell'Università e della Ricerca

Italiadomani PIANO NAZIONALE DI RIPRESA E RESILIENZA

Contents

Abstract **1**

1 Organic chemistry in space **3**
1.1 The cosmic chemical cycle . . . 3
1.2 Physical landscapes: from molecular clouds to discs . . . 3
1.3 The journey of ices: inheritance versus reprocessing . . . 5
1.4 Composition and evolution of interstellar dust . . . 6
1.5 The volatile reservoir of the icy universe . . . 7
1.6 Synthetic pathways and structural evolution of interstellar icy mantles . . . 9
1.6.1 Structural stratification: the polar and apolar mantle phases . . . 11
1.7 Complex organic molecules . . . 12

2 Experimental methodology and laboratory infrastructure **15**
2.1 Vacuum and Thermal Architecture . . . 15
2.1.1 The LIFE facility . . . 15
2.1.2 The IEPS facility . . . 16
2.1.3 Pre-mixing chamber and gas line system . . . 16
2.2 Detection system . . . 17
2.3 Energetic sources . . . 18
2.3.1 Vacuum-ultraviolet lamp . . . 18
2.3.2 X-ray source . . . 19
2.3.3 Electron gun . . . 20
2.4 Experimental protocols . . . 21
2.4.1 Processes involved in the experiments . . . 23

3 CO line profiles in accreting ices **25**
3.1 Introduction . . . 25
3.2 Experiments . . . 26
3.3 Results . . . 28
3.3.1 Gaussian decomposition . . . 31
3.3.2 Longitudinal modes . . . 35
3.3.3 The CO - CH_3OH interaction . . . 36
3.4 Discussion . . . 38
3.4.1 Mapping concurrent CO environments in astronomical ices . . . 40
3.5 Conclusions . . . 43

A The role of substrate **45**
A.1 The nature of the surface . . . 45
A.2 Experiments . . . 45
A.3 Conclusion and future perspectives . . . 50

4 The chemical architecture of ultraviolet-processed ice mantles **53**
4.1 Non-uniform growth and the energetic processing . . . 53
4.2 Experiments . . . 54
4.3 Results . . . 55
4.4 Impact of ultraviolet irradiation on ice mantle stratification . . . 58

5 Phosphorus activation on icy moons **61**
5.1 The geochemical landscape of Enceladus and the Cassini discovery . . . 61
5.2 The magnetospheric radiation environment . . . 62
5.2.1 Mimas and Tethys . . . 63
5.2.2 Is Enceladus surface a chemical reactor? . . . 64
5.3 Ion and electron radiolysis of Enceladus's surface ice . . . 65
5.4 Experiments . . . 67
5.4.1 Substrate preparation and conditioning . . . 67
5.4.2 Experimental procedure . . . 67
5.5 Results . . . 67

5.5.1 Characterization of pristine Na_3PO_4 . . . 68
5.5.2 Electron irradiation of pristine Na_3PO_4 . . . 69
5.5.3 Deposition of H_2O ice over Na_3PO_4 at various temperatures and irradiation with 1 keV and 2 keV electrons . . . 70
5.5.4 Radiolytic processing and kinetic evolution of mixed H_2O:CO ices on Na_3PO_4 substrates . . . 74
5.5.5 Comparative electron and X-ray radiolysis of interfacial ices on Na_3PO_4 substrates and their thermal evolution . . . 81
5.5.6 Why X-rays exhibit reduced localized chemical efficiency compared to electron bombardment . . . 83
5.6 Conclusions and future developments . . . 85

6 The prebiotic thread: from cosmic ices to the foundations of astrobiology 87
6.1 The continuum of molecular complexity: from molecular clouds to discs . . . 87
6.2 Energetic triggers and the synthesis of prebiotic structure . . . 87
6.3 The phosphorus bottleneck and the habitability of ocean worlds . . . 88
6.4 Final perspectives: the unbroken thread . . . 88

List of Figures

1.1 Schematic diagram indicating the evolution of a protoplanetary disc, starting from the transition from a flared, gas-rich disc to a cleared debris disc. Key processes shown include stellar accretion, far ultraviolet driven photo-evaporation, grain growth and settling, and the eventual formation of an inner cavity that leads to the total dissipation of the primary gas disc.reproduced with permission from Williams and Cecchi-Pestellini (2015). 5

2.1 LIFE chamber of 20 cm diameter and 30 cm height; the pumping system is connected at the bottom of the chamber, with the exception of the getter pump, which is connected to the port between the ion gauge and the X-ray source. The horizontal section of the chamber showing some of the diagnostic instruments and radiation sources is shown on the righthand side. 16

2.2 A sketch of the IEPS UHV experimental setup, in which the energetic electrons source, and the diagnostic systems are indicated. In the right inset some details of the cold finger assembly are reported. 17

2.3 Experimental setup and geometric configurations of the MDHL integrated into the IEPS system. Left: the lamp in operation at a hydrogen pressure of 0.4 mbar; the intense purple glow illustrates the plasma discharge within the quartz tube coupled to the main chamber. Right: schematic representation of the T-type (upper panel) and F-type (lower panel) geometries. The technical dimensions provided correspond to the specific lamp assembly mounted on the IEPS setup. 19

2.4 Emission spectrum of the MDHL installed in the LIFE facility. The dominant peak at 121.6 nm represents the atomic hydrogen Lyman$-\alpha$ line. The structured emission features immediately adjacent to this peak and extending to roughly 165 nm are the Lyman band ($B^1\Sigma_u^+ \rightarrow X^1\Sigma_g^+$) of molecular hydrogen. The secondary cluster of peaks centered near 160 nm represents the Werner band ($C^1\Pi_u \rightarrow X^1\Sigma_g^+$). 20

2.5 Theoretical transmission curve of the 200 nm thick silicon nitride (Si_3N_4) membrane window (density = 3.44 g cm^{-3}) as a function of photon energy (left panel). The sharp features in the curve correspond to the characteristic absorption edges of the membrane's constituent elements, while the overall profile confirms a transmissivity exceeding 80% for the primary energy ranges utilized in the XR 50 NAP source shown in the right panel. 21

2.6 Left panel: photographic layout of the Kimball Physics EFG-7 electron gun. Right: panel normalized spatial intensity distribution of the electron beam; the beam profile was imaged using a fluorescent plate and a CCD camera, demonstrating the homogeneous circular morphology achieved under standard operating conditions (Huang, 2019). 22

2.7 Flow chart diagrams for mode 1. 22

2.8 Flow chart diagrams for mode 2. 22

2.9 Flow chart diagrams for mode 3. 23

2.10 Flow chart diagrams for mode 4. 23

3.1 Normal incidence infrared spectra (black lines) of the CO stretching band at 2138 cm^{-1} for the first 6 experiments listed in Table 3.1, representing mixed ices produced by isothermal co-deposition at 12 K. Blue, red and green curves correspond to the Gaussian components centered to high, intermediate, and low wavenumbers, respectively (see Table 3.2). The spectral resolution is 1 cm^{-1}. . . 29

3.2 Normal incidence infrared spectra (black lines) of the CO stretching band at 2138 cm^{-1} for experiments $7-12$ listed in Table 3.1. The panels are arranged sequentially and correspond to layered ices produced by simultaneous deposition during cooling from 200 K to 12 K. Blue, red, and green curves indicate Gaussian components centered at high, intermediate, and low wavenumbers, respectively (see Table 3.2). Spectral resolution is 1 cm^{-1}. 30

2 Continuation of Figure 2: Normal incidence infrared spectra (black lines) for experiments 13 – 14 listed in Table 3.1. Blue, red, and green curves indicate Gaussian components centered at high, intermediate, and low wavenumbers, respectively (see Table 3.2). Spectral resolution is 1 cm^{-1}. 31

3.3 Normal incidence infrared spectra (black lines) are shown for four distinct ice mixtures, all deposited at a constant temperature of 12 K. Left top panel, CO:CO_2 2:1 ratio (experiment 15); right top panel CO + CH_3OH 2:1 ratio (experiment 16), left bottom panel, CO + CH_3OH 1:2 ratio (experiment 17); right bottom panel, ternary CO + CH_3OH + CO_2 ice mixture 2:1:1 ratio. Colored lines correspond to the various components of Gaussian fits (see Table 3.2), following the color convention of previous figures. The spectral resolution is 1 cm^{-1}. 33

3.4 Infrared spectra of the water dangling hydroxyl (dOH) stretching region centered at approximately $3600 - 3700$ cm^{-1} for experiments 2, 3, 4, and 5. The profiles illustrate the variation in dOH intensity across different ice mixtures; the CO + H_2O + CH_4 mixture (experiment 4) exhibits the most prominent feature, indicating a higher degree of microporosity and a greater number of surface binding sites. 35

3.5 CO stretching absorption band for pure CO ice recorded at oblique (45°, black solid line) and normal (90°, red dashed line) incidence. Left panel: isothermal deposition (mode 1) at a constant temperature of 12 K; right panel: CO ice deposited while the substrate temperature was decreasing (mode 2). Both deposition methods result in spectra that show the $C - O$ stretching absorption band near ~ 2138 cm^{-1}, displaying TO mode and a distinct LO mode at ~ 2143 cm^{-1}. The TO mode intensity is scaled by a factor of ~ 1.3 relative to the oblique incidence spectrum. The spectral resolution is 1 cm^{-1}. 36

3.6 The spectra display the vibrational regions for the C-H stretch (left panels) and the C-O stretch (right panels) of methanol diluted in CO and CO + CO_2 matrices. Panels illustrate concentration and composition effects: top, CO:CH_3OH = 2:1; middle, CO:CH_3OH:CO = 1:2; bottom, CO + CH_3OH + CO_2. 37

3.7 Normalized spectra for the whole set of experiments performed in mode 1 (left panel) and mode 2 (right panel). The vertical dashed black line marks the peak position of pure CO ice. Numbers refer to the experiment list reported in Table 3.1. 40

3.8 Left panels: fitting profiles for the CO ice absorption band toward three astronomical sources, the dense cloud sightlines NIR38 and J110621 (McClure et al., 2023), and the protoplanetary disc HH 48 NE (Bergner et al., 2024). The fit has been performed using the Gaussian decomposition, equation (3.1), based on our laboratory-derived ice components. The original JWST spectra are displayed as thick gray lines, while the total fitting profile (representing the sum of all Gaussian components) is shown as a solid black line. Right panels: individual Gaussian components constituting the total fit; labels identify the specific laboratory and the derived ice environment (the peak) selected by the fitting procedure. 42

A.1 Comparison of infrared absorption spectra for pure CO ices deposited at 10 K. The left column displays experiments performed on the bare ZnSe reference window, while the right column shows the corresponding depositions on the ground meteorite powder. The top panels correspond to mode 1 (direct deposition), and the bottom panels correspond to mode 2. 47

A.2 Spectroscopic profiles of ternary ice mixtures CO, H_2O, and NH_3 across six experimental configurations. The left column illustrates the reference depositions on a bare ZnSe window, and the right column illustrates those on the meteorite powder substrate. The panels are organized by deposition protocol: the top row shows the mixed ices (mode 1), while the middle and bottom rows display the layered configurations (mode 2) with varying initial CO ratios. 48

4.1 Infrared spectroscopic evolution of the ternary H_2O:NH_3:CO (2:1:6) ice mixture during concurrent molecular deposition, cryogenic cooling, and ultraviolet irradiation. The bottom panel displays the calculated integrated band areas for the two primary photoproducts, CO_2 (circles) and OCN^- triangles), following their accretion on the cooling window, under high (filled) and low (empty) deposition pressure regimes. 56

4.2 FTIR spectra of the ternary H_2O:NH_3:CO (2:1:6) ice mixture recorded at 10 K following concurrent cooling, molecular deposition, and ultraviolet irradiation, for two deposition pressure values. 57

4.3 Thermal desorption profiles of the ternary H_2O:NH_3:CO (2:1:6) ice mixture. The top panels show the structural evolution of the FTIR transmission spectra as a function of the increasing temperature, while the bottom panels display the QMS tracks (m/z) corresponding to characteristic molecular fragments of parent species and synthesized photoproducts escaping into the gas phase. 58

4.4 Comparative fractional abundance profiles versus ice thickness for parental species under non-irradiated (left panel) and irradiated (right panel) conditions. Solid lines on the non-irradiated data represent the analytical model developed by Jiménez-Escobar et al. (2024). 59

5.1 Schematic view of the inner magnetosphere of Saturn, illustrating the cold plasma (gas) torus associated with Enceladus, the pickup ion population generated from plume material, the E-ring torus (the doughnut-shaped outermost dust ring of Saturn created directly by Enceladus), and the interchange transport processes responsible for plasma redistribution and energization within the Saturnian system (left panel). The orbits of the major Saturn's moons are displayed in the right panel. 63

5.2 Thermal "Pac-Man" anomalies on the leading hemispheres of Mimas (left) and Tethys (right). The upper panels show thermal maps derived from Cassini observations, highlighting the characteristic wedge-shaped regions produced by the preferential bombardment of high-energy electrons trapped in Saturn's rotating magnetosphere. The lower panels show corresponding visible-light images of the two satellites. 64

5.3 FTIR spectroscopic characterization of pristine Na_3PO_4. The left panel displays the raw absorbance spectra at 300 K and 10 K. Middle and right panels illustrate the multi-peak Gaussian deconvolution used to resolve individual structural and environmental vibrational modes. 68

5.4 FTIR spectra of Na_3PO_4 recorded at different irradiation times (30, 90, 180, 360, 660, 1200, 2100, 3600, 5400, and 10800 s) under 1 keV electron irradiation. (a) Full spectral range ($2000 - 730$ cm^{-1}) showing the temporal evolution of the irradiated samples. (b) Expanded view of the 1800˘1400 cm^{-1} region. Gaussian deconvolution of the spectrum acquired after 10800 s irradiation in the regions (c) $1400 - 1100$ cm^{-1} and (d) 1100˘900 cm^{-1}. Labels indicate vibrational features reported in Table 5.3, highlighting the evolution and redistribution of absorption bands. 69

5.5 Same as in Figure 5.4, but for Na_3PO_4 irradiated with 2 keV electrons. 70

5.6 Comparison between the FTIR spectra of Na_3PO_4 obtained after 3 h of irradiation with 1 keV and 2 keV electrons. 71

5.7 FTIR spectral evolution of H_2O ice overlayers on Na_3PO_4 substrates during 1 keV electron irradiation for a fixed duration of 1 hour, comparing the temperature-dependent behaviors of experiments 5 (11 K), 6 (80 K), 7 (100 K), and 8 (130 K). The profiles illustrate the progressive radiolytic depletion of the parent H_2O matrix alongside the concomitant synthesis of major irradiation products. 72

5.8 Same as for Figure 5.7 for 2 keV electrons and 3 hour irradiation time. 73

5.9 Radiolytic column density evolution of H_2O, and H_2O_2 under 1 KeV (1 hour) and 2 KeV (3 hour) electron irradiation 75

5.10 Temperature-dependent FTIR spectra captured during the systematic TPD warm-up (11 K to 300 K at 2 K/min) of H_2O ice overlayers on Na_3PO_4 substrates following 1 keV and 2 keV electron irradiation. Labels indicates band locations (their assignemnts is in Table 5.4). 75
5.11 Infrared spectra of the unirradiated H_2O:CO ice mixture at 12 K. 77
5.12 FTIR difference spectra of the Na_3PO_4+H_2O:CO matrix taken at progressive intervals during 1 keV electron irradiation at 12 K (both top panels) and during 2 keV electron irradiation at 12 K (both bottom panels). Traces are arranged chronologically from bottom to top, corresponding to exposure times of 15, 30, 60, 90, 120, 180, 240, 360, 540, 900, 1800, 2700, and 3600 seconds. Spectral profiles are plotted as a function of wavenumber (cm^{-1}) after subtracting the initial, unirradiated ice spectrum from each subsequent trace. 77
5.13 Column density evolution of precursor molecules H_2O and CO, and synthesized radiolysis products, CO_2, H_2CO and ·HCO. plotted against electron fluence for 1 keV and 2 keV irradiation regimes. 79
5.14 FTIR spectral evolution ($2000 - 1000$ cm^{-1}) of electron-irradiated H_2O:CO ice during annealing from 20 to 300 K at 20 K intervals. The left and right panels correspond to processing under 1 keV and 2 keV electron bombardment, respectively. 79
5.15 Top panel: FTIR absorbance spectrum of the pristine Na_3PO_4 substrate at 10 K before irradiation; bottom panels: Gaussian decomposition of the two main features. 82
5.16 FTIR absorbance spectrum of the bare Na_3PO_4 substrate at 10 K taken at different times during the irradiation. 83
5.17 FTIR absorbance spectra of a 100 ML H_2O ice mantle deposited on the Na_3PO_4 substrate, recorded at progressive irradiation intervals (10, 30, 90, and 210 minutes). The panels track the structural and chemical evolution of the system across four distinct deposition temperature regimes: 10 K, 80 K, 100 K, and 130 K. 84

List of Tables

1.1 Inventory of interstellar ice species 10
1.2 Inventory of representative interstellar COM and gas-phase abundances 13

2.1 Calculated arrival rates and monolayer formation times at 300 K 15

3.1 List of experiments and ice description. 27
3.2 Gaussian fitting of CO infrared profiles for the set of experiments described in Table 3.1. 32
3.3 Gaussian fitting of methanol vibrational C-H and C-O stretch profiles 39
3.4 Relative contributions of laboratory derived Gaussian components to the astronomical spectral fits 41

A.1 List of experiments and ice description with and without meteorite. 46
A.2 Gaussian fitting of CO infrared profiles for the set of experiments described in Table A.1. 49

4.1 Fit parameters for the accretion of the ternary ice mixture. 54
4.2 Wavenumber peak positions of the major vibrational bands of the ternary H_2O:NH_3:CO (2:1:6) ice mixture at 10 K. 55

5.1 Estimated composition of the bulk oceanic chemical environment in molarity (M). 62
5.2 List of the experiments and corresponding physical parameters. All experiments were performed using a $CaF_2 + Na_3PO_4$ substrate. 67
5.3 Infrared band positions and assignments for pristine and electron-irradiated Na_3PO_4. 71
5.4 FTIR features measured during the warming up of H_2O ice after 1 keV and 2 keV irradiation. 76
5.5 Infrared wavenumber assignments and molecular products identified in mixed H_2O:CO ices overlying Na_3PO_4 after 1 keV and 2 keV electron irradiation. 76
5.6 Infrared band assignments and observed wavenumbers (cm^{-1}) for the H_2O:CO mixture during the warm-up phase. 80
5.7 Comprehensive experimental matrix for the comparative irradiation of ice-substrate systems. 81
5.8 Quantitative transport and energy deposition parameters for electron and X-ray radiolysis. 83

Abstract

The emergence of life from non-living matter remains one of the most profound questions in modern science. Addressing this challenge requires understanding the physical and chemical pathways that connect the molecular inventory of the interstellar medium to the formation of habitable planetary environments. This thesis investigates the role of astrophysical ices within this continuum, combining laboratory astrochemistry, molecular spectroscopy, and planetary science to explore how simple cosmic molecules are processed, transformed, and ultimately incorporated into environments relevant for prebiotic chemistry.

The first part of this work focuses on the evolution of volatile species from molecular clouds to protoplanetary discs. Through infrared spectroscopic investigations of laboratory ice analogues, the structural organization of carbon monoxide and other volatile molecules was characterized under astrophysically relevant conditions. Particular attention was devoted to distinguishing mixed and segregated ice phases and to identifying spectroscopic signatures capable of tracing the thermal and chemical history of icy mantles. These studies demonstrate how the microscopic architecture of interstellar ices influences subsequent chemical evolution, affecting the trapping, mobility, and reactivity of molecules during star and planet formation. While the macroscopic architecture of ice, whether layered or mixed, is a primary driver of chemical evolution, the underlying template upon which these ices condense may also play a significant role. To explore this, we extended our laboratory simulations beyond inert substrates to include the use of ground meteoritic material as a proxy for innterplanetary dust particles. This allowed us to investigate the interfacial dynamics between the mineral surface and the ice mantle, specifically looking for evidence of surface-mediated structural changes that occur during the accretion. Comparative analysis reveals that while CO ice deposited on inert ZnSe at 10 K remains predominantly amorphous, the presence of a meteoritic backbone induces a multi-component infrared profile characterized by a distinct blue-shifted shoulder. We propose that this feature arises from the high rugosity and intrinsic mineralogy of the meteorite, which provide specific adsorption sites that act as a physical template. These sites appear to facilitate a more ordered molecular arrangement than is typically observed on flat, inert surfaces at 10 K, altering the physical architecture of ice mantles. If robustly confirmed, the nature of the condensing surface should be considered when interpreting the high resolution spectroscopic signatures of cold astrophysical environments. The resulting molecular inventory represents the initial reservoir from which comets, planetesimals, and ultimately terrestrial planets inherit their volatile content. The second part of the thesis investigates the effects of energetic processing on astrophysical ice analogues. Using vacuum-ultraviolet photons, X-rays, and energetic electrons, simple ice mixtures were subjected to irradiation conditions representative of interstellar and circumstellar environments. The experiments reveal how ionizing radiation initiates complex non-equilibrium chemistry through molecular dissociation, radical formation, and secondary electron cascades. These processes drive the synthesis of increasingly complex organic species, including key prebiotic intermediates such as formaldehyde and formic acid. Such molecules occupy central positions in reaction networks leading to sugars, amino acids, and other compounds of biological relevance. The results highlight the fundamental role of radiation as a universal driver of molecular complexity in environments where thermal chemistry alone would be severely limited.

The final part of the thesis extends this astrochemical perspective to planetary environments, focusing on the potential habitability of icy ocean worlds. In particular, the interaction between sodium orthophosphate and water ice under electron irradiation was investigated as a model for surface processes occurring on Saturn's moon Enceladus. Phosphorus is widely recognized as one of the principal bottlenecks in origin-of-life scenarios because of its tendency to remain trapped in chemically inert mineral phases. The experiments presented here demonstrate that radiolytically generated hydrogen species can efficiently interact with phosphate-bearing materials, promoting protonation reactions and potentially increasing phosphorus reactivity. These findings suggest that surface irradiation may contribute to overcoming limitations in phosphorus bioavailability, thereby enhancing the prebiotic potential of icy planetary environments.

Taken together, the results presented in this thesis reveal a continuous chemical thread linking the cold molecular clouds of the interstellar medium to the emergence of potentially habitable worlds. The structure of interstellar ices determines the initial conditions for molecular evolution; energetic processing transforms simple species into increasingly complex organic compounds; and planetary surface chemistry may activate essential nutrients required for the

transition from chemistry to biology. By integrating laboratory experiments with astrophysical and planetary contexts, this work contributes to a broader understanding of how molecular complexity develops across cosmic environments and how the fundamental ingredients of life may arise throughout the Universe.

Ultimately, the study of cosmic ices extends beyond the characterization of frozen matter in space. It provides a framework for reconstructing the chemical history that connects stars, planets, and biology, offering insight into the universal processes that may transform simple molecules into living systems.

1. Organic chemistry in space

1.1 The cosmic chemical cycle

The history of matter in the universe is defined by a cycle of birth, evolution, and recycling within the interstellar medium (ISM). Stars form within the gravitationally unstable regions of dense molecular clouds, process material through nuclear fusion, and eventually return heavier elements to the ISM through stellar winds and supernovae. During this cycle, a fraction of the material is incorporated into the formation of planetary systems, creating a reservoir of complex organic molecules (COMs) that may seed habitable worlds. The transition from a purely atomic gas to a chemically diverse molecular population is not uniform across the galaxy. Roughly $10-15\%$ of the Milky Way's disc mass resides in the interstellar matter, concentrated primarily along spiral arms and the galactic plane. Within these regions, dense molecular clouds represent the most chemically active environments. These clouds are composed mostly of H_2 and He, but they contain trace amounts of heavier elements, carbon, nitrogen, oxygen, and sulfur, that are essential for life. An apparent contradiction of astrochemistry is that the conditions most conducive to molecular stability, the deep vacuum and extreme cold of dense clouds, are also those where traditional chemical reactions are most inhibited. At temperatures of 10 to 20 K, reactants lack the kinetic energy necessary to overcome activation barriers. Furthermore, the mean densities of 100 to 10,000 H_2 cm^{-3} in "dense" clouds imply that molecular collisions are exceedingly rare. Under such conditions, gas-phase chemistry is restricted to ion-molecule reactions, which are driven by electrostatic attraction rather than thermal collisions. These reactions are barrierless and follow Langevin kinetics, allowing for the formation of small species containing 2 to 6 atoms (Puzzarini and Alessandrini, 2026). In this regime reaction rates are nearly independent of temperature, depend mainly on polarizability and reduced mass, and every close encounter is assumed to be reactive (capture-limited). However, the driver of much of astrochemistry is cosmic-ray ionization, which maintains a low but persistent ionization fraction that initiates and sustains reactive chemical pathways in otherwise cold and dilute gas (Herbst and Klemperer, 1973).

Many of the molecules discovered towards molecular clouds were found to form in complex gas-phase chemical networks. These networks may contain thousands of reactions. Enormous efforts have been (and continue to be) made in the laboratory and in computational studies to supply accurate rate coefficients and other data required to evaluate the effectiveness of these networks in providing molecular species in the observed abundances. However, it has become increasingly evident that purely gas-phase reaction kinetics are insufficient to account for the diversity and fractional abundances of chemical species observed throughout the ISM. While chemical models may incorporate thousands of gas-phase reactions, these schemes remain fundamentally inadequate, failing to produce interstellar molecules that are at the next level of complexity in large, partly hydrogen-saturated species (i.e., the structure contains three or more H atoms with no carbon–carbon multiple bonds), such as CH_3CH_2OH, CH_3CH_2CN, $(CH_3)_2O$, and CH_3OCHO. However, the discovery of over 300 molecular species in the ISM (McGuire, 2022), including complex organics with more than 12 atoms like fullerenes (C_{60} and C_{70}), indicates that a more efficient mechanism for molecular growth must exist. This mechanism is surface-driven chemistry (Tielens and Hagen, 1982). At temperatures below the freeze-out threshold of most volatiles, atoms and molecules from the gas phase condense onto the surfaces of submicrometer-sized dust grains, primarily amorphous silicates or carbonaceous materials. These grains act as molecular factories, concentrating reactants on a two-dimensional surface where they can migrate and meet through quantum tunneling or thermal diffusion.

In cold clouds, the structure of these ice mantles is not a simple homogeneous mixture. Instead, evidence suggests a layered or segregated morphology (Öberg et al., 2011). Hydrogenation of atomic oxygen, carbon, and nitrogen on the bare grain surface first produces a layer of reduced species: water (H_2O), methane (CH_4), and ammonia (NH_3). As the density increases and the environment becomes more translucent, carbon monoxide (CO) from the gas phase freezes out on top of this polar layer, often accompanied by the formation of methanol through the successive hydrogenation of CO. This stratified description suggests that the chemical evolution of ices is sensitive to the specific physical conditions during their accretion history.

1.2 Physical landscapes: from molecular clouds to discs

The chemical potential of astrophysical ices is activated during the collapse of a molecular cloud core into a protostar. This process transforms a relatively quiescent environment into

one defined by extreme gradients in temperature and radiation. Protoplanetary discs, the circumstellar reservoirs of gas and dust from which planets emerge, represent a transitional stage linking interstellar matter to prebiotic potential.

The journey begins within the vast, cold expanses of giant molecular clouds. These are primarily composed of molecular hydrogen and helium, interspersed with microscopic dust grains that act as the cold surfaces where interstellar ices first form. It is an important to focus on low-to-intermediate mass stars, such as our Sun or even smaller M-dwarfs, when discussing prebiotic chemistry. High-mass stars live fast and die young, often exhausting their fuel in a few million years. This is far too brief for the complex molecular evolution and planet-building processes to reach their full potential. In contrast, stars of lower mass provide a stable, long-lived radiation environment that allows protoplanetary discs to persist for millions of years, giving the chemical potential of astrophysical ices enough time to be refined through the cycles of transport and radiation. For stars like our Sun to emerge, a specific region within these clouds, a molecular cloud core, must become dense enough to overcome its internal thermal pressure. This happens when the core's mass exceeds the Jeans mass, which represents the critical threshold where the inward pull of gravity outweighs the outward push of internal gas pressure, triggering a gravitational collapse (Williams et al., 2017). At this point, gravity becomes the dominant force, and the core begins an irreversible inward collapse. Because these cores are incredibly cold (typically $10-20$ K), the initial chemistry is frozen in, preserving the simple molecules gathered from the interstellar medium.

As the collapse accelerates, the conservation of angular momentum funnels the structural evolution of the system. Even a negligible amount of initial rotation in the cloud core becomes significant as the material draws closer to the center, and the collapsing gas and dust spin up as they fall inward. While gravity pulls material from all directions, the centrifugal force generated by this rotation increasingly resists the collapse along the equator. Material at the poles, however, faces no such resistance and falls directly toward the central protostar. This directional disparity causes the collapsing envelope to flatten into a thin, rotating protoplanetary disc centered around the growing star. Simultaneously, the system must solve a critical physical bottleneck: it has too much spin to allow all the material to land on the star. To shed this excess angular momentum, the system launches bipolar flows. These are high-velocity jets of gas and magnetic fields ejected at immense speeds from the poles of the protostar. These outflows act as a cosmic pressure valve, carving out massive cavities in the remaining cloud envelope and carrying away the rotational energy that would otherwise prevent the star from gaining mass. This transition marks the end of the quiescent phase. As the disc forms, the gravitational energy of the falling material is converted into thermal energy, creating the steep temperature gradients that define the environment. During the process, the system evolves from a Class 0 protostar, which is almost entirely hidden by a thick envelope of falling dust, into a Class II system, where the star is visible and the disc is a stable, high-energy laboratory for chemical complexity (e.g., Williams and Cecchi-Pestellini 2015).

The physical structure of a disc exhibits a complex radial and vertical architecture. In the midplane, the density is at its highest, and the optical depth is sufficient to block most external radiation, allowing ices to persist. However, as one moves vertically toward the disc surface or radially toward the central protostar, the temperature rises and the radiation field intensifies. This causes a phenomenon known as the snow line, where specific molecular species transition between the solid and gas phases. For example, the H_2O ice line occurs where temperatures reach approximately $150-170$ K, while the CO ice line is found in the much colder outer regions of the disc near 20 K. Chemistry in discs is significantly more dynamic than in molecular clouds. Materials are not static; they undergo transport, lofting from the midplane to the irradiated surface and back again. This vertical mixing is driven by turbulence and exchange of angular momentum, exposing ice mantles to radiation doses that are several orders of magnitude higher than those found in the quiescent ISM. Modeling of this transport suggests that grains may experience multiple episodes of condensation, photolysis, and sublimation, a process that progressively refines the molecular complexity of the ice.

As the disk evolves, it loses mass through both stellar accretion and photo-evaporation. As grains grow and settle, they provide less extinction for ultraviolet light, allowing radiation to penetrate more deeply and eventually carve out an inner hole. Once this hole is established, the disc is rapidly dismantled from the inside out by stellar radiation, ultimately leaving behind only the larger grains and planetesimals that characterize a debris disc, the final site of planet

formation.

Figure 1.1 illustrates this evolutionary sequence across four distinct stages. It begins with the initial stable disc phase, showing a flared geometry where material is actively accreting onto the central star while far ultraviolet photons trigger evaporation at the outer edges. As the system evolves, the second stage depicts the thinning of the disc as grains grow in size and settle toward the mid-plane, reducing the overall extinction of ultraviolet light. In the third stage, a clear inner hole appears as photo-evaporation begins to dominate, effectively cutting off the inner disc from its outer mass supply. The final stage represents the resulting debris disc, where the gaseous component has been entirely removed, leaving only a flattened plane of large grains and planetesimals surrounding the star.

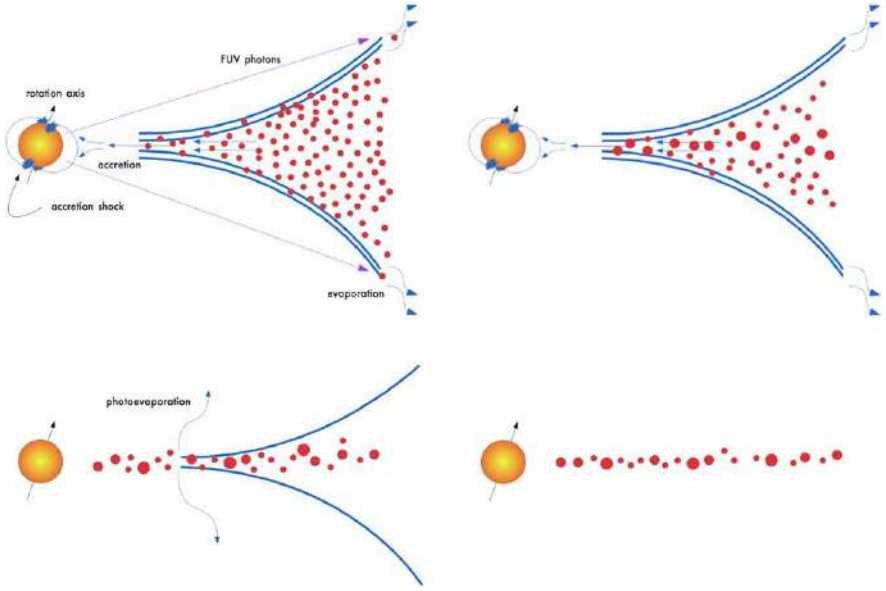

Figure 1.1: Schematic diagram indicating the evolution of a protoplanetary disc, starting from the transition from a flared, gas-rich disc to a cleared debris disc. Key processes shown include stellar accretion, far ultraviolet driven photo-evaporation, grain growth and settling, and the eventual formation of an inner cavity that leads to the total dissipation of the primary gas disc.reproduced with permission from Williams and Cecchi-Pestellini (2015).

1.3 The journey of ices: inheritance versus reprocessing

An important debate in modern astrochemistry is whether the molecular inventory of a planetary system is inherited from the parent cloud or reprocessed (destroyed and reformed) within the disc. The implications of this question are profound for astrobiology: if molecules are inherited, then the building blocks of life are likely universal and present in every star-forming region; if they are reprocessed, then the chemical state of a new planet depends entirely on the unique history of its host disc.

Recent observations of heavy water (D_2O) in the disc of the young star V883 Ori (Leemker et al., 2025) have provided the first direct evidence for water's interstellar journey. Violent shocks and episodic accretion outbursts from young stars can destroy heavy water, causing it to reform as regular H_2O with a lower deuteration ratio. However, the high D_2O/H_2O ratio observed in V883 Ori is consistent with values seen in protostellar envelopes and comets. This indicates that water molecules can survive the transition from a cold molecular cloud to a planet-forming disc unchanged and intact. This inheritance model extends to complex organics as well. The *James Webb Space Telescope (JWST) Ice Age* project has detected a diverse inventory of ices in the darkest regions of molecular clouds, including methanol, ethanol, and potentially acetaldehyde (McClure et al., 2023). The similarity between these ice inventories and the molecular composition of comets like 67P/Churyumov-Gerasimenko, within a factor of 5, suggests that cometary COMs are inherited from the early protostellar phases.

As planetesimals and pebbles aggregate into larger bodies, they carry this inherited inventory into the terminal stage of the journey: the formation of moons and planets. In the outer

Solar System, the circumplanetary discs of giant planets like Jupiter and Saturn acted as sub-reservoirs, capturing icy grains from the wider protosolar nebula. Models indicate that nearly half of the icy material that built moons like Europa, Ganymede, and Callisto may have delivered freshly made COMs from the interstellar cloud without chemical destruction (Mousis et al., 2026). Consequently, these planetary bodies did not originate as chemically pristine entities; rather, they inherited a foundational inventory of prebiotic constituents during their formative stages. The simulations point to something even more intriguing. Some complex organic molecules may have formed not only far from Jupiter, but also closer to the planet itself. Instead of a single delivery route, there may have been a steady supply line operating on more than one front. The idea that these molecules could survive the trip is crucial. Space is not gentle, and radiation and heat can easily break apart fragile compounds. Yet the models show that a significant fraction of icy grains likely preserved their newly formed organics as they migrated inward.

Can we trace such chemical and structural history? The evolutionary pathway of astrophysical ices may be encoded in the subtle variations of their infrared absorption spectra. High-resolution spectroscopy allows for the analysis of band profiles, which serve as chemical fingerprints of the physical conditions experienced by the ice during its evolution. The position, width, and overall shape of an absorption feature are sensitive to the molecular environment, the phase of the ice, and the thermal history of the grains.

1.4 Composition and evolution of interstellar dust

The transition from a purely atomic primordial gas to the chemically diverse and structurally complex universe observed today is fundamentally mediated by the presence of interstellar dust. Although dust constitutes a mere 1% of the total mass of the ISM, it serves as the essential catalytic substrate for complex chemistry and the primary regulator of the physical conditions within molecular clouds. Interstellar dust is not a static population of particles; rather, it is a dynamic component that undergoes a continuous cycle of birth in stellar outflows, processing in the diffuse ISM, and sequestration within the dense interiors of molecular clouds, where it ultimately facilitates the formation of new stars and planetary systems (Williams and Cecchi-Pestellini, 2015).

Interstellar dust grains originate primarily in the dense, relatively cool atmospheres of red giant stars, particularly those on the Asymptotic Giant Branch (AGB), and in the high-energy environments of supernova explosions. In these circumstellar shells, temperatures and densities are sufficient for the condensation of refractory elements into solid particles (Gail and Sedlmayr, 2013). The chemical composition of the newly formed dust is strictly governed by the carbon-to-oxygen (C/O) ratio in the progenitor star's atmosphere. In oxygen-rich environments, $C/O < 1$, the high bond energy of the CO molecule ensures that nearly all carbon is locked in the gas phase, leaving excess oxygen to react with silicon, magnesium, and iron to form silicate grains. Conversely, in carbon-rich environments ($C/O > 1$), the excess carbon leads to the formation of carbonaceous grains, including amorphous carbon, graphite, and polycyclic aromatic hydrocarbons (PAHs). The nucleation of these grains often begins with highly refractory seeds. Theoretical models and spectroscopic observations suggest that oxides such as titanium dioxide (TiO_2) and aluminum oxide (Al_2O_3) are the first to condense, providing the surfaces upon which silicate mantles subsequently grow. As these particles are expelled into the ISM by radiation pressure and stellar winds, they enter a long period of processing, in which they undergo a cycle of destruction and reformation. In the diffuse ISM, grains are subjected to ultraviolet radiation, cosmic ray bombardment, and high-velocity shocks from supernovae. These processes can shatter large grains into smaller fragments or remove atoms through sputtering, leading to a size distribution that ranges from sub-nanometer macromolecules to micron-sized particles. Since the rate at which dust is destroyed by sputtering and grain-grain collisions in supernova-driven shock waves far exceeds the rate at which stars can produce new grains, it is very likely that less than 10% of the dust mass responsible for interstellar extinction is "true stardust" that survived the journey from a stellar atmosphere (Draine, 2011). The remaining 90% must be grown directly within the ISM through the accretion of gas-phase atoms onto surviving seed cores. This suggests that the dust grains eventually incorporated into the molecular cloud collapse are not merely stellar relics, but are largely ISM-grown products, chemically reprocessed and re-condensed in the cold, dense phases of the medium. This continuous recycling ensures that the dust entering the protoplanetary disc carries a complex history of both stellar

heritage and local interstellar growth.

The presence of dust is most readily inferred through its interaction with electromagnetic radiation. Dust grains effectively scatter and absorb starlight, particularly at short wavelengths, a phenomenon known as interstellar extinction. This wavelength-selective extinction causes the light from distant stars to appear redder than its intrinsic color, providing an important diagnostic of dust properties known as interstellar reddening (Cecchi-Pestellini et al., 2012). When we relate this process to the physical properties of the dust grains, the optical depth is defined as the integral of the extinction cross-section along the line of sight

$$\tau_\lambda = \int n_d \sigma_\lambda ds \tag{1.1}$$

where n_d is the number density of the grains and σ_λ is the extinction cross-section, that is a function of the grain's physical size, its shape, and its chemical composition, specifically the complex refractive index of the material. In astronomy, the extinction $A(\lambda)$ is measured in magnitudes, whereas the optical depth τ_λ is a dimensionless quantity that describes the opacity of the path. They are linked by the linear relationship $A_\lambda = 1.086\ \tau_\lambda$. This constant, 1.086, arises from the conversion between the natural logarithm (base e) used in the definition of optical depth (the Beer-Lambert law), and the common logarithm (base 10) used in the magnitude system.

The dimensionless parameter $R_V = A_V/(A_B - A_V)$, called the total-to-selective extinction ratio, is given by the increase in optical depth at visual wavelengths, V (0.55 μm), relative to blue wavelengths, B (0.44 μm). When the physical size of a dust grain is approximately equal to the wavelength of the incident light, the extinction efficiency reaches its peak. This occurs because the grain is large enough to intercept the light wave effectively but small enough to cause significant wave interference and scattering. In the diffuse interstellar medium, most grains are small, making them highly effective at scattering the shorter wavelengths of blue light, while being relatively transparent to the longer wavelengths of visual light. As grains migrate into dense molecular clouds, they undergo coagulation and the accretion of icy mantles, causing their radii to grow. As these grains increase in size, they begin to exceed the wavelengths of visible light. In this regime, the grains become gray absorbers; they block both blue and visual light with similar efficiency. Mathematically, this causes the difference $(A_B - A_V)$ to shrink relative to the total extinction A_V. In diffuse regions, R_V typically clusters around 3.1, whereas in dense molecular clouds, R_V can exceed 5.0, signaling the increase of the average dust size.

The structural morphology of dust is equally significant. Rather than being solid spheres, interstellar grains are often described as porous, fluffy aggregates with large surface-to-volume ratios. This irregular structure is a critical factor in their chemical efficiency. A grain with a high degree of porosity provides a significantly larger surface area, by factors of several hundred, compared to a compact sphere of the same mass. This increased surface area enhances the rate at which gas-phase atoms and molecules can be adsorbed, providing more sites for the complex chemical reactions that drive molecular evolution. The most fundamental chemical reaction in the universe, the formation of molecular hydrogen, is essentially impossible in the gas phase under the conditions prevalent in the ISM. When two neutral hydrogen atoms collide in the gas phase, the release of the binding energy (≈ 4.5 eV) cannot be efficiently dissipated, leading to the immediate dissociation of the nascent molecule. Dust grains resolve this bottleneck by acting as a third body that absorbs the excess reaction energy, thereby stabilizing the H_2 molecule (Gould and Salpeter, 1963). In addition to catalyzing H_2 formation, these grains serve as the primary substrates for the accumulation of astrophysical ices in cold, dense regions. Molecules and atoms from the gas phase collide with the dust and (if they can) stick, forming a thin, solid mantle. The high surface-to-volume ratio of porous grains is especially crucial here; it allows for the rapid growth of these ice layers, which eventually constitute a significant fraction of the grain's total mass. The accumulation of astrophysical ices is a sequential process governed by the specific sublimation temperatures of various volatile species. Rather than a single event occurring at a universal temperature, ice formation represents a dynamic equilibrium between the density of the gas phase and the thermal energy of the dust grain surface.

1.5 The volatile reservoir of the icy universe

In the dense, well-shielded regions of molecular clouds and the cold midplanes of protoplanetary discs, the temperature drops below the freeze-out threshold of most volatile species, typically

between 10 and 20 K. Under these conditions, atoms and molecules from the gas phase condense onto the surfaces of dust grains to form astrophysical ices. These ice mantles are not merely passive accumulations of frozen gas; they are the primary sites of molecular growth and the repository of the universe's volatile inventory (Boogert et al., 2015).

The study of interstellar ices relies almost exclusively on infrared absorption spectroscopy. As infrared light from a background star or an embedded Young Stellar Object (YSO) passes through the dust and ice of a molecular cloud, the vibrational modes of the molecules within the ice absorb specific wavelengths of light. These absorption features provide a unique chemical fingerprint of the ice composition. A tremendous amount of information is contained within the ice band profiles, the exact peak position, full width at half maximum (FWHM), and overall shape of a band. Laboratory experiments play a critical role in the analysis of these observations. By simulating the conditions of space, extremely low temperatures and high vacuum, it is possible to create ice analogs and measure their spectroscopic properties. These laboratory data allow for the decomposition of observed spectra into their constituent molecular components and the determination of column densities through the use of integrated band strengths (or A-values).

The study of interstellar and protostellar ices has undergone a fundamental transition since the successful commissioning and deployment of JWST. The recent results from e.g., the early release science program *JWST Ice Age* (McClure et al., 2023) and the *JWST Observations of Young Protostars* collaboration (van Dishoeck et al., 2025) have provided an unprecedented glimpse into this critical stage of ice evolution, revealing a chemical complexity that far exceeds the findings of previous infrared facilities such as Spitzer or AKARI. The sensitivity and spectral resolution of JWST's instrument suite, particularly the Near-Infrared Camera (NIRCam), the Near-Infrared Spectrograph (NIRSpec), and the Mid-Infrared Instrument (MIRI), have redefined the boundaries of astrochemistry. Where previous telescopes were limited to observing only a few lines of sight toward the brightest infrared sources, JWST can now probe highly extinguished environments, $A_V > 50-100$ mag and map ice distributions across entire molecular cloud cores. The Medium Resolution Spectroscopy (MRS) of MIRI covers the $4.9-28$ μm range with a resolving power ($R \sim 1300-3700$) that is significantly superior to that of the Spitzer Infrared Spectrograph ($R \sim 60-600$). This jump in resolution allows for the identification of individual ice absorption bands that were previously blended.

The major ice species that constitute the bulk of grain mantles, water, carbon dioxide, and carbon monoxide, are ubiquitously and securely detected across all studied environments, from dense clouds to protoplanetary discs. These primary components are typically accompanied by simple hydrides such as ammonia and methane, which form during the early hydrogenation of atoms on grain surfaces. The identification of isotopologues, specifically $^{13}CO_2$ and ^{13}CO, has been significantly advanced by high-sensitivity observations toward pre-stellar cores, dense regions prior to star formation (McClure et al., 2023). Because these ^{13}C features do not suffer from the spectral saturation common in their ^{12}C counterparts, they provide a more reliable means of calculating total column densities. Furthermore, they serve as critical probes for carbon fractionation, allowing for a direct comparison between isotope ratios in the solid phase and those found in the gas phase or local interstellar medium. The census of ionic and sulfur-bearing molecules has recently been consolidated, offering new insights into the energetic processing of ices. The cyanate anion (OCN^-) and carbonyl sulfide (OCS) have been securely identified in dense, quiescent environments for the first time, suggesting that complex sulfur and nitrogen chemistry begins even before protostellar heating occurs. Additionally, nitrous oxide (N_2O) has been detected in some protostellar envelopes via its characteristic N–N stretch band at $4.44-4.47$ μm (Karteyeva et al., 2026). The presence of these species is pivotal for understanding the missing sulfur and nitrogen budgets in the ISM, as they represent a significant solid-state reservoir for these elements. Methanol (CH_3OH) remains the only securely detected COM across nearly all sources. As the simplest COM formed via the sequential hydrogenation of CO, it acts as the primary benchmark for grain-surface chemistry and a precursor to more intricate prebiotic species.

In the more dynamic environment of protoplanetary discs, the chemical inventory becomes a reflection of radial and vertical transport. Recent observations have successfully mapped the major ice components alongside multiple weaker signatures from less abundant species including NH_3, OCN, and OCS (Sturm et al., 2023). Interestingly, the first-time detection of $^{13}CO_2$ in a disc environment highlights the ability of modern observatories to trace isotopic heritage from

the parent cloud into the building blocks of future planetary systems. This continuity suggests that the fundamental chemical stratified structure established in the pre-stellar phase might survives, albeit reprocessed, into the planet-forming stage.

The high sensitivity of MIRI-MRS has opened the door for the identification of COMs larger than methanol. In low- and high-mass protostellar systems, Rocha et al. (2024) reported statistically robust detections for ethanol (CH_3CH_2OH), methyl formate (CH_3OCHO), and acetaldehyde (CH_3CHO). Acetic acid (CH_3COOH) has also been reported as a likely detection. Ambiguity remains for several species where spectral features are either too weak to isolate or are significantly blended with stronger features. Sulfur dioxide (SO_2) is a prime example; while it has been tentatively reported in several sources, the stretching mode near $7.3-7.6$ μm is weak and blended with the strong CH_4 band, making its column density highly dependent on baseline choice. Similarly, formaldehyde (H_2CO), formic acid (HCOOH), and formamide (NH_2CHO) are often reported as tentative because they typically contribute only to one or two minor features that may be degenerate with other species. An additional class of absorbers is represented by organic refractory materials, i.e., complex macromolecular residues formed through the irradiation of simpler ice mixtures. These species are responsible for broad absorption features spanning the $5.5-11$ μm spectral region and have been suggested to contribute up to 10% of the total absorption in selected sources. Their precise molecular composition remains poorly constrained, owing to the absence of distinct and well-defined spectral features.

Determining the relative abundances of ice species is a primary goal of the JWST missions, as these values represent the starting conditions for planetary volatile inventories. Abundances are typically normalized to water ice, with the abundance of water usually set to 100. In the quiescent regions of the Chamaeleon I molecular cloud, JWST has revealed a remarkably consistent baseline composition despite variations in total extinction. Toward the background stars NIR38 and J110621, the abundances of CO and CO_2 are high, reflecting the cold, dense conditions of the cloud. The ice abundances in these regions are similar to those found in even more obscured sources, suggesting that once a certain extinction threshold is reached, the ice chemistry stabilizes.

Most ice features in molecular clouds are broad, a characteristic of the amorphous (disordered) structure typical of ices formed at temperatures below 20 K. The 3.0 μm H_2O band is famously broad due to the large range of hydrogen-bonding environments within the amorphous matrix. Similarly, the broad 4.27 μm profile of CO is used to infer the growth of icy grains to micron-sized radii, as scattering from larger grains produces excess absorption in the line wings. In edge-on discs, these broad profiles are further modified by radiative transfer effects and scattering. The profiles observed toward the HH 48 NE disc, for example, show evidence for grain settling and the entrapment of volatiles, which can broaden the features and shift their peak positions relative to pristine cloud ices. Narrow features or sharp peaks within broader bands are diagnostic of a high degree of ordering or the presence of pure, segregated ice phases. The most distinct example is the 15.2 μm bending mode of CO_2. In cold environments, this band is broad and single-peaked, but as the ice is heated and CO_2 segregates into pure crystalline clusters, the profile splits into two sharp, distinct peaks. JWST has also detected a sharp short-wavelength peak at 4.38 μm in the $^{13}CO_2$ asymmetric stretch, which is attributed to segregated pure CO_2 ice. These narrow features are essential probes of the thermal history of the ice, as the transition from amorphous to crystalline structure occurs at specific temperature thresholds. Furthermore, some COMs like methyl formate and ethanol exhibit relatively narrow fingerprint bands in the $7-8$ μm range, which allows for their identification despite the complexity of the region. One of the greatest challenges in profile analysis is the blending of features. The 7.7 μm region is notoriously difficult because the narrow CH_4 peak is surrounded by broader contributions from SO_2 and OCN^-. Accurate baseline estimation is critical here; small changes in the assumed continuum can lead to significant variations in the derived column densities for the weaker components like SO_2. The inability to isolate a clean profile for H_2S at 3.9 μm is a major reason for its continued status as an elusive sulfur reservoir. Table 1.1 summarizes the key ice species detected to date, their classification, observed environments, and spectral characteristics based on the most recent JWST findings.

1.6 Synthetic pathways and structural evolution of interstellar icy mantles

The emergence of molecular complexity in the ISM is fundamentally based on the catalytic and protective roles of dust grains. While gas-phase chemistry contributes significantly to the

Table 1.1: Inventory of interstellar ice species

ice species		band/μm (cm^{-1})[a]	vibrational mode	status	environment	profile type	abundance[b]
water	H_2O	3.07 (3257), 6.02 (1660)	O-H stretch, H-O-H bend	secure	polar[c] / bulk mantle	broad (amorphous)	100
carbon monoxide	CO	4.67 (2141)	C≡O stretch	secure	apolar / CO-rich	narrow (pure) + broad (mix)	$15-45$
carbon dioxide	CO_2	4.27 (2342), 15.2 (658)	asym. stretch (ν_3), bend (ν_2)	secure	polar and apolar	mix / pure (split[d])	$13-35$
ammonia	NH_3	2.96 (3378), 9.0 (1111)	N-H stretch, umbrella (ν_2)	secure	polar (water-rich)	broad	$5-11$
methane	CH_4	3.32 (3012), 7.7 (1299)	stretching (ν_3), bending (ν_4)	secure	polar	narrow peak	$1.6-5.5$
methanol	CH_3OH	3.53 (2833), 9.6 (1042)	CH_3 sym. stretch, C-O stretch	secure	polar (hydrogenated)	medium	$4-9$
cyanate ion	OCN^-	4.62 (2165), 7.6 (1316)	C≡N stretch, C−O stretch	secure	energetically processed[e]	medium	$0.1-0.5$
carbonyl sulfide	OCS	4.90 (2041)	C=O stretch (ν_3)	likely	apolar / mix	narrow	$0.1-0.2$
ammonium ion	NH_4^+	6.85 (1460)	asymmetric bending (ν_4)	secure	ionic[f] / polar	broad[g]	$4-5$
nitrous oxide	N_2O	4.45 (2247)	asymmetric stretch (ν_3)	tentative	apolar (CO/CO_2 matrix)	narrow	$0.1-0.5$
ethanol	CH_3CH_2OH	7.01 (1427), 7.47 (1339)	CH_2 (ν_5) + CH_3 (ν_{10}, ν_{11}) def.	likely	mix (COM-rich)	narrow/complex	$0.3-0.6$
methyl formate	CH_3OCHO	7.75 (1290)	C-O stretch, CH_3 rock	tentative	mix	narrow	≈ 0.5
acetaldehyde	CH_3CHO	7.23 (1383)	CH_3 def.	tentative	mix	narrow	≈ 0.4
sulfur dioxide	SO_2	7.60 (1316)	asymmetric stretch (ν_3)	tentative	mix	broad/blended	$0.2-1.2$
acetic acid	CH_3COOH	6.83 (1464), 6.89 (1451)	CH_3 def., C-H bend	tentative	mix	narrow/blended	trace
carbon dioxide	$^{13}CO_2$	4.38 (2283)	asymmetric stretch (ν_3)	secure	mix / pure	sharp peak	$1.1-1.5$
formic acid	HCOOH	7.25 (1379)	C-H bend + C-O stretch	likely	polar	broad/blended	≈ 1.4

[a] band positions refer to typical laboratory values for astrophysical amorphous ice analogs at $10-15$ K; [b] abundances are given as a percentage relative to water ice, where $N(H_2O)$ is normalized to 100; [c] polar environments are H_2O-dominated, forming a strongly hydrogen-bonded matrix; apolar environments are dominated by molecules lacking strong hydrogen bonds, primarily CO or N_2; [d] "split" refers to a band profile that resolves into multiple distinct peaks; this can occur due to overlapping polar/apolar environments; [e] it indicates species primarily formed or altered through irradiation by ultraviolet photons, cosmic rays, or electrons, rather than solely by cold surface atom-addition chemistry; [f] "ionic" indicates that the species exists as part of a charged salt pair (e.g., NH_4^+ pairing with OCN^-) resulting from acid-base proton transfer reactions within the ice matrix; [g] the 6.85 μm feature is often a composite of several species; NH_4^+ is the primary secure contributor.

molecular inventory of diffuse environments, it fails to account for the observed abundances of saturated molecules and complex organic species in the cold, dense regions of molecular clouds. Interstellar grains, composed primarily of amorphous silicates or carbonaceous materials, act as microscopic substrates that facilitate the accretion, diffusion, and reaction of gaseous species. At temperatures as low as 10 K, these grains provide a third body to dissipate the excess energy of exothermic reactions, preventing the immediate dissociation of newly formed bonds. The resulting icy mantles are not homogeneous mixtures but complex, stratified structures whose composition and morphology evolve in tandem with the physical conditions of the cloud.

Water is the dominant constituent of interstellar ice mantles, yet its formation remains a subject of intense laboratory and theoretical investigation. Because gas-phase water synthesis is inefficient at low temperatures, the vast majority of interstellar water is produced directly on the surfaces of dust grains through the sequential hydrogenation of oxygen-bearing precursors. Three primary pathways, the atomic oxygen (O), molecular oxygen (O_2), and ozone (O_3) channels, operate concurrently, with their relative efficiencies determined by the local density and the H/H_2 ratio (e.g., Redondo et al. 2020). In the early stages of cloud collapse, when the gas phase is rich in atomic hydrogen and oxygen, the simplest route to water formation involves successive hydrogen addition to O atoms. The reaction sequence $O + H \rightarrow OH$ followed by $OH + H \rightarrow H_2O$ proceeds without significant activation barriers in the gas phase and remains highly efficient on grain surfaces at 10 K. The hydroxyl radical (OH) is a critical intermediate; it can also react with molecular hydrogen, the most abundant species in the ISM, to form water via $OH + H_2 \rightarrow H_2O + H$. However, this latter reaction possesses a gas-phase activation energy of approximately 5.16 $kcalmol^{-1}$, suggesting that its efficiency on cold grains depends heavily on quantum tunneling or the stabilization provided by the ice matrix. While H_2 in dense cold regions is far more abundant than atomic H, the lack of a chemical barrier makes the atomic H addition route a critical step in the water formation network (Meisner et al., 2017). As the cloud evolves and oxygen atoms combine to form O_2, its hydrogenation channel becomes a major contributor to water synthesis. Laboratory simulations using reflection absorption infrared spectroscopy (RAIRS) have demonstrated that O_2 ice, when bombarded with H atoms at $1 - 28$ K, is efficiently converted into H_2O through a hydrogen peroxide (H_2O_2) intermediate (Ioppolo et al., 2008). Ozone is synthesized on grain surfaces through the reaction $O + O_2 \rightarrow O_3$, which is highly exothermic (≈ -1.48 eV). Hydrogenation of O_3 has been identified as potentially an efficient route for water formation in dense clouds (Mokrane et al., 2009).

1.6.1 Structural stratification: the polar and apolar mantle phases

Interstellar ices are generally not found in a state of homogeneous mixing but are instead stratified into distinct chemical phases. This layering is a direct consequence of the chemical evolution of the surrounding gas and the differing condensation temperatures of various species.

The initial layer of ice, referred to as the polar phase, forms during the early stages of mantle growth in translucent and dense clouds. This phase is dominated by water, but also includes other simple hydrides formed through the hydrogenation of C, N, and O atoms. The high abundance of atomic hydrogen in these regions favors a reducing environment, leading to the synthesis of methane, ammonia (NH_3), and water. This layer is characterized by strong hydrogen bonding and an amorphous structure, often referred to as amorphous solid water (ASW). As the cloud density increases and temperatures drop toward 10 K, carbon monoxide, which is formed efficiently in the gas phase, begins to freeze out rapidly onto the existing polar ice. This CO freeze-out stage marks the transition to the apolar phase, where the ice is dominated by CO, with possible trapped minor volatiles as N_2. Observations toward field stars and protostars consistently reveal the presence of pure or nearly pure CO ice components, providing evidence for this distinct outer layer. The final morphology of the ice—whether it remains strictly layered or becomes partially mixed—depends on the interplay of several kinetic and physical factors: different molecular species cannot simultaneously, thermal diffusion upon warming, radiation-induced mixing (e.g., X-rays, Jiménez-Escobar et al. 2022), and porosity allowing volatile species like CO to penetrate into the water-rich layer, creating a "mixed" environment at the interface.

While water forms the structural backbone of the ice, other simple species are formed concurrently, and incorporated within the polar matrix. Ammonia and methane are formed through the sequential hydrogenation of atomic nitrogen and carbon, respectively. Methane ice

is observed to be strongly correlated with solid H_2O, confirming its formation during the early polar phase. Ammonia synthesis follows the $N \rightarrow NH \rightarrow NH_2 \rightarrow NH_3$ sequence. Computational models (Germain et al., 2022) and laboratory experiments (He et al., 2022) using amorphous water clusters indicate that NH_3 exhibits a broad distribution of binding energies (BE) on ASW surfaces, with adsorption sites predominantly being dangling-oxygen (dO) atoms.

Carbon dioxide is a major component of interstellar ice, but its primary formation mechanism is still debated. While the direct reaction $CO + O \rightarrow CO_2$ has a significant activation barrier ($\sim$ 2970 K in the gas phase), the reaction $CO + OH \rightarrow CO_2 + H$ is considered the most efficient route on grains. This reaction proceeds via a hydroxycarbonyl (HOCO) intermediate (Molpeceres et al., 2025). In polar ices, CO and OH radicals (produced from H_2O photolysis or O hydrogenation) can meet and react to form CO_2. In apolar ices, CO_2 formation is less efficient because the HOCO intermediate requires external energy to overcome stabilization by the CO matrix. This explains why astronomical observations, including those from JWST, find CO_2 primarily in water-rich environments (Molpeceres et al., 2023).

Methanol is the most complex of the simple ices and serves as the cornerstone for the formation of COMs. Its synthesis is inextricably linked to the apolar CO layer (although it can form through OH-mediated reactions of methane, Qasim et al. 2018). The dominant pathway to methanol is the successive addition of H atoms to CO: $CO + H \rightarrow HCO$, $HCO + H \rightarrow H_2CO$ formaldehyde, $H_2CO + H \rightarrow CH_3O$ or CH_2OH, $CH_3O + H \rightarrow CH_3OH$. The first and third steps possess modest activation barriers but are known to proceed via quantum tunneling at 10 K. Experimental evidence confirms that this sequence is efficient enough to produce the observed methanol abundances in dark clouds (Chuang et al., 2016). A significant recent finding is the importance of H-atom abstraction reactions in methanol synthesis. The reaction $CH_3O + H_2CO \rightarrow CH_3OH + HCO$ has been experimentally confirmed to be a dominating final step, contributing $70 - 90\%$ of the methanol formed (Santos et al., 2022). This mechanism is particularly relevant in the bulk of the ice mantle where atomic hydrogen may be scarce, but reactive radicals are generated by radiation.

1.7 Complex organic molecules

The identification of COMs in the ISM represents a transformative achievement in molecular astrophysics, bridging the gap between fundamental astrochemistry and the potential origins of life. Traditionally defined as carbon-containing species possessing at least six atoms, these molecules are no longer viewed as rare anomalies but as ubiquitous constituents of star-forming regions, circumstellar envelopes, and even the diffuse interstellar gas. As of early 2025, the inventory of interstellar and circumstellar molecules has reached 334 distinct species, with a notable acceleration in the discovery of complex organic structures during the 2021–2025 period. This expansion is largely driven by advances in broadband radio-astronomical surveys, which have utilized the unprecedented sensitivity of the Acatama Large Millimeter Array (ALMA) to delve into the chemical richness of high-mass star-forming cores like Sagittarius B2(N).

The significance of COMs extends beyond their mere existence; they serve as critical tracers of the physical evolution of protostellar systems. Their abundances relative to molecular hydrogen or reference species like methanol reflect the interplay between grain-surface synthesis and gas-phase processing. From the saturated alcohols and ethers that dominate the hot cores of massive star formation to the large, unsaturated hydrocarbon rings found in the cold, quiescent gas of the Taurus Molecular Cloud (TMC-1), the chemical diversity of the ISM reveals a universe capable of building significant molecular complexity long before the formation of planetary bodies.

Methanol is the most ubiquitous and abundant COM, serving as a primary precursor for many O-bearing complex species. More complex biogenic molecules like glycolaldehyde (the simplest sugar) and formamide (a precursor for nucleobases) have been detected toward hot cores, the warm envelopes of massive protostars, and hot corinos, their solar-mass counterparts. The primary mechanism for the synthesis of COMs is radical-radical recombination on the surfaces of icy dust grains. This process occurs through a series of steps linked to the physical evolution of the star-forming region (Herbst et al., 2020). Ultraviolet photons and cosmic rays penetrate the ice mantles, dissociating stable molecules like H_2O, CH_3OH, NH_3, and CH_4 into reactive radicals such as OH, CH_3, NH_2, HCO, and CH_3O. In the cold prestellar phase ($\approx$ 10 K), radicals are largely immobile. However, as the protostar begins to form and heat the surrounding material, the mobility of these radicals increases. Migration can occur via thermal

diffusion or through non-thermal mechanisms like quantum tunneling. When two radicals encounter each other on the two-dimensional surface of a grain, they can recombine to form a COM. Because the grain acts as a heat sink, the energy released during the formation of the new chemical bond is dissipated, preventing the molecule from dissociating. Finally, once the grain temperature reaches the sublimation point ($\sim$ 100 K), the COMs are released into the gas phase. Non-thermal desorption mechanisms, such as chemical desorption or ultraviolet-induced photodesorption, can also release molecules into the gas phase at much lower temperatures. In addition, ion-molecule reactions, which are barrierless and efficient at low temperatures, can synthesize small molecules that later freeze onto grains. Furthermore, once COMs are desorbed into the warm gas of a hot core, they can undergo further neutral-neutral reactions to create even more complex species.

Table 1.2: Inventory of representative interstellar COM and gas-phase abundances

Chemical Family	**Representative Molecules**	**Chemical Formula**	**Gas-Phase Abundance**
alcohols	methanol	CH_3OH	$10^{-8} - 10^{-7}$
	ethanol	CH_3CH_2OH	$10^{-9} - 10^{-8}$
	vinyl alcohol	CH_2CHOH	$10^{-11} - 10^{-10}$
	2-methoxyethanol	$CH_3OCH_2CH_2OH$	10^{-11}
ethers	dimethyl Ether	CH_3OCH_3	$10^{-9} - 10^{-8}$
	dimethyl sulfide	CH_3SCH_3	$\sim 10^{-10}$
esters	methyl formate	CH_3OCHO	$10^{-9} - 10^{-8}$
	ethyl formate	C_2H_5OCHO	3.6×10^{-9}
	methyl acetate	CH_3COOCH_3	$10^{-11} - 10^{-10}$
aldehydes	acetaldehyde	CH_3CHO	$10^{-10} - 10^{-9}$
	glycolaldehyde	$HOCH_2CHO$	6×10^{-11}
	propanal	C_2H_5CHO	$10^{-11} - 10^{-10}$
nitriles	methyl cyanide	CH_3CN	$10^{-9} - 10^{-8}$
	ethyl cyanide	C_2H_5CN	$\sim 10^{-9}$
	iso-propyl cyanide	i-C_3H_7CN	1.3×10^{-8}
	n-propyl cyanide	n-C_3H_7CN	1.0×10^{-9}
	benzonitrile	C_6H_5CN	10^{-10}
amides	formamide	NH_2CHO	1.3×10^{-10}
	acetamide	CH_3CONH_2	2.1×10^{-10}
	urea	$(NH_2)_2CO$	$10^{-12} - 10^{-11}$
diols	ethylene glycol	$(CH_2OH)_2$	$10^{-11} - 10^{-10}$
S-bearing	carbonyl sulfide	OCS	$10^{-9} - 10^{-8}$
	methyl mercaptan	CH_3SH	$\sim 10^{-9}$
	ethyl mercaptan	C_2H_5SH	$10^{-10} - 10^{-9}$

The detection of COMs is no longer restricted to the high-temperature hot cores of massive stars. Modern facilities like ALMA and JWST have revealed that COMs are present at nearly every stage of the journey from a molecular cloud to a planetary system (Nazari, 2025). Detections of COMs in cold, starless cores like TMC-1 and Perseus have challenged traditional models that required thermal heating for radical mobility (Scibelli et al., 2024). Thus, gas-phase reactions might also contribute to the chemical inventory (e.g., (Barone et al., 2015)). Methanol and acetaldehyde are detected in up to 100% and 49% of surveyed starless cores, respectively, suggesting that COM synthesis is already well underway before the first star even forms. In these 10 K environments, chemistry is likely driven by non-diffusive processes or tunneling. During the protostellar phase, the chemical complexity reaches its peak. Hot corinos, such as IRAS 16293-2422, exhibit thousands of spectral lines from dozens of complex organic species. Recent JWST observations have also detected COMs in the solid phase (ice) toward protostars, providing the direct evidence that these molecules form in the ice before being sublimated. In more evolved regions as protoplanetary discs, COMs are found in the gas phase through non-thermal desorption from the cold midplane or in the warmer inner regions. Detections in discs including TW Hydrae and V883 Ori have identified species like H_2CO, HC_3N and CH_3OH. The detection of dimethyl ether (CH_3OCH_3) in a planet-forming disc for the first time marks a milestone in tracing the full interstellar journey of complex organics.

The study of COMs and ices is currently undergoing a revolution driven by the synergy of infrared and sub-millimeter observations. While ALMA provides the spatial resolution and sensitivity to detect gaseous COMs on the scale of a few astronomical units, JWST is revealing the solid-state precursors trapped in the ices. This dual approach allows astronomers to track (at least in principle) the evolution of matter from its most primitive form as soot in a stellar wind to its incorporation into the building blocks of a habitable world. The discovery of oxygen-bearing molecules more complex than methanol in protoplanetary discs confirms that the chemical potential of astrophysical ices is sufficient to feed the formation of prebiotic environments across the stars.

In Table 1.2 we report a synthesized overview of representative COMs, their chemical formulas, and their typical gas-phase abundances as identified across diverse interstellar environments. The inclusion of the urea and complex thiols marks a significant shift in astrochemistry toward understanding prebiotic precursors. The observed abundance of acetamide (CH_3CONH_2) in Sgr B2(N), for instance, is only a factor of three lower than formaldehyde, indicating that peptide-bond-forming chemistry is remarkably efficient in high-mass star-forming regions. The rapid discovery of increasingly complex molecular structures, including branched chains and rings, reveals a cosmic chemistry far more sophisticated than previously assumed. These interstellar COMs are primarily forged on the surfaces of dust grains through radical-radical recombination and hydrogenation, only later transitioning into the gas phase via thermal or shock-driven release. This chemical evolution appears largely universal; despite notable nitrogen enrichment in high-mass stars, the fundamental pathways remain remarkably consistent across varying stellar environments. The prevalence of prebiotic precursors like amides and sugars reinforces the inheritance model, suggesting that the organic building blocks of planets and comets are a direct chemical legacy from their parent interstellar clouds.

2. Experimental methodology and laboratory infrastructure

2.1 Vacuum and Thermal Architecture

The primary challenge in simulating interstellar chemistry is the reproduction of the extreme isolation and low temperatures characteristic of molecular clouds and protoplanetary discs. To achieve this, the experiments were housed in two sophisticated Ultra-High Vacuum (UHV) systems: the *Light Irradiation Facility for Exochemistry* (LIFE) and *Interstellar Energetic-Process System* (IEPS).

To accurately simulate the chemical evolution of the interstellar medium (ISM), the experimental environment must achieve Ultra-High Vacuum (UHV) conditions, typically reaching base pressures around 1×10^{-11} mbar. This extreme isolation is necessitated by the Hertz-Knudsen arrival rate, expressed as $Z = P/\sqrt{2\pi m k_B T}$ (m being the molecular mass of a single gas particle), which defines the flux of residual gas molecules striking the sample surface. the arrival rate is directly proportional to pressure but inversely proportional to the square root of both the molecular mass and the temperature. This explains why lighter residual gases have a higher collision frequency at a given pressure compared to heavier contaminants. By assuming a standard surface site density of 1×10^{15} molecules/cm^2 for the formation of a single monolayer (ML), the arrival rate can be directly converted into a contamination growth rate (ML/s). The time elapsed before residual gas species, primarily H_2, H_2O, and CO_2, reaches 1 ML is reported in Table 2.1. As shown in the comparative data, the transition from high vacuum to ultra-high vacuum is the defining factor in sample integrity. These results emphasize that at high-vacuum pressures, the arrival rate of molecules is so high that even a trace amount of residual water or carbon dioxide would encapsulate a thin ice sample within seconds. By suppressing the pressure to UHV levels, this arrival rate is reduced by several orders of magnitude.

Table 2.1: Calculated arrival rates and monolayer formation times at 300 K

Species	**Pressure (mbar)**	Z **(cm^{-2}s^{-1})**	**Growth Rate (ML/s)**	**Time to 1 ML**
H_2	10^{-7}	1.43×10^{14}	1.43×10^{-1}	≈ 7.0 s
H_2O	10^{-7}	4.78×10^{13}	4.78×10^{-2}	≈ 20.9 s
CO_2	10^{-7}	3.06×10^{13}	3.06×10^{-2}	≈ 32.7 s
H_2	10^{-10}	1.43×10^{11}	1.43×10^{-4}	≈ 1.94 h
H_2O	10^{-10}	4.78×10^{10}	4.78×10^{-5}	≈ 5.81 h
CO_2	10^{-10}	3.06×10^{10}	3.06×10^{-5}	≈ 9.08 h

Beyond the kinetic requirements of extreme vacuum, reproducing the thermodynamic environment of interstellar dust grains requires the sample substrate to be maintained at deep cryogenic temperatures, typically near 10 K. In both the LIFE and IEPS facilities, this thermal architecture is implemented using a closed-cycle helium cryostat in thermal contact with the sample holder. Maintaining the substrate at very low temperatures is essential to simulate the interstellar environment and to provide the necessary heat sink for the freeze-out and accretion of dosed gas-phase volatiles into solid ice analogues. At the same time, cryogenic conditions ensure that thermal desorption is effectively suppressed, so that non-thermal processes, such as desorption induced by energetic photons or particles, can be selectively investigated under controlled irradiation or spectroscopic monitoring conditions. The combined action of the UHV pumping stages and cryogenic provides that the resulting ice mixtures remain chemically clean and thermally stable throughout the experimental duty cycle. The cryostat and thermal-control system are described in the following subsections.

2.1.1 The LIFE facility

LIFE includes a cylindrical UHV chamber of 20 cm diameter and 30 cm height (see Figure 2.1). The pumping system consists of a turbomolecular pump (Boc-Edwards Maglev, 450 liters/s) connected to a primary apparatus made of another turbomolecular pump (TXT 76DX, 70 liters/s) backed up by a diaphragm pump (MPV 015, $0.25 - 0.3$ liters/s). A cryogenic pump of 1500 liters/s and a getter pump (Saes D1000, 1000 liters/s for H_2) are also present. The pressure in the chamber is monitored by a Ion Gauge (VG Scientia-IGC3) working in the range $10^{-2} - 10^{-12}$ mbar.

The chamber includes a closed-cycle helium cryostat (ARS DE204SB) which can reach

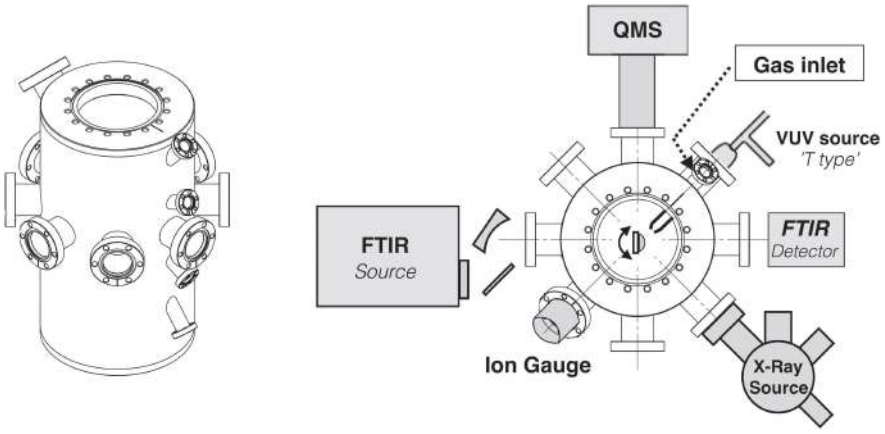

Figure 2.1: LIFE chamber of 20 cm diameter and 30 cm height; the pumping system is connected at the bottom of the chamber, with the exception of the getter pump, which is connected to the port between the ion gauge and the X-ray source. The horizontal section of the chamber showing some of the diagnostic instruments and radiation sources is shown on the righthand side.

temperatures as low as 6 K. At the tip end of the cryostat, an infrared transparent support of 13 mm diameter is placed inside a gold-coated sample holder. The cryostat and the sample holder are surrounded by a cylindrical copper radiation shield. To ensure the best thermal conductivity, an indium layer (purity $> 99.9\%$) is used between the sample holder and the cryostat. The cryostat is mounted on a rotating platform, which allows the sample holder to rotate toward different devices, such as the capillary for gas injection, the radiation sources, and the infrared spectrometer. The temperature is monitored with an accuracy of ± 0.1 K by two silicon diodes, placed along the cryostat and at the sample holder. The cryostat, near the sample, is connected to a Minco HK5321 thermoresistance, which can heat the sample to a fixed temperature while the cryostat is working. A Lake Shore 331 temperature controller connected to the diodes and the tunable thermo-resistance provides the temperature control at the sample.

2.1.2 The IEPS facility

IEPS is an UHV chamber equipped with radiative sources, a pre-mixing system, and detection/diagnostic instruments. A schematic picture of IEPS is shown in Figure 2.2. The base pressure measured by an ion gauge (Granville-Phillips 370 Stabil), is $\lesssim 5 \times 10^{-10}$ mbar. Technical details are very similar to LIFE.

The vacuum is obtained with a turbo-molecular pump (Oerlikon Leybold vacuum 600C, 600 liters/s), backed up by a scroll pump (Edward nXDS15i). A closed-cycle helium cryostat (CTI M350), is mounted on a rotating platform (Thermionics RNN-400 equipped with stepper motor) at the center of the chamber (see Figure 2.2). At the end of the cold finger there is a sample holder (see the inset in Figure 2.2), where an infrared transparent window can be mounted as substrate for the ices. Two temperature sensors driven by a Lakeshore 335 temperature controller are mounted along the cold finger. The first one is close to the sample holder (Lakeshore DT-670-OB), while the other is located on tip of the second stage of the cryostat (Lakeshore DT-470-SD). The cold finger and copper radiation shield are placed on the second and first stages of the cryostat, respectively. A heater is hooped on the cold finger and operated through the temperature controller. In order to improve thermal conductivity, all junctions are made with indium (99.99% purity). The infrared transparent window is housed in the sample holder of the cryostat. The window is held by a circular copper ring tightened by screws with spring washers to avoid damaging the window at low temperatures. In this configuration, the substrate can be maintained at temperatures in the range of $11 - 340$ K with an uncertainty of ± 0.3 K.

2.1.3 Pre-mixing chamber and gas line system

The gas-line systems of the LIFE and IEPS facilities represent two high-precision approaches to gas mixture preparation, both anchored by stainless steel architectures and advanced vacuum

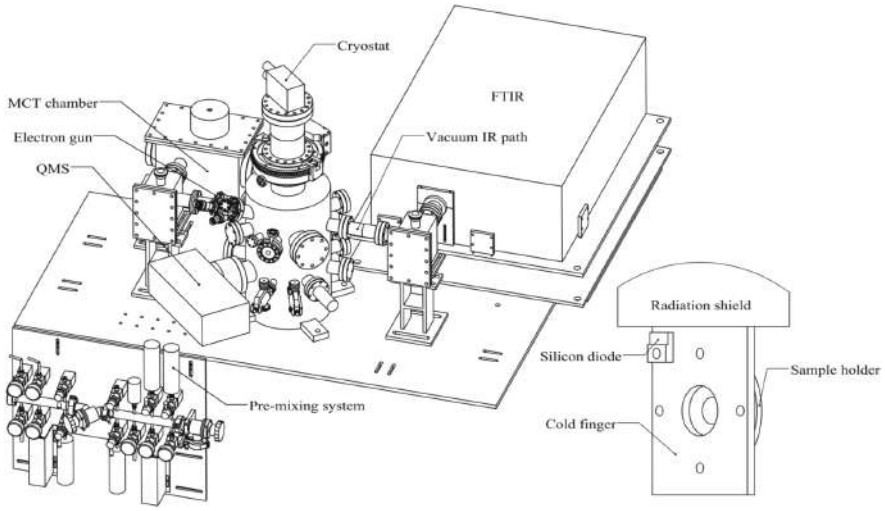

Figure 2.2: A sketch of the IEPS UHV experimental setup, in which the energetic electrons source, and the diagnostic systems are indicated. In the right inset some details of the cold finger assembly are reported.

technology, yet they differ subtly in their configuration and output delivery. The LIFE facility is designed around a central stainless steel cylinder connected to six empty bottles and six inlet ports, utilizing a Pfeiffer-HiCube 80 ECO turbomolecular pump to achieve base pressures of approximately 10^{-8} mbar after baking at 120 °C. In contrast, the IEPS facility employs a dual-line pre-mixing system featuring four bottles of equal volume, achieving a comparable base pressure of $\approx 10^{-7}$ mbar through an Oerlikon Leybold 361 turbomolecular pump backed by an oil-sealed mechanical pump with a molecular sieve trap. While both systems rely on capacitance-based manometry for pressure measurement, using an MKS 626B Baratron for LIFE and a BROOKS CMC series for IEPS, their analytical and delivery mechanisms diverge. The LIFE system integrates an ESS Vision 200D QMS directly to its mixing chamber via a leak valve for real-time analysis and features a specialized leak valve dedicated to corrosive gases like NH_3. For gas introduction, LIFE directs flow through a capillary toward the sample holder, whereas IEPS utilizes a VG ZLVM 940R leak valve connected to a 1/16 inch stainless steel tube pointed specifically toward a cold substrate. Ultimately, while LIFE offers higher baking temperatures and more inlet flexibility, IEPS provides a more robust backing pump stages and a dual-line setup tailored for precise deposition onto cold surfaces.

2.2 Detection system

The diagnostic suites of the IEPS and LIFE facilities are centered on the real-time observation of ice-phase transformations and gas-phase desorption, employing Fourier Transform (mid-)InfraRed (FTIR) and Quadrupole Mass spectrometers in very similar instrumental configurations.

The FTIR spectrometer (Bruker VERTEX 70), is equipped with a mercury–cadmium–telluride (MCT) detector for recording transmission spectra of the ice samples. The infrared beam is introduced into the chamber via external mirrors and guided along a vacuum optical path to minimize absorption from atmospheric CO_2 and H_2O. This path is separated from the UHV chamber by two wedged ZnSe window flanges positioned at the entrance and exit ports. After transversing the sample, the beam is reflected toward the detector by a mirror located on the opposite side of the chamber. To prevent contamination and moisture accumulation, the optical components and detector are enclosed in protective housings, while the MCT detector is maintained within a dedicated vacuum chamber. Additionally, the spectrometer and associated optical assemblies are continuously purged with dry air to ensure stable operating conditions. Gas-phase products are monitored by a Hiden Hal/3F PIC QMS, covering a mass range of $1 - 300$ amu with a 0.5 amu resolution. This allows for precise Temperature Programmed Desorption (TPD) studies, identifying volatile species as they sublimate from the ice matrix. The QMS is mounted with its central axis pointed along the normal direction of the substrate. The emission current of the QMS filament and integrated scanning time can be manually regulated.

The exploited emission current is 100 μA, and the scanning time 100 ms for each mass. The electron-impact ionization energy has been chosen to be 70 eV. The minimal partial pressure detectable by the QMS is 3.5×10^{-15} torr.

The infrared spectrum is collected during the whole experiment to monitor the column density (thickness) of the sample as well as the products. Resolution may be tuned from 0.5 to 4 cm^{-1} according to different experiments. The column density N of a given species can be calculated as

$$N = \frac{\cos\theta}{A} \int_{\Delta\nu} \tau_\nu d\nu \tag{2.1}$$

where ν the wavenumber in cm^{-1}, θ the angle between the infrared beam and the ice surface, A the absorption line strength in cm/molecule, τ_ν the optical depth, and the integration is done over the spectral band $\Delta\nu$. The column density is frequently translated in ML through the conversion factor 1×10^{15} molecules cm^{-2}.

Complementing the infrared data in the LIFE facility is a Resonance Ltd. VS7550 vacuum ultraviolet spectrometer. Purged with N_2, this instrument monitors plasma emission and potential fluorescence/X-ray reflections in the $100 - 400$ nm range.

2.3 Energetic sources

In this work, ice samples are processed using three distinct types of energetic sources across the LIFE and IEPS laboratory astrochemistry facilities. Both setups share a common approach to vacuum ultraviolet irradiation, employing similar Microwave-Discharge Hydrogen-flow Lamps (MDHL). Beyond ultraviolet irradiation, the two laboratories offer complementary processing capabilities: the LIFE setup is equipped with a multi-anode electron-impact X-ray source emitting in the range $0.3 - 10$ keV, while the IEPS facility features an electron gun, tunable in energy between 100 and 5000 eV. These three types of energetic sources, vacuum ultraviolet photons, X-rays, and electrons, are described in detail in the following subsections.

2.3.1 Vacuum-ultraviolet lamp

The ultraviolet irradiation is provided by a MDHL coupled to the experimental chamber through a magnesium fluoride (MgF_2) window. This window acts as an optical filter with a specific transmittance consistent with established literature, effectively cutting off radiation below approximately 114 nm. Sometimes, a calcium fluoride (CaF_2) window is employed to specifically isolate the molecular components of the spectrum, because it possesses a higher cut-off at approximately 123 nm, which effectively blocks the 121.6 nm Lyman$-\alpha$ emission. The lamp operates using a continuous flow of pure molecular hydrogen at a pressure of 0.4 mbar (Figure 2.3, left panel), with a microwave generator maintained at a power of 80 W.

The flux of the ultraviolet lamp is estimated by measuring the conversion rate of CO_2 to CO during the ultraviolet irradiation of pure CO_2 ice at 10 K, a method previously used by Cottin et al. (2000) and Muñoz Caro et al. (2010). The ultraviolet flux results

$$I_{\mathrm{UV}} = \frac{N_t - N_0}{Q_e t} \tag{2.2}$$

where $Q_e = 1$ (molecule $photon^{-1}$) is the quantum efficiency for the formation of CO, and N_0 and N_t the initial and final column densities of CO, respectively. The resulting ultraviolet flux is estimated to be $I_{\mathrm{UV}} = 3 \times 10^{14}$ photons cm^{-2} s^{-1}. During irradiation, the photon flux is continuously monitored using a nickel mesh positioned at the end of the quartz tube. The current measured by this device indicates a decrease in flux of approximately 20% during the first 30 minutes of operation, followed by an additional reduction of about 5% over the subsequent 70 minutes (Ciaravella et al., 2018; Huang et al., 2020).

A critical aspect of the lamp's performance is its geometric configuration, which dictates the spectral distribution of the emitted light. Chen et al. (2014) identify different geometric configurations, specifically T-type and F-type (see Figure 2.3, right panel). In the T-type configuration, the hydrogen gas is evacuated perpendicularly to the discharge tube, creating a higher pumping efficiency that favors intense atomic Lyman$-\alpha$ emission, whereas the F-type configuration utilizes a standard axial flow that results in a spectrum dominated by molecular hydrogen Lyman and Werner bands. This results in a spectrum where the atomic Lyman$-\alpha$ line at 121.6 nm is highly prominent, accounting for roughly 19.1% of the total emission. In

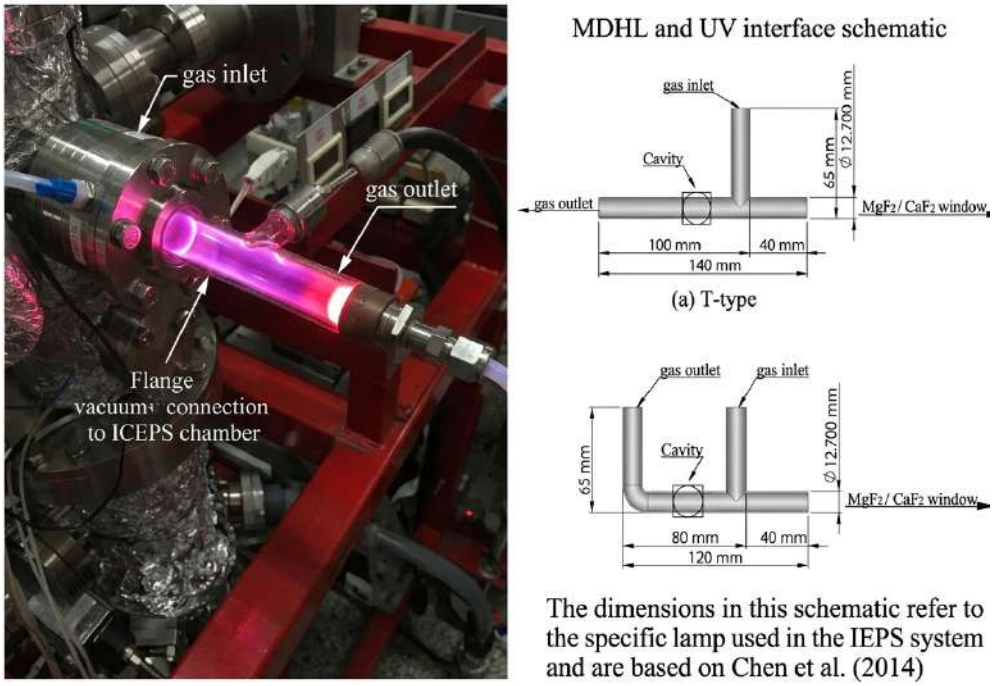

Figure 2.3: Experimental setup and geometric configurations of the MDHL integrated into the IEPS system. Left: the lamp in operation at a hydrogen pressure of 0.4 mbar; the intense purple glow illustrates the plasma discharge within the quartz tube coupled to the main chamber. Right: schematic representation of the T-type (upper panel) and F-type (lower panel) geometries. The technical dimensions provided correspond to the specific lamp assembly mounted on the IEPS setup.

contrast, the standard F-type configuration used in many commercial lamps results in a lower Lyman$-\alpha$ proportion of about 8.4%, leaving the spectrum dominated by molecular hydrogen Lyman and Werner bands. In YSOs, Lyman$-\alpha$ is often the single most significant component of the vacuum ultraviolet spectrum. It is produced intensely by the star's chromosphere and the accretion shocks where material from the disc falls onto the stellar surface. Studies have shown that Lyman$-\alpha$ can account for 70% to 90% of the total vacuum ultraviolet flux reaching the surface of the disc. The ultraviolet field found in the cold, dense interiors of molecular clouds is generated internally by cosmic-ray excitation of H_2 (Prasad and Tarafdar, 1983; Cecchi-Pestellini and Aiello, 1992). This field is primarily composed of the Lyman and Werner molecular bands ($140 - 1700$ nm) and lacks the intense Lyman$-\alpha$ dominance seen in stellar spectra. Thus, in principle we might use different configurations to describe more accurately different astronomical environments. The integrated MDHLs are configured in a T-type arrangement in both facilities.

In practice, the reliability of these simulations lies on matching the lamp's spectral output with the wavelength-dependent absorption cross-sections of the ice analogs. Since absorption efficiency varies significantly with wavelength, aligning the lamp's emission peaks with the absorption response of a specific species is crucial (see e.g. Cruz-Diaz et al. 2014a). Figure 2.4 illustrates the MDHL emission spectrum as measured by the Resonance Ltd. VS7550 vacuum ultraviolet spectrometer integrated into the LIFE system.

2.3.2 X-ray source

The X-ray source integrated into the experimental setup is the XR 50 NAP model by SPECS, a versatile system designed to operate across a broad pressure range from ultra-high vacuum to

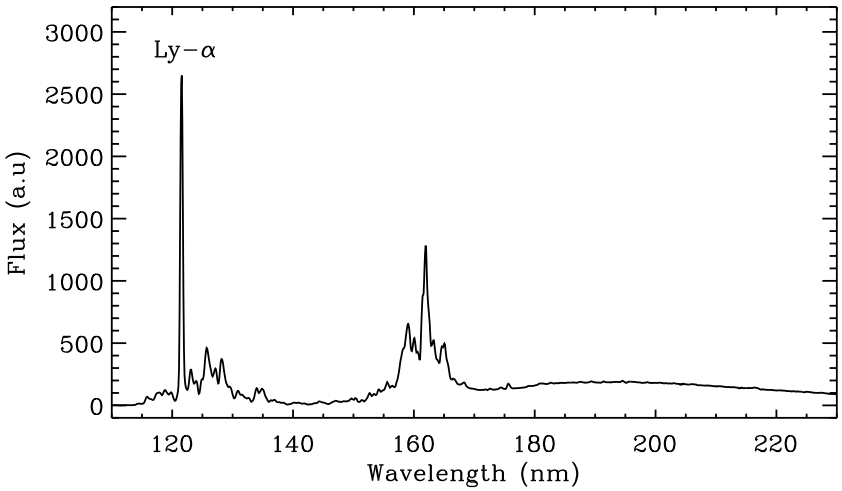

Figure 2.4: Emission spectrum of the MDHL installed in the LIFE facility. The dominant peak at 121.6 nm represents the atomic hydrogen Lyman$-\alpha$ line. The structured emission features immediately adjacent to this peak and extending to roughly 165 nm are the Lyman band ($B^1\Sigma_u^+ \rightarrow X^1\Sigma_g^+$) of molecular hydrogen. The secondary cluster of peaks centered near 160 nm represents the Werner band ($C^1\Pi_u \rightarrow X^1\Sigma_g^+$).

near-ambient conditions. This operational flexibility is achieved through a differential pumping system and a specialized membrane window that acts as a robust gas barrier. The source is mounted on the chamber flange and aligned toward the sample holder to ensure uniform irradiation of the ice film. The source utilizes a dual-anode system, with faces coated in aluminum and copper, capable of accelerating electrons through an electric field of up to 15 kV to generate specific X-ray emission lines. The X-rays are generated by electron-impact excitation, where electrons emitted from a heated filament are accelerated toward a metallic anode under a high voltage V. Upon impact, X-rays are produced through bremsstrahlung and characteristic emission processes. The output intensity is determined by the anode power, $P = V \times I_e$ where I_e is the emission current. Specifically, the source produces photons at 1486.6 eV for the Al Kα line, while the copper anode provides lines at 931.6 eV (Lα line) and 8055 eV (Kα line), with maximum power outputs of 400 W and 300 W, respectively. At a nominal working distance of 20 mm, the source delivers a photon flux of $I_X = 4.1 \times 10^{10}$ photons s^{-1} for the Al Kα line with a spot size $s_X \approx 80$ mm^2, at a working distance of 20 mm. This cross-section is larger than the FTIR spectrometer's infrared beam, $s_{IR} = 50$ mm^2, providing that the we are correctly sampling the ice.

The interface between the source and the target environment is maintained by an Al-coated silicon nitride (Si_3N_4) membrane window with a thickness of 200 nm. As shown in the transmission curve, Figure 2.5, this window is highly efficient, providing a transmissivity greater than 80% for the Al line and exceeding 99% for the Cu lines within the relevant photon energy ranges. Beyond its optical transparency, the currently mounted membrane offers the necessary mechanical integrity to withstand a pressure differential of up to 20 mbar, facilitating experiments in near-ambient conditions. To ensure stable operation and component longevity, the source is supported by a dedicated water-cooling system equipped with precise sensors to monitor temperature, flow rate, and water pressure.

2.3.3 Electron gun

The Kimball Physics EFG-7 electron gun, integrated with the EGPS-2017 power supply, serves as a critical energetic source within the IEPS facility for the simulation of interstellar radiation environments. This system is primarily utilized to mimic the processing of ice mantles by secondary electrons, generated when primary cosmic rays penetrate solid matter, or the electron bombardment of icy moons (such as Europa or Enceladus) within the magnetospheres of giant planets. By delivering a controlled electron beam with an energy range typically spanning from 100 eV to 5 keV, the EFG-7 facilitates the investigation of radiolysis, the synthesis of

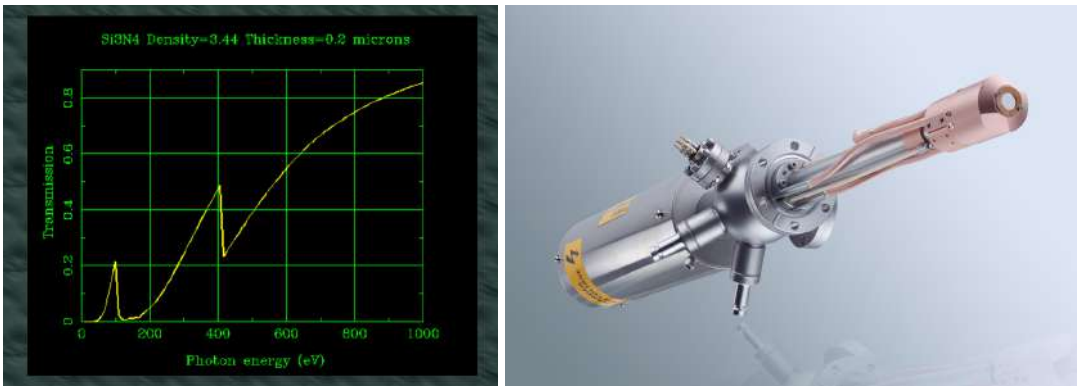

Figure 2.5: Theoretical transmission curve of the 200 nm thick silicon nitride (Si_3N_4) membrane window (density = 3.44 g cm^{-3}) as a function of photon energy (left panel). The sharp features in the curve correspond to the characteristic absorption edges of the membrane's constituent elements, while the overall profile confirms a transmissivity exceeding 80% for the primary energy ranges utilized in the XR 50 NAP source shown in the right panel.

complex organic molecules, and electron-stimulated desorption processes. The accompanying EGPS-2017 power supply provides the high-precision digital control necessary to maintain stable beam energy, focus, and filament current over the long durations required for astrochemistry experiments. Furthermore, the gun's ultra-high vacuum compatibility ensures that the pristine nature of the ice analogues is preserved, while the ability to accurately measure beam flux allows researchers to quantify energy deposition in terms of eV per molecule. The electron gun has a flux of $I_{\rm el} = 3.2 \times 10^{11}$ electron cm^{-2} s^{-1}, and a spot size $s_{\rm el} = 2$ cm^2. This number refers to the electron source integrated in IEPS. The IEPS is designed so that the infrared beam size is smaller than the electron spot size. This ensures that the portion of the ice being read by the spectrometer has been uniformly irradiated by a consistent electron flux across its entire integrated area. Figure 2.6 illustrates the electron gun alongside the experimental characterization of its output, specifically the spatial distribution of the electron beam intensity as captured by a fluorescent plate. In normal operating modes—characterized by low emission current and minimal deflection voltages—the beam maintains a nearly homogeneous circular profile. To quantify this distribution, the fluorescence intensity was captured via a CCD detector and converted into a normalized 8-bit image (Huang, 2019). To prevent detector saturation, the camera was positioned at an angle relative to the plate's normal. This spatial profile confirms that the electron flux delivered to the ice samples is uniform, ensuring consistent energy deposition across the target surface.

2.4 Experimental protocols

To simulate the diverse structural and chemical conditions of interstellar ices, four experimental protocols were defined. The primary distinction between these sequences lies in the thermal history of the ice growth, which determines whether the resulting mantle is a homogeneous mixture or a stratified (layered) structure. We consider the following processes: cryogenic cooling, ice deposition, energetic irradiation, and TPD, and 4 protocols (hereafter called *modes*)

mode 1 — sequential processing (mixed ices):

1. pre-cooling: prior to cooling, a baseline infrared spectrum is acquired at 300 K to provide system vacuum integrity and instrument calibration;

2. cooling: the substrate is cooled from room temperature (300 K) to a base temperature of approximately 10 K;

3. deposition: the gas mixture is introduced only after the target temperature is reached; because all species condense simultaneously at 10 K, this results in a homogeneously mixed ice;

4. irradiation (optional): the stable ice is subjected to vacuum ultraviolet, X-ray, or electron irradiation to induce photochemical transitions;

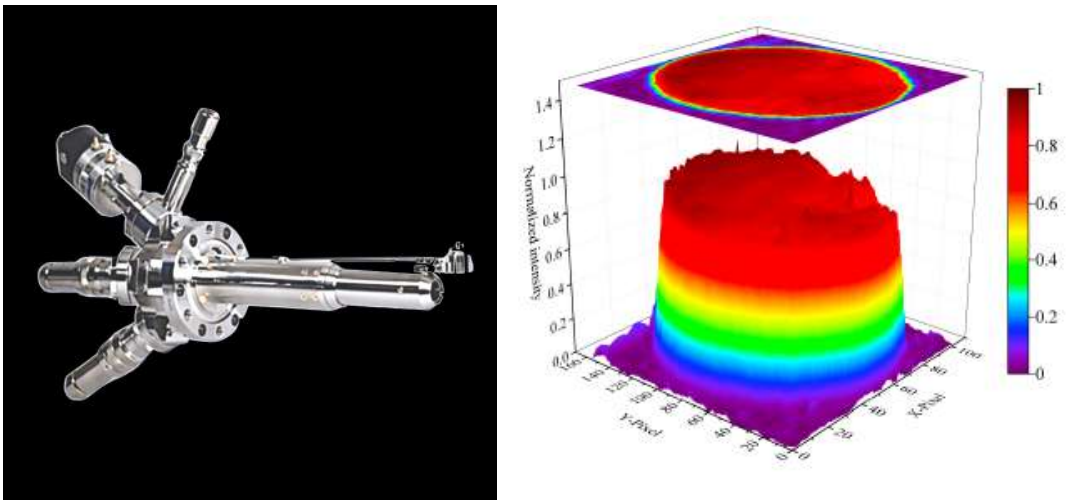

Figure 2.6: Left panel: photographic layout of the Kimball Physics EFG-7 electron gun. Right: panel normalized spatial intensity distribution of the electron beam; the beam profile was imaged using a fluorescent plate and a CCD camera, demonstrating the homogeneous circular morphology achieved under standard operating conditions (Huang, 2019).

5. warm-up (optional): the procedure concludes with TPD at a constant ramping rate without further irradiation.

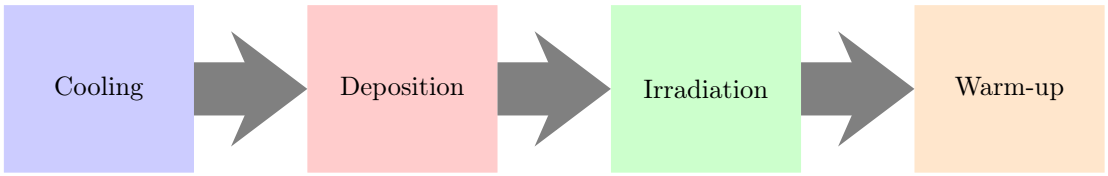

Figure 2.7: Flow chart diagrams for mode 1.

mode 2 — concurrent growth (layered ices):

1. pre-cooling: a baseline infrared spectrum is acquired at 300 K for calibration;
2. simultaneous cooling and deposition: gas introduction begins at 200 K and continues throughout the cooling ramp to the base temperature; this results in a layered structure, as less volatile species deposit first;
3. irradiation (optional): the layered ice is irradiated only after reaching the base temperature;
4. warm-up: the ice is analyzed via TPD without irradiation.

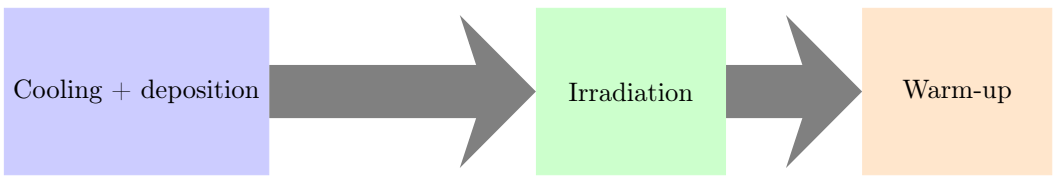

Figure 2.8: Flow chart diagrams for mode 2.

mode 3 — fully simultaneous processing:

1. pre-cooling: a baseline infrared spectrum is acquired at 300 K for calibration;

2. simultaneous cooling, deposition, and irradiation: gas introduction and irradiation are initiated at 200 K and maintained until the substrate reaches the lowest temperature; this ensures each molecular species is processed at its specific condensation temperature during the formation of the stratification;

3. warm-up (optional): the ice is analyzed via TPD without irradiation.

Figure 2.9: Flow chart diagrams for mode 3.

mode 4 — processing during thermal evolution:

1. sequential start: follows the pre-cooling, cooling, and deposition steps of mode 1 to create a mixed ice;

2. warm-up + irradiation: unlike the other modes, irradiation is maintained during the TPD phase as the substrate is warmed; this allows for the study of chemistry as the ice matrix softens and sublimates.

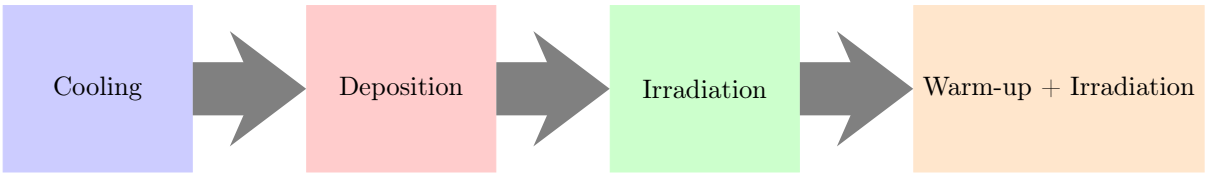

Figure 2.10: Flow chart diagrams for mode 4.

2.4.1 Processes involved in the experiments

The experimental sequence begins with the thermal preparation of the system. The substrate is cooled from room temperature (300 K) to a base temperature of approximately 10 K using a closed-cycle helium cryostat. Prior starting the cooling ramp, a baseline infrared spectrum is acquired. This step is essential to provide the integrity of the system's vacuum, verify the absence of contaminants, and provide a reference point for instrument calibration. Once the baseline is established, the cooling process proceeds, providing the thermal foundation for subsequent ice growth.

Ice formation is achieved by introducing a gas mixture, prepared in the stainless-steel premixing system, into the UHV chamber through a high-precision leak valve. The method of deposition determines the physical architecture of the ice: in isothermal deposition (modes 1 and 4), the gas is introduced only after the substrate reaches the base temperature, resulting in a homogeneously mixed ice mantle. Conversely, in concurrent deposition (modes 2 and 3), gas introduction begins at 200 K, allowing species to condense according to their specific sublimation temperatures. This creates a layered structure that more accurately simulates the complex freeze-out history observed in molecular cloud environments.

Energetic processing is then (optionally) applied to the ice analogs to simulate interstellar radiation fields. Depending on the experimental requirements, the ice is subjected to vacuum ultraviolet photons from the MDHL, X-rays from a SPECS XR 50 source, or electron bombardment from a Kimball Physics EFG-7 gun. These irradiation sources induce photochemical and photophysical transitions, triggering the synthesis of new, more complex species from the original reactants. The timing of this irradiation, whether performed on a stable ice at 10 K or during the growth and warming phases, allows for the investigation of different chemical kinetic regimes.

The final diagnostic phase consists of TPD. The substrate is warmed at a precisely controlled constant ramping rate until it returns to room temperature. As the ice temperature increases, the various molecular species sequentially sublimate into the gas phase, where they are monitored by the QMS. This process generates desorption profiles that are necessary for identifying the synthesized photo-products and determining their respective binding energies. By correlating the TPD data with the initial layered or mixed layout of the ice, the efficiency of chemical pathways under specific astrophysical conditions can be quantified.

3. CO line profiles in accreting ices

In this chapter, we present a series of experiments investigating the line profiles of the carbon monoxide C≡O stretching mode in ice mixtures containing species relevant to interstellar ices. We introduce a method for the deconvolution of the profile into contributions associated with distinct chemical microenvironments, and we apply this methodology to astronomical observations. In addition, we include a (still preliminary) appendix in which we examine how these profiles are affected when the substrate is not inert but mineral in nature; at this stage, a meteorite is employed as a representative substrate.

3.1 Introduction

Interstellar ices play a crucial role in the chemical evolution of interstellar and circumstellar regions. These ices, which mainly form in the coldest parts of molecular clouds and protoplanetary discs, provide a dynamic medium for chemical reactions that can lead to the formation of prebiotic compounds (Herbst et al. 2020 and references therein). Their molecular properties and spectroscopic signatures are strongly influenced by the local environment: temperature, density, and radiation fields affect both the formation and composition of ice mantles (Tielens et al., 1991), while polar and non-polar ices produce distinct line profiles due to their molecular architectures and intermolecular interactions (Gorai et al., 2020). The physical phase of the ice, amorphous, crystalline, or mixed, also leaves a recognizable imprint on the spectra, with the crystalline phases typically producing sharper, more structured bands compared to the broader features of the amorphous ices (Cuppen et al., 2024). The properties of dust also modulate the profiles, as grain size and morphology introduce scattering effects that broaden or distort absorption characteristics (Dartois et al., 2022). Energetic processing by ultraviolet photons, cosmic rays or X-rays further modifies ices by producing radicals, ions, and new species, which results in spectral changes like band shifts or new features (Muñoz Caro et al., 2025).

In molecular clouds, ices condense sequentially onto dust grains, with their composition reflecting both the local physical conditions and the condensation temperatures of different species (Öberg et al., 2011). Although only weakly bound, hydrogen atoms have residence times at temperatures of $10-20$ K sufficient to hydrogenate O, C, and N atoms, producing efficiently water (e.g., Ioppolo et al. 2008), methane (Qasim et al., 2020), and ammonia (e.g., Jonusas et al. 2020). Thus, it is clear that although there are certainly pure materials in the ices, there is also considerable mixing, and, typically, the water ice formed is not pure but incorporates other less abundant species (e.g., methanol formed through OH-mediated reactions of methane, Qasim et al. 2018). Several of these species, including CH_4 and NH_3, are observed to correlate with H_2O, consistently with their formation through hydrogenation reactions taking place during the buildup of water ice. The mixture CO_2 + H_2O is also in this category, suggesting that CO is being oxygenated while C and N are hydrogenated. The resulting CO_2 can thus interact with H_2O if located properly (Boogert et al., 2015). This initial layer, dominated by water ice, serves as a matrix and stable substrate for subsequent layers of molecules. More volatile species, such as the abundant CO, form an outermost layer as temperatures drop below the corresponding sublimation points. Residual nitrogen-bearing species such as N_2H^+, which are otherwise destroyed in reactions with CO molecules, can accumulate in the gas phase and serve as tracers of the densest cloud regions (Lippok et al., 2013). Eventually, they may also condense onto the outer CO-rich ice layer. The hydrogenation of carbon monoxide results in the formation of various products, mainly methanol CH_3OH and other hydrocarbons. Once formed, methanol serves as a fundamental building block in the synthesis of more complex organic molecules (Chuang et al., 2016).

While molecular clouds offer relatively stable environments for the buildup of layered ices, conditions in protoplanetary discs are more dynamic. Grains undergo radial and vertical transport, and they may cross snow lines where sublimation and recondensation events blur compositional stratification (e.g., Bergner and Ciesla 2021). Although layering may still occur in cold midplanes, turbulence and grain aggregation likely produce ices that are less neatly stratified than in the cold, low-velocity core regions of molecular clouds. The resulting ice structures are therefore expected to be more heterogeneous and compositionally differentiated.

Because intermolecular interactions shape the profile of infrared absorption bands, the structural configuration of an ice, whether well mixed or chemically segregated into distinct layers, should be imprinted in its infrared spectrum. Numerous spectroscopic studies have demonstrated this effect (see Müller et al. 2021 and references therein). CO is particularly diagnostic

in this regard, as its narrow band profiles are highly sensitive to the chemical environment, as demonstrated by many laboratory experiments (Fraser et al., 2004; Palumbo et al., 2006; Bouwman et al., 2007; Dawes et al., 2016; Ciaravella et al., 2020) and numerical simulations (Collings et al., 2014; Zamirri et al., 2018; Escribano et al., 2025). However, the majority of these experiments were performed under static conditions, depositing ices at fixed cryogenic temperatures (around typically 10 K). For instance, Müller et al. (2021) investigated layered versus mixed ices of four major constituents, H_2O, CO, CO_2, and CH_3OH, and concluded that a layered ice structure best reproduces observed methanol bands in prestellar cores and star-forming regions. Their work demonstrated how JWST sensitivity can constrain the structural nature of interstellar ices. However, in space, layered structures often arise not from deposition onto substrates already at 10 K, but during cooling of grains that experience temperature gradients. Using this structural proxy, Jiménez-Escobar et al. (2024) deposited a ternary gas mixture composed of H_2O, NH_3, and CO while the substrate cooled from 200 K to 10 K, producing layered structures more representative of actual grain histories. Direct deposition effectively simulates the hydrogenation process, as the high mobility of H atoms (even at 10 K) leads to the near-instantaneous molecular transformation of precursors upon grain accretion. However, while this effectively mimics H_2O formation, it should be noted that the yields of species like NH_3 may be lower in space due to competition between atomic sticking and gas-phase reactivity (Daranlot et al., 2012).

Following this methodology, we extend our investigation of temperature-dependent deposition to CO-bearing ices. To simulate the thermal evolution of grains in space, we perform experiments where these ices are deposited both at constant cryogenic temperatures and during controlled cooling. The experimental setup and the resulting data are detailed in Sections 3.2 and 3.3. In Section 3.4, we interpret these findings from both laboratory and astronomical perspectives, specifically examining their implications for recent JWST observations. Finally, Section 3.5 summarizes our conclusions.

3.2 Experiments

Experiments were carried out with *Interstellar Energetic-Process System* (IEPS), an ultra-high vacuum chamber with a base pressure of 5×10^{-10} Torr, achieved after baking the chamber at 100° C for 48 h to minimize contamination. The system is equipped with a closed-cycle CTI M350 helium cryostat installed on a rotating platform. An infrared transparent CaF_2 window, used as the substrate, was mounted on the cryostat, which allows temperature control in the $11 - 340$ K range. The evolution of the condensed phase was monitored with a Bruker Vertex 70 mid-FTIR spectrometer ($8000 - 400$ cm^{-1}) equipped with a vacuum-kept Mercury–Cadmium–Telluride (MCT) detector. The instrument provides selectable spectral resolutions of 0.5, 1, 2, and 4 cm^{-1}. Complementary gas-phase diagnostics were obtained with a quadrupole mass spectrometer (QMS; Hiden Analysis/3F RC PIC), scanning masses from 1 to 200 amu. A detailed description of the facility can be found in Huang et al. (2020). Ice thickness was monitored in situ via FTIR spectroscopy. The CO column density was determined by integrating the CO fundamental stretching band and subsequently converted to monolayers (ML) using a standard surface density of 1×10^{15} molecules cm^{-2} per ML.

Using a deposition pressure of 5×10^{-9} Torr, two deposition protocols were adopted:

1. isothermal co-deposition at 12 K carried out with species in predefined ratios; the total thickness of the ice samples was kept below 300 ML;

2. simultaneous cooling and deposition. Before each experiment, the system was stabilized for 1 h at 200 K under ultrahigh vacuum conditions. Gas mixtures condensed on the substrate during its cooling from 200 K down to 12 K at a rate of 2 K min^{-1}; deposition was interrupted when the final temperature of 12 K was reached; the injection flux into the chamber was regulated as to obtain a deposition pressure of 5×10^{-9} Torr at 200 K, and was then maintained constant throughout the cooling process.

The complete set of experiments is summarized in Table 3.1. The choice of deposition protocol dictates the resulting ice morphology, which is summarized in the sixth column of the Table. Although, experiments $15 - 18$ are performed in mode 1, we classify them as "top layer" because, in the ice stratified description, CH_3OH (hydrogenation) and CO_2 (via energy deposition by cosmic-rays or X-rays, e.g., Ivlev et al. 2023; Ciaravella et al. 2016, mixed phase

Table 3.1: List of experiments and ice description.

exp.	composition	pre-mixing ratio	final ratio	deposition mode	ice type	CO column density (ML$^{(a)}$)
1	CO			1	pure	80
2	CO, H_2O		1 : 2.3	1	mixed	79
3	CO, H_2O, NH_3		1 : 2.5 : 1.4	1	mixed	58.5
4	CO, H_2O, CH_4		1 : 2.1 : 1.6	1	mixed	56.4
5	CO, H_2O, NH_3, CH_4		1 : 2.7 : 1.5 : 1.4	1	mixed	56.5
6	CO, CH_4		1 : 1.4	1	mixed	52.3
7	CO			2	pure	8.0
8	CO, H_2O	3 : 1	1 : 3	2	layered	6.7
9	CO, H_2O, NH_3 (5×10^{-9} Torr)$^{(b)}$	6 : 2 : 1	1.2 : 1.9 : 1.3	2	layered	7
10	CO, H_2O, NH_3 (1×10^{-8} Torr)	6 : 2 : 1	1.2 : 2.3 : 1	2	layered	14
11	CO, H_2O, NH_3 (1×10^{-7} Torr)	6 : 2 : 1	1.2 : 1.8 : 1	2	layered	132
12	CO, H_2O, NH_3 (6×10^{-7} Torr)	6 : 2 : 1	1.2 : 2.1 : 1	2	layered	416
13	CO, H_2O, CH_4	6 : 2 : 1	1 : 2.3 : 1.2	2	layered	3.1
14	CO, H_2O, NH_3, CH_4	6 : 2 : 1 : 1	1 : 2 : 1.3 : 1	2	layered	5
15	CO, CO_2		2.1:1.2	1	top layer	54.3
16	CO, CH_3OH		1.7 : 1	1	top layer	54.3
17	CO, CH_3OH		1 : 2.1	1	top layer	58.5
18	CO, CH_3OH, CO_2		2.1:1.1:1	1	top layer	54.3

(a) 1 ML = 1×10^{15} cm^{-2}; (b) this experiment has been repeated three more times at different deposition pressures.

processes, Terwisscha van Scheltinga et al. 2022, OH-radical reactions with CO, Oba et al. 2010) may form directly from CO in the top layer. The pronounced difference in CO column densities between deposition mode 1 (isothermal at 12 K) and mode 2 (cooling from 200 K to 12 K) yielding much lower CO column densities $\sim 5-8$ ML, is primarily due to the low deposition pressure of 5×10^{-9} Torr. This is consistent with the results of Jiménez-Escobar et al. (2024), which found a sharp, direct dependence of CO column density on the deposition pressure. However, these authors also show that the underlying layered structure itself does not change with pressure, implying that the fundamental mechanism of sequential condensation is invariant, even if the absolute ML amount of the final CO layer is small. To assess the impact of this pressure dependence on the CO line profiles, we repeated experiment 9 three additional times, systematically increasing the deposition pressures to match those exploited by Jiménez-Escobar et al. (2024). CO column densities resulting from experiments 10 to 12 are 14, 132, and 416 ML, respectively.

For all experiments, we recorded infrared spectra with 0.5, 1, 2 and 4 cm^{-1}. The spectra were acquired at both normal (90°) and oblique (45°) incidence to probe the longitudinal optical (LO) mode, which becomes detectable via the Berreman effect in pure CO ices (and other pure substances such as CO_2; e.g., Escribano et al. 2013; Cooke et al. 2016). The LO mode directly reflects the dielectric function of the ice and is sensitive to dipole–dipole interactions, molecular orientation, and structural order, providing information complementary to the transverse optical (TO) mode observed at normal incidence. In mixed ices, interactions with other species often shift, broaden, or suppress the LO mode, so while 45° spectra were still collected, the LO contribution is extremely weak or entirely absent. The integrated absorbance ratio between the two measurements should be approximately the geometric factor of 1.4, reflecting the longer optical path at 45°, unless experimental artifacts or scattering effects become significant.

3.3 Results

The experimental set investigates the infrared response of CO embedded in progressively more complex icy environments, beginning with pure CO and extending to mixtures with H_2O, NH_3, CH_4, CO_2 and CH_3OH. All experiments target the CO stretching band near 2138 cm^{-1}, but differ in composition, stoichiometric ratios, deposition mode, and deposition pressure. When deposition is performed at a fixed temperature of 12 K (mode 1), all gas-phase species efficiently stick to the substrate from the start. This leads to the formation of homogeneous mixtures, as the low temperature prevents chemical stratification; even volatile components like CO and CH_4 condense together with H_2O and NH_3. Figure 3.1 presents the infrared spectra for these isothermal mixtures. Visual inspection reveals that the introduction of polar species (H_2O, NH_3) broadens the CO stretching band at 2138 cm^{-1} and produces clear asymmetries. While, mixtures with water (experiment 2) show a pronounced blue wing near 2148 cm^{-1}, the presence of NH_3 (experiments 3 and 5) tends to smear out this blue wing. As a strong hydrogen-bond acceptor (He et al., 2022), ammonia interacts with H_2O dangling bonds, effectively displacing CO from these sites. In contrast, the presence of CH_4 (experiment 4) results in a blue wing with an unexpectedly larger intensity ratio, despite methane being non-polar.

The simultaneous cooling and deposition protocol (mode 2) generates a layered structure due to sequential freeze-out (Figure 3.2). Following the thermal gradient, water condenses first ($\sim$ 140 K), followed by ammonia ($\sim$ 110 K), and finally CO and CH_4 below $\sim$ 40 K (e.g., Collings et al. 2004). In interstellar regions, CH_4 is believed to form during the early stages of mantle evolution via the surface hydrogenation of atomic carbon, co-existing with H_2O and NH_3. Thus, in mode 2 experiments, methane (when present) serves as a representative apolar, non-hydrogen-bonding species. This allows us to investigate how the presence of chemically inert neighbors affects ice structure and condensation dynamics. Unlike mixed ices, the peaks in layered experiments are generally more symmetric, suggesting that CO forms a distinct phase partially separated from the more polar components.

Finally, Figure 3.3 illustrates the impact of CH_3OH and CO_2 on the CO profile (experiments $15-18$). Mixtures containing CH_3OH reveal a strong dependence on the stoichiometry of the ice. The CO-rich binary mixture displays an intense peak that, while relatively narrower than those in the other two experiments, still exhibits appreciable broadening. This indicates that even when CO is the major component, its vibrational environment is sufficiently heterogeneous due to interactions with the polar methanol molecules. As the ice becomes richer in methanol, the profile broadens further and develops a distinct red-shifted asymmetry. This confirms that

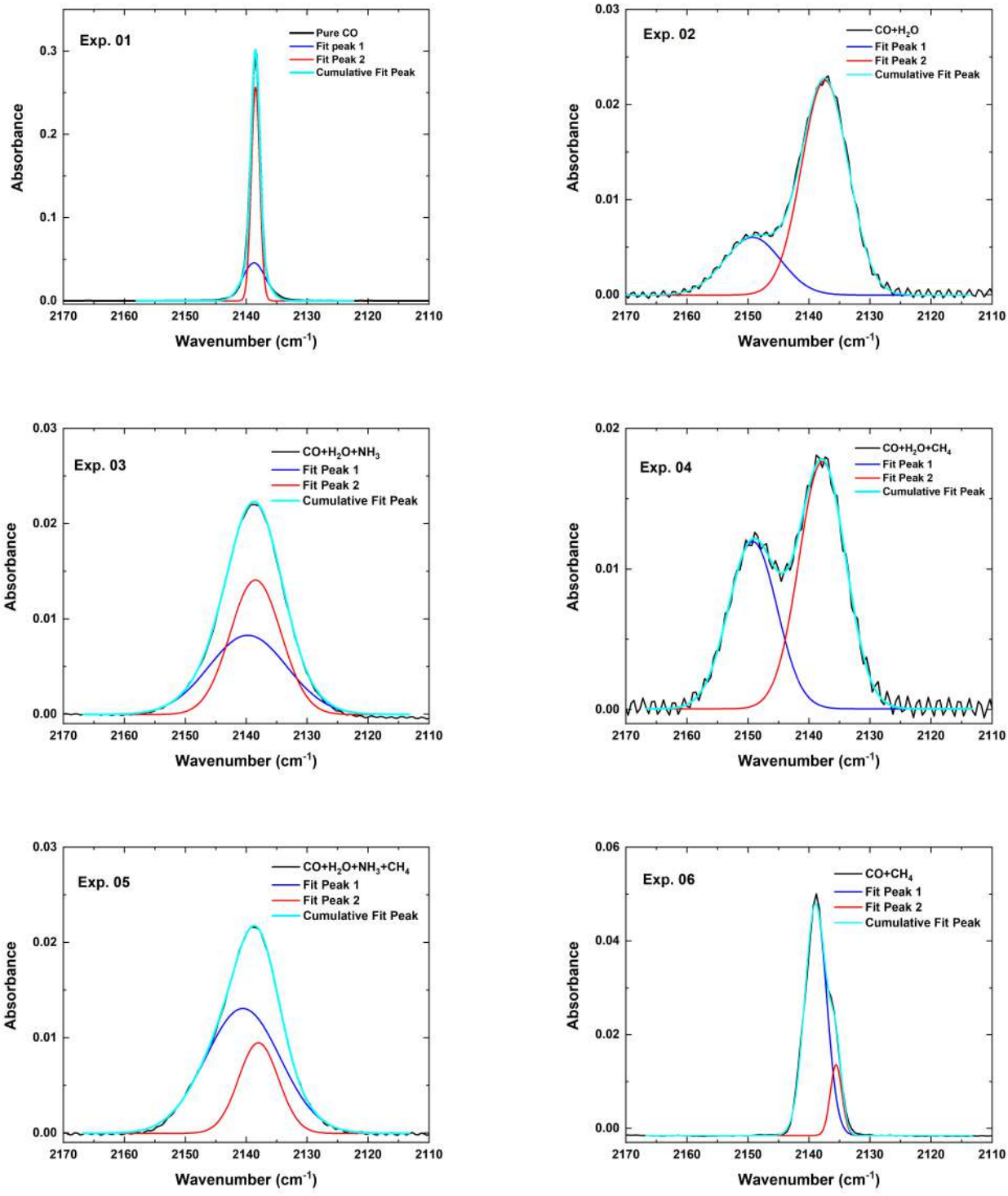

Figure 3.1: Normal incidence infrared spectra (black lines) of the CO stretching band at 2138 cm^{-1} for the first 6 experiments listed in Table 3.1, representing mixed ices produced by isothermal co-deposition at 12 K. Blue, red and green curves correspond to the Gaussian components centered to high, intermediate, and low wavenumbers, respectively (see Table 3.2). The spectral resolution is 1 cm^{-1}.

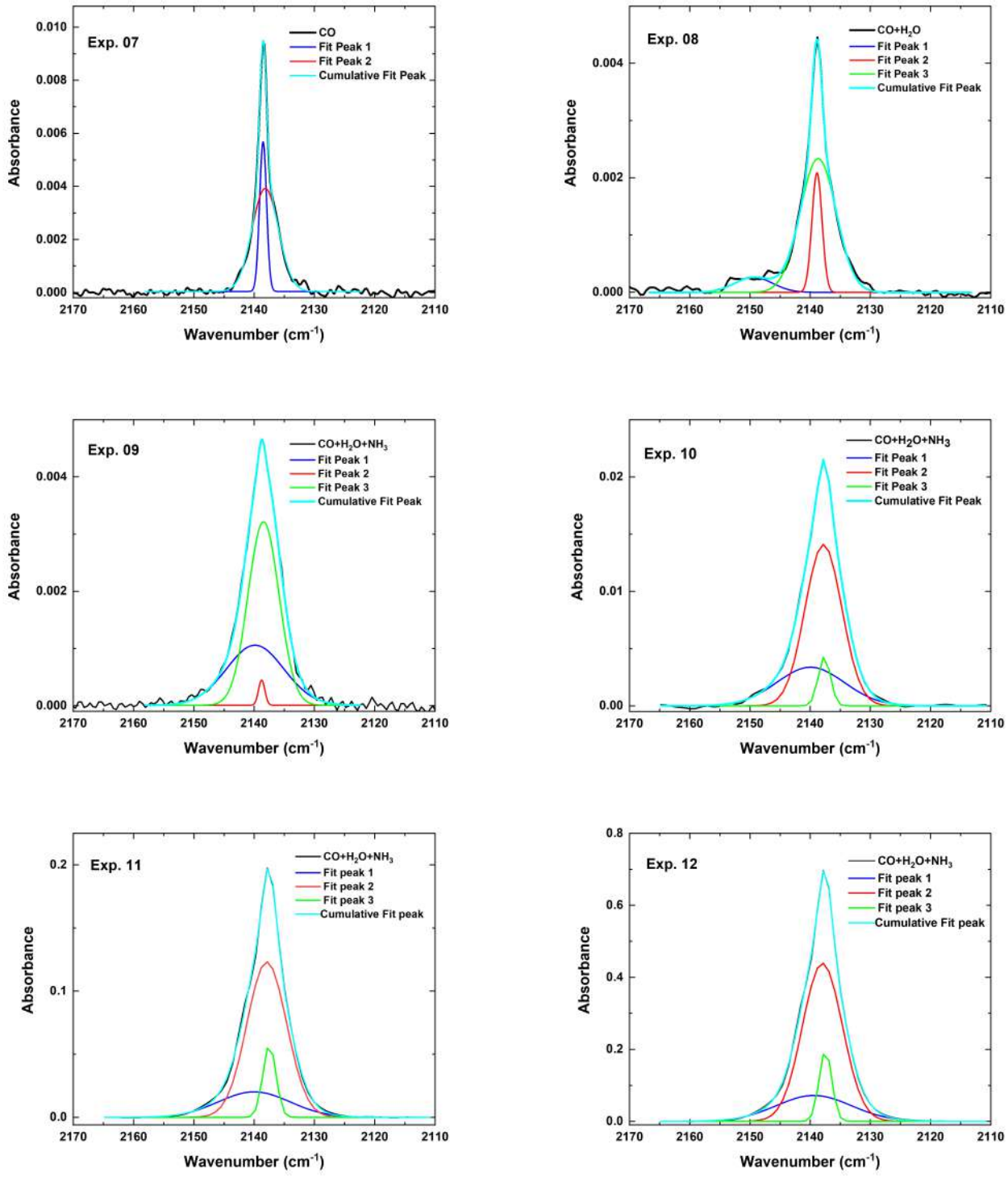

Figure 3.2: Normal incidence infrared spectra (black lines) of the CO stretching band at 2138 cm^{-1} for experiments $7 - 12$ listed in Table 3.1. The panels are arranged sequentially and correspond to layered ices produced by simultaneous deposition during cooling from 200 K to 12 K. Blue, red, and green curves indicate Gaussian components centered at high, intermediate, and low wavenumbers, respectively (see Table 3.2). Spectral resolution is 1 cm^{-1}.

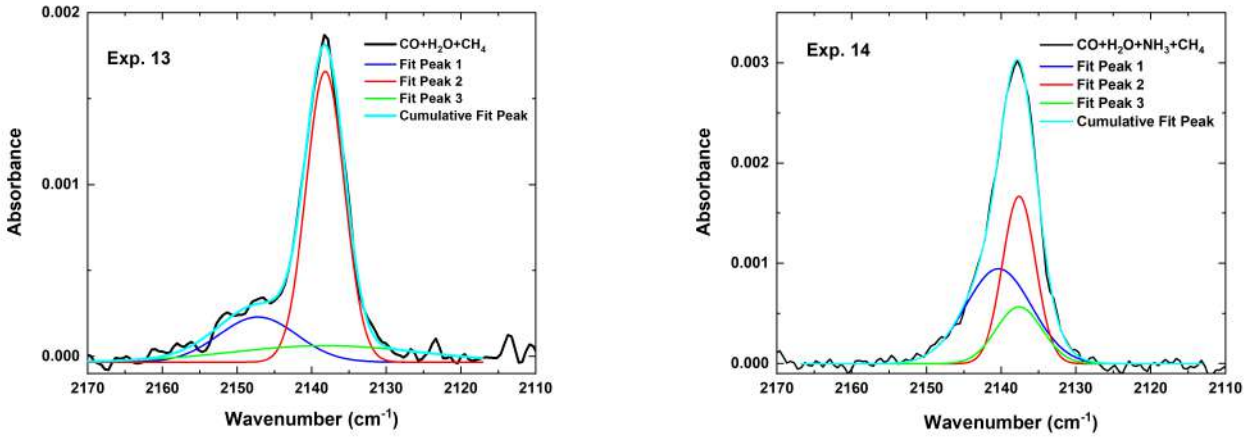

Figure 2: Continuation of Figure 2: Normal incidence infrared spectra (black lines) for experiments 13 – 14 listed in Table 3.1. Blue, red, and green curves indicate Gaussian components centered at high, intermediate, and low wavenumbers, respectively (see Table 3.2). Spectral resolution is 1 cm^{-1}.

the excess CH_3OH acts as a polar matrix that strongly perturbs the CO vibration, creating a wider distribution of interaction sites. Finally, the ternary mixture including CO_2 presents the broadest and most complex profile. The combination of methanol and CO_2 induces substantial structural disorder, resulting in a wide envelope that reflects the existence of multiple overlapping components arising from diverse molecular interactions.

3.3.1 Gaussian decomposition

To quantify these effects, the observed absorption bands were decomposed into a sum of Gaussian profiles. We employed the Levenberg–Marquardt algorithm for nonlinear least-squares optimization. Results are reported in Table 3.2, in which the various components are ordered from blue to red according to their central peak wavelength. We note that peak position and FWHM uncertainties are below the lowest spectral resolution (0.5 cm^{-1}). This approach reproduces both the intrinsic sharp feature of pure CO and the additional components arising from interactions with other species in mixed ices, providing a quantitative measure of the environmental heterogeneity experienced by CO molecules.

The properties of solid CO ice are highly sensitive to both the deposition technique (mode 1 vs. mode 2) and the chemical nature of the co-guests. We analyze the resulting phases by distinguishing between structural disorder, quantified by the FWHM of the CO stretching band, and chemical interaction indicated by the peak wavenumber shift (e.g., Sandford et al. 1988; Ehrenfreund et al. 1997).

In mode 1 (isothermal deposition), the stable 12 K substrate allows CO molecules to undergo sufficient local structural relaxation upon impact, enabling them to settle into an efficient, relatively ordered packing configuration that yields a characteristic narrow spectral feature (FWHM = 1.63 cm^{-1}) in the pure CO reference (experiment 1) at 2138.6 cm^{-1}, and a broader component likely arises by structural disorder at the ice boundaries and pore surfaces.

The presence of co-guests in mixed isothermal deposition consistently results in highly disordered CO phases, evidenced by broad FWHM values $\gtrsim$ 5 cm^{-1}. The loss of the narrow component shows that interaction with other molecular species, especially polar neighbors, substantially increases structural disorder, suggesting CO molecules are randomly dispersed and trapped within the matrix, experiencing a wide variety of binding energies. This is further illustrated by CO + CH_3OH mixtures, where strong chemical interaction causes the CO peak to shift significantly to 2134.6 cm^{-1} (experiment 17), which is the most red-shifted ($\sim$ 4 cm^{-1}) feature in the entire set. This pronounced shift indicates a qualitative difference in the electronic perturbation of CO compared to that in water and ammonia matrices. In water-rich ices, CO molecules are often trapped in relatively symmetric, constrained cages where local electric field

Table 3.2: Gaussian fitting of CO infrared profiles for the set of experiments described in Table 3.1.

exp.	composition	first peak (cm^{-1})	IA[(a)] (cm^{-1})	height	FWHM[(b)] (cm^{-1})	second peak (cm^{-1})	IA (cm^{-1})	height	FWHM (cm^{-1})	third peak (cm^{-1})	IA (cm^{-1})	height	FWHM (cm^{-1})	$R^{2(c)}$
isothermal deposition														
1	CO	2138.6	0.21	0.04	4.39	2138.4	0.44	0.25	1.63					0.9996
2	CO, H_2O	2149.2	0.07	0.006	10.87	2137.3	0.21	0.02	8.99					0.9997
3	CO, H_2O, NH_3	2139.7	0.13	0.008	15.14	2138.4	0.14	0.01	9.85					0.9998
4	CO, H_2O, CH_4	2149.2	0.11	0.01	9.35	2137.7	0.16	0.01	9.02					0.9938
5	CO, H_2O, NH_3, CH_4	2140.5	0.20	0.01	14.43	2137.9	0.07	0.009	7.71					0.9998
6	CO, CH_4	2138.8	0.21	0.04	4.17	2135.5	0.03	0.01	2.23					0.9998
15	CO, CO_2	2140.8	0.208	0.025	7.72	2137.9 n	0.05	0.01	4.89					0.9999
16	CO, CH_3OH (2:1)	2136.7	0.24	0.029	7.72	2134.9	0.01	0.005	3.53					0.9997
17	CO, CH_3OH (1:2)	2138.6	0.024	0.004	5.63	2134.6	0.25	0.02	8.90					0.9998
18	CO, CH_3OH, CO_2	2138.9	0.034	0.001	20.62	2138.9	0.19	0.02	8.09	2136.0	0.03	0.006	5.08	0.9991
simultaneous cooling and deposition														
7	CO	2138.5	0.008	0.005	1.36	2138.1	0.02	0.003	5.18					0.9968
8	CO, H_2O	2149.3	0.002	0.0002	7.42	2138.8	0.004	0.002	1.97	2138.6	0.01	0.002	7.01	0.9970
9	CO, H_2O, NH_3	2139.8	0.01	0.001	11.25	2138.7	0.0005	0.0004	1.24	2138.4	0.02	0.003	6.04	0.9985
10	CO, H_2O, NH_3	2139.8	0.05	0.003	11.89	2137.8	0.11	0.014	7.04	2137.6	0.01	0.004	2.32	0.9984
11	CO, H_2O, NH_3	2140.0	0.30	0.02	5.96	2137.9	1.02	0.12	3.29	2137.5	0.16	1.05	1.07	0.9985
12	CO, H_2O, NH_3	2139.4	1.12	0.67	6.25	2137.9	3.65	0.45	3.31	2137.4	0.52	0.19	1.03	0.9990
13	CO, H_2O, CH_4	2147.2	0.003	0.0002	12.26	2138.1	0.01	0.0016	6.0	2138.1	0.003	0.00006	29.6	0.9956
14	CO, H_2O, NH_3, CH_4	2140.3	0.01	0 .0009	10.47	2137.5	0.009	0.001	5.20	2137.5	0.004	0.0005	7.26	0.9974

(a) Integrated Absorbance (IA) defined as the total area under an absorption spectral feature; (b) Full Width at Half Maximum; (c) coefficient of determination.

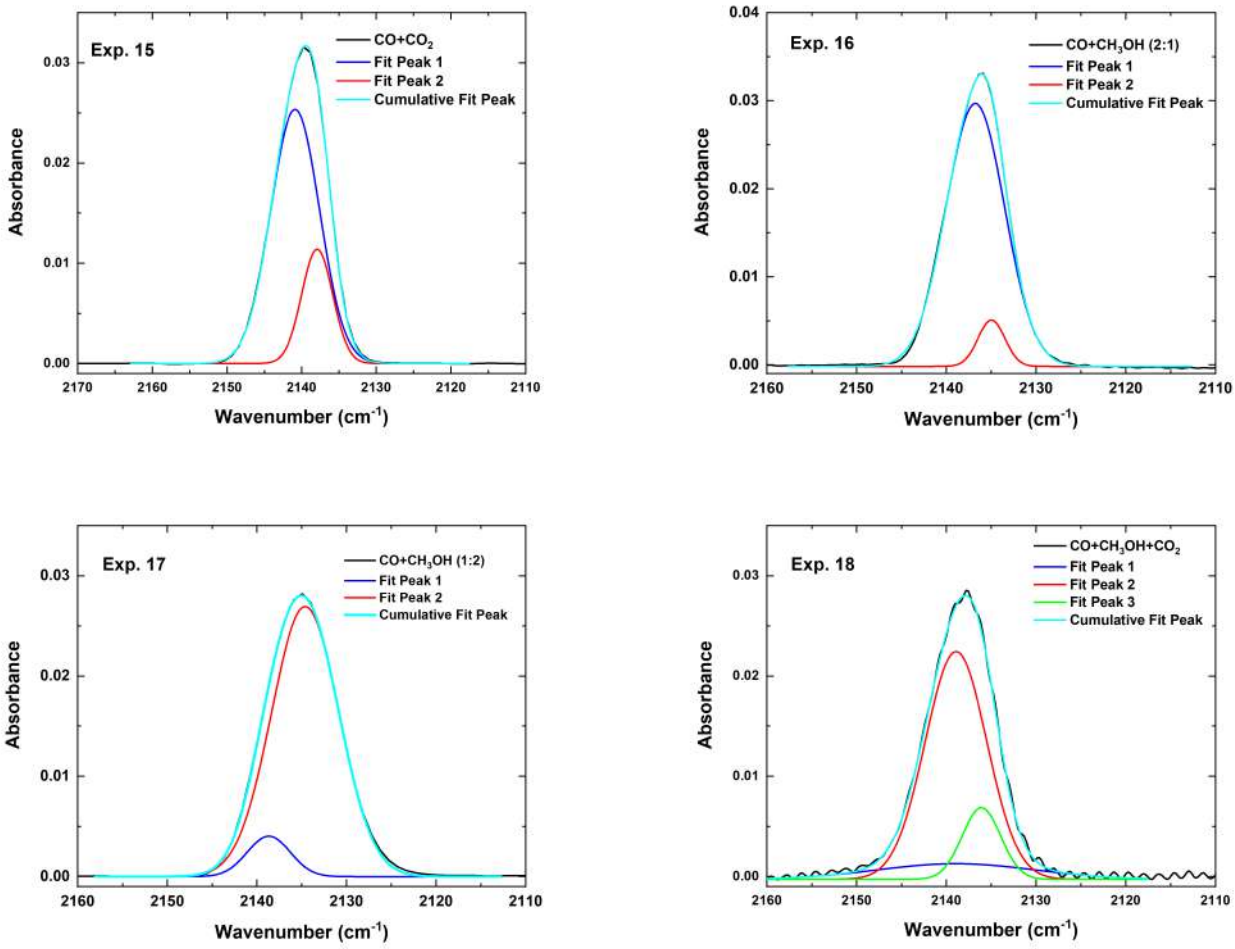

Figure 3.3: Normal incidence infrared spectra (black lines) are shown for four distinct ice mixtures, all deposited at a constant temperature of 12 K. Left top panel, CO:CO_2 2:1 ratio (experiment 15); right top panel CO + CH_3OH 2:1 ratio (experiment 16), left bottom panel, CO + CH_3OH 1:2 ratio (experiment 17); right bottom panel, ternary CO + CH_3OH + CO_2 ice mixture 2:1:1 ratio. Colored lines correspond to the various components of Gaussian fits (see Table 3.2), following the color convention of previous figures. The spectral resolution is 1 cm^{-1}.

vectors partially cancel out. In contrast, the methyl group in methanol prevents the formation of a high-symmetry lattice, resulting in a less constrained network where the O–H dipoles generate stronger, more directional local electric fields and specific interactions. These fields couple strongly to CO electronic structure, inducing a polarization that mixes antibonding $2\pi^\star$ character into the ground-state wavefunction, slightly reducing the effective C–O bond order (to ~ 2.98), and causing the observed red-shift in the stretching frequency.

In mode 2 (simultaneous cooling and deposition), the spectral profile of pure CO exhibits a coexistence of ordered and disordered phases, similar to that observed in mode 1. While the dominant component, $\sim 71\%$ of the Integrated Absorbance (IA), is a broad phase (FWHM = 5.18 cm^{-1}), which represents a primary amorphous and structurally strained CO matrix, the minor component is among the narrowest features (FWHM = 1.36 cm^{-1}), suggesting the presence of highly ordered domains. This high disorder in the dominant phase is attributed to kinetic trapping onto a structurally unstable substrate. Unlike the stable mode 1 surface, the rapid cooling in mode 2 creates a substrate that is under high internal stress and in a non-equilibrium conditions. CO molecules landing on this irregular film are immediately trapped into voids and strained position, limiting efficient local ordering and thus leading to the broad spectral profile. Significantly, the narrow, ordered feature persists as a minor phase

in layered ices, such as H_2O + CO (FWHM = 1.97 cm^{-1}, experiment 8) and H_2O + NH_3 + CO (FWHM $\lesssim$ 1.5 cm^{-1}, experiments 9 to 12), consistent with CO segregating into a relatively pure, ordered top layer despite the polar substrate below, thereby minimizing mixing with the bulk polar matrix. Conversely, the narrow CO component is absent in CH_4-containing ice mixtures (experiments 13 and 14), suggesting that methane acts as a structural disruptor that prevents the formation of these ordered domains.

Beyond structural disorder, the peak positions reveal distinct chemical environments. As widely reported in the literature, mixed ices containing polar molecules (experiments $2-5$) exhibit an underlying, much broader blue-shifted component (FWHM $\gtrsim$ 10 cm^{-1}), reflecting CO interaction with water or water–ammonia matrices. Infrared spectra of experiments 2 (H_2O + CO) and 4 (H_2O + CH_4 + CO) unambiguously reveal the presence of two distinct CO populations. The dominant component centered at $2137-2138$ cm^{-1} is attributed to CO molecules dispersed within the amorphous bulk of the water ice matrix, where they experience a variety of local environments. In addition, a weaker blue-shifted feature appears at $\sim$ 2149 cm^{-1}. This feature is commonly attributed to CO interacting with dangling OH (dOH) groups on amorphous ice surfaces. Computational studies (Zamirri et al., 2018) confirm this spectroscopic signature arises from the stiffening of the $C-O$ bond, caused by either a direct hydrogen bond with a dOH group or tight confinement within specific, small cage-like sites ($sIII_{grp2}$ sites). Despite these being distinct structural environments, both scenarios lead to the observed shift to higher wavenumbers. The computed oscillator strengths for all these blue-shifted modes are small, a finding that is entirely consistent with the weak intensity observed in laboratory spectra, and explains why these features are typically very hard to detect in astronomical observations of interstellar icy grains (He et al., 2022; Noble et al., 2024). This is further confirmed by the analysis of the water dangling bond features at $\sim 3600-3700$ cm^{-1}; as shown in Figure 3.4, the mixture exhibits a markedly more intense peak compared to the other experimental cases (experiments 2, 3, and 5), providing direct evidence of the enhanced porosity induced by methane. This suggests that while methane enhances the porosity of the ice, its non-polar nature prevents it from interacting strongly with the water surface. Consequently, the dangling-bond sites remain available to interact with CO, explaining the prominent blue-wing feature observed in the CO stretching mode for this mixture. In contrast, in the presence of a polar component like NH_3, the d-OH feature is suppressed because ammonia acts as a strong hydrogen-bond acceptor, preferentially occupying these sites and reducing the interaction between CO and the H_2O ice mantle. The necessary role of the water matrix is confirmed by the CO + CH_4 control experiment 6, where the $\sim$ 2149.1 cm^{-1} peak is entirely absent. Instead the spectrum displays an additional shoulder on the red side of the main CO profile, centered at 2135.5 cm^{-1} consistent with weak, dispersive interactions between CO and CH_4 (Figure 3.1). Similar trends are seen in spectra from mode 2 experiments 8 and 13, where the structural influence of methane on water ice persists despite the fact that layering effectively prevents CO and CH_4 from interacting with the H_2O bulk, thereby reducing the blue component that would arise from a mixed phase: the ratio of the absorbance integrated area is larger in experiment 13 (0.23) than in experiment 8 (0.14).

The incorporation of CO_2 into the ice lattice significantly perturbs the local environment of the CO molecules. In the binary CO + CO_2 mixture (experiment 15), the primary CO absorption feature is centered at 2140.8 cm^{-1} (FWHM = 7.72 cm^{-1}), This represents a distinct blue shift relative to the stretching frequency of pure bulk CO (van Broekhuizen et al., 2006). This shift suggests that the CO molecules are likely subjected to a 'stiffer' and more directional potential imposed by the quadrupolar CO_2 matrix. Computational studies suggest the importance of quadrupole moment to provide a reasonable description of the properties of the solid phase in carbon dioxide systems (Pérez-Sánchez et al., 2013). In the ternary CO + CH_3OH + CO_2 mixture (experiment 18), the CO band splits into three components. This behaviour likely arises because of the copresence of chemically distinct neighbourhoods.

The addition of the strong hydrogen-bond acceptor ammonia suppresses the $\sim$ 2149 cm^{-1} component in experiments 3 and 9 (CO + H_2O + NH_3). Instead, the CO band is dominated by polar-trapped features at or below 2140 cm^{-1}. This confirms that NH_3 chemically blocks the dOH sites by preferentially binding to them (Figure 3.4), preventing CO from forming the blue-shifted signature, as shown in He et al. (2022).

Finally, the comparison between experiments 5 (isothermally mixed) and 14 (layered), both quaternary mixtures, highlights the hierarchy of competing effects between NH_3 and CH_4 in

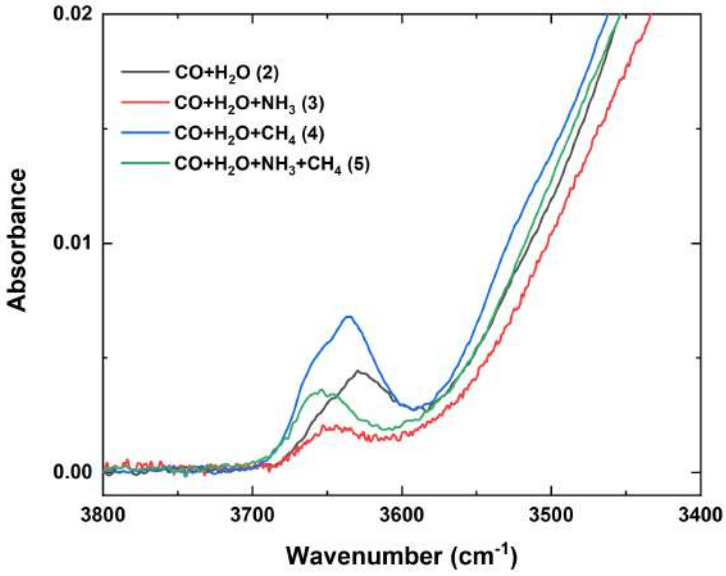

Figure 3.4: Infrared spectra of the water dangling hydroxyl (dOH) stretching region centered at approximately $3600 - 3700$ cm^{-1} for experiments 2, 3, 4, and 5. The profiles illustrate the variation in dOH intensity across different ice mixtures; the CO + H_2O + CH_4 mixture (experiment 4) exhibits the most prominent feature, indicating a higher degree of microporosity and a greater number of surface binding sites.

controlling CO − H_2O interactions, depending on the deposition conditions. The strong polarity and chemical reactivity of NH_3 produces a pronounced blocking effect that effectively outweighs the structural enhancement induced by CH_4. Specifically, although methane increases ice porosity and generates additional dangling dOH sites, ammonia binds preferentially to these sites, preventing CO adsorption and significantly reducing the blue-shifted CO feature. In the layered ice (experiment 14), the early condensation of H_2O and NH_3 allows ammonia to become thoroughly embedded within the water matrix, neutralizing available dOH sites before the subsequent CO and CH_4 condensation, thus yielding an interface largely devoid of active adsorption sites. Consequently, the chemical interaction of NH_3 is the dominant factor, controlling the outcome over the structural effects of CH_4 and the intrinsic porosity of the amorphous ice (see Figure 3.4). Methane, condensing later with CO, acts only as a secondary structural disruptor within the CO-rich layer, but this effect is negligible compared to the chemical influence of NH_3.

3.3.2 Longitudinal modes

To further probe the ice morphology, we examined the CO stretching band at an oblique infrared incidence of 45° to access its LO component. In our pure CO films this LO peak appears near 2143 cm^{-1} (whereas the main TO mode remains around 2138 cm^{-1}). While the CO absorption band in the multi-component mixtures exhibits only a geometric intensity scaling factor ($\sim$ 1.3) between normal and 45° incidence, the pure CO ices (experiments 1 and 7) show the characteristic signature of a TO/LO splitting, where the LO mode becomes distinct and visible. The absence of this LO mode splitting in the mixtures confirms their highly amorphous and disordered nature, produced by the random incorporation of H_2O, NH_3, and CH_4. A distinct LO band at $\sim$ 2143 cm^{-1} observed in pure CO ices (experiments 1 and 7, Figure 3.5) suggests that, although the ice is globally amorphous, the film acts as a continuous dielectric medium capable of supporting collective longitudinal oscillation, consistently with the behavior reported by He et al. (2021).

A direct comparison between left (isothermal deposition at 12 K) and right (cooling plus deposition) panels in Figure 3.5 reveals that the local structural homogeneity of the CO ice

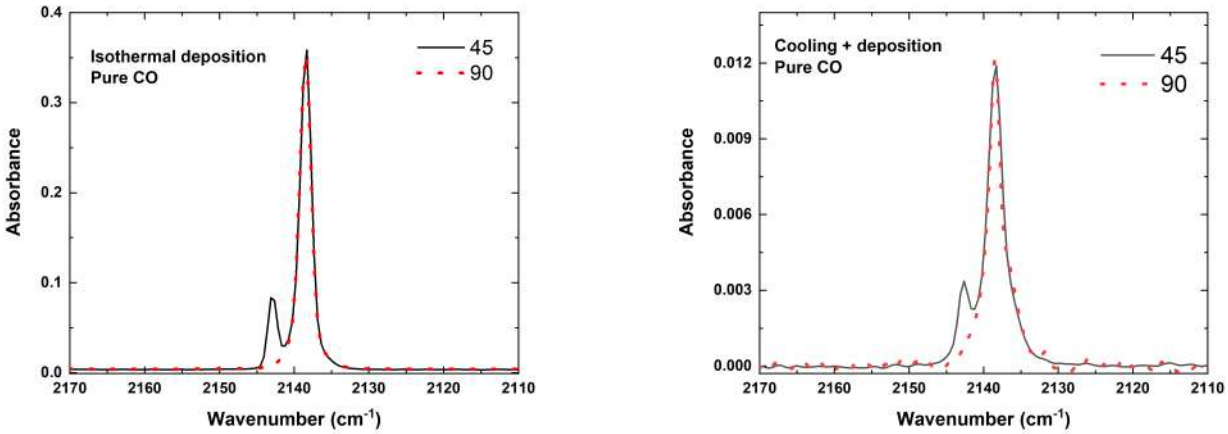

Figure 3.5: CO stretching absorption band for pure CO ice recorded at oblique (45°, black solid line) and normal (90°, red dashed line) incidence. Left panel: isothermal deposition (mode 1) at a constant temperature of 12 K; right panel: CO ice deposited while the substrate temperature was decreasing (mode 2). Both deposition methods result in spectra that show the $C-O$ stretching absorption band near ~ 2138 cm^{-1}, displaying TO mode and a distinct LO mode at ~ 2143 cm^{-1}. The TO mode intensity is scaled by a factor of ~ 1.3 relative to the oblique incidence spectrum. The spectral resolution is 1 cm^{-1}.

is sensitive to the deposition history. While both films exhibit the LO mode, the band profiles in cooling plus deposition mode are noticeably broader and more blended. This increased inhomogeneous broadening suggests a wider distribution of local CO environments (site-to-site disorder) in the ramped case. CO deposited at 30 K isothermal conditions would adopt a crystalline, ordered structure. However, mode 2 protocol is a dynamic process where the substrate temperature is continuously decreasing. Thus, each new layer of CO is deposited at a different temperature and onto a previous layer that is already contracting due to cooling. This creates a vertical gradient of thermal stress that prevents the formation of a cohesive, long-range crystalline lattice throughout the thickness of the ice. Instead, the ice consists of a stack of structurally mismatched layers, which leads to the site-to-site variability (inhomogeneous broadening) we observe. The LO spectra thus confirm the role of dynamic deposition conditions: the constant change in surface mobility and surface energy during the cooling from ~ 30 K (the initial temperature from which CO starts depositing) to 12 K, kinetically traps CO molecules in a greater variety of non-equilibrium packing arrangements. In contrast, the constant temperature of 12 K in mode 1 favors the growth of a CO phase with a more uniform lattice, yielding sharper, better-resolved TO and LO features.

These results suggest that the inhomogeneous broadening of the CO band, which reflects local molecular packing, is sensitive to the deposition's thermal history. This sensitivity provides a diagnostic tool, as cooling and heating protocols produce fundamentally different structural environments. While heating traditionally leads to the annealing and homogenization of ice, the cooling ramp employed here induces vertical stratification and cumulative thermal stresses. Because these structural changes are inherently irreversible, the resulting spectral profiles remain distinct from those of purely heated or isothermal ices. Consequently, these specific spectral signatures provide a reliable means in discriminating between interstellar grains that have experienced cooling cycles versus those that have undergone subsequent thermal annealing.

3.3.3 The CO - CH_3OH interaction

In modeling the chemical evolution of icy mantles in dense molecular clouds, the outermost CO-rich layer is critically important; it represents the final stage of ice stratification and serves as the primary site for late-stage surface chemistry. The vibrational profiles of CH_3OH in various ice matrices (experiments $16-18$; Figure 3.6) were analyzed via Gaussian deconvolution, and the results are summarized in Table 3.3. While peak position uncertainties remain within the minimum resolution (0.5 cm^{-1}), consistent with CO fitting results, uncertainties in the FWHM

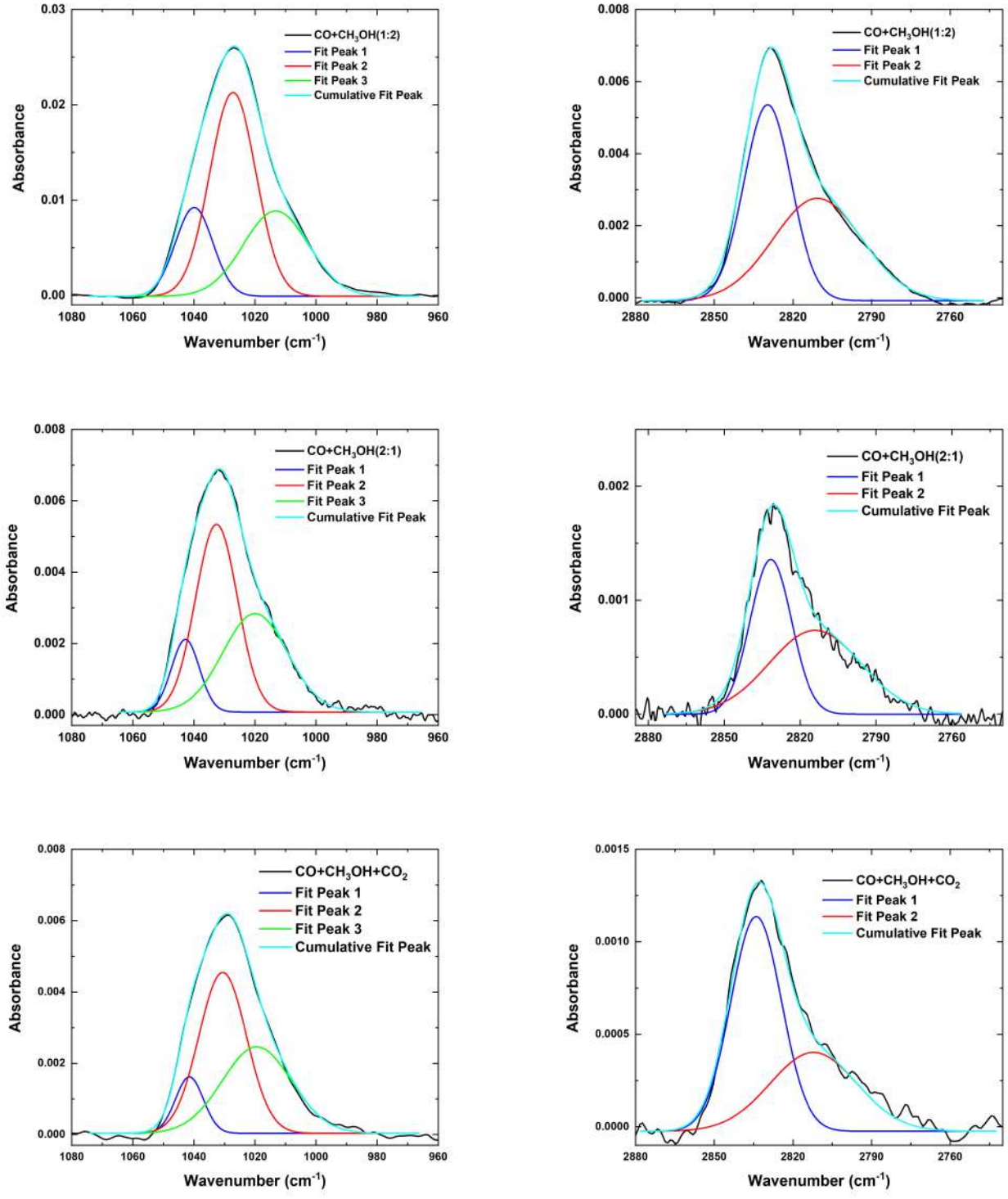

Figure 3.6: The spectra display the vibrational regions for the C-H stretch (left panels) and the C-O stretch (right panels) of methanol diluted in CO and CO + CO_2 matrices. Panels illustrate concentration and composition effects: top, CO:CH_3OH = 2:1; middle, CO:CH_3OH:CO = 1:2; bottom, CO + CH_3OH + CO_2.

values are inherently higher, but never exceed $2-3$ cm^{-1}. The data reveal that the C–O and C–H stretching modes respond distinctly to the surrounding CO and CO_2 environment.

The significant electronegativity difference in the C–O bond ($\Delta\chi = 0.89$ in the Pauling scale) results in a larger dipole moment change during vibration compared to the weakly polar C–H bonds ($\Delta\chi = 0.35$). As a result, the C–O stretch is more strongly coupled to the local electrostatic environment, making it highly sensitive to hydrogen bonding and matrix composition. This explains why the C–O band necessitates a three-component fit to resolve the complex variety of molecular sites, whereas the C–H bonds effectively average these environments, requiring only two Gaussian components. The C-O stretching feature displays significant frequency shifts relative to pure methanol ice (1028 cm^{-1}; Müller et al. 2021), which we interpret as a response to the local degree of hydrogen bonding. The central component ($1027-1032$ cm^{-1}), aligning well with the reference value for amorphous methanol, is assigned to bulk-like CH_3OH self-interactions. This assignment is supported by the integrated area, which reaches a maximum of 0.407 cm^{-1} in the methanol-rich experiment 17. A narrow, blue-shifted component ($\sim 1040-1043$ cm^{-1}) is observed with a relatively low FWHM (~ 11 cm^{-1}). We attribute this to a population of methanol molecules with reduced hydrogen-bond connectivity, such as monomers or small oligomers isolated in the matrix cages. This is supported by a lower shift in experiment 17, because, in a crowded environment, even isolated molecules feel some pull from nearby methanols. Conversely, a broad, red-shifted component ($\sim 1013-1020$ cm^{-1}) exhibits the highest FWHM (~ 25 cm^{-1}). This feature likely represents a distribution of disordered sites at the interface between methanol clusters and the matrix, or specific interactions with CO_2 (in experiment 18) that perturb the C-O oscillator. In contrast to the multi-modal shifting of the C-O band, the C − H stretch responds to the environment through bimodal splitting and significant broadening. The first C − H component ($\sim 2830-2834$ cm^{-1}) corresponds to bulk-like environments (2829 cm^{-1}, Müller et al. 2021), while the second component ($\sim 2810-2814$ cm^{-1}) is significantly red-shifted and broadened. The FWHM of this secondary component reaches a maximum of 42.87 cm^{-1} in the CO-rich experiment 16, nearly double the width of any C-O component. This underscores the high degree of structural heterogeneity and interaction experienced by the methyl group when embedded in a CO-rich matrix.

3.4 Discussion

The spectroscopic analysis performed in Section 3.3 decomposes the CO profiles into Gaussian components that serve as distinct spectroscopic indicators used to quantitatively define concurrent chemical environments. The standard astrochemical populations (Boogert et al., 2015) are recognized based on the data reported in Table 3.2, where the peak wavenumber reflects the dominant intermolecular interaction, and the FWHM characterizes the structural disorder and local constraint experienced by CO within the ice mantle. The most significant distinction in our experimental framework arises from the thermal history imposed by the deposition protocol, which produces measurable differences in these spectroscopic indicators, as illustrated in Figure 3.7. Isothermal deposition at 12 K (mode 1) results in homogeneous mixed ices. In this highly disordered structure, CO molecules are forced into close proximity with all neighboring species, both polar and non-polar, leading to peak positions that are strongly dependent on the host matrix. This behavior is illustrated by the substantial band broadening and red-shifting observed in the CH_3OH-rich mixtures of experiment 17 (e.g., the CO feature centered at 2134.6 cm^{-1}). In contrast, the simultaneous cooling and deposition protocol (mode 2) promotes chemical and structural segregation, producing layered ice structures. In this case, CO molecules that accumulate in the outer layer largely avoid the strong electrostatic influence of the underlying polar-rich phases. As a consequence, the CO absorption bands are narrower, more symmetric, and clustered around the pure CO band position, providing a clear spectroscopic signature of structural order. These spectroscopic results provide new insight into the chemical and structural architecture of interstellar and circumstellar ices on dust grains. The CO band profile requires multiple Gaussian components because the ice structure is intrinsically non-uniform, consistent with studies of other mixed ices such as CH_3OH (Müller et al., 2021). This decomposition is necessary to reproduce the spectral disorder arising from the broad distribution of kinetically trapped binding sites, particularly in the mode 1 deposition experiments.

Our laboratory fitting procedure provides a library of 43 Gaussian components, whose defining parameters, band center ν_j and FWHM (σ_j = FWHM/2.355), are listed in Table 3.2. In

Table 3.3: Gaussian fitting of methanol vibrational C-H and C-O stretch profiles

exp.	transition	first peak (cm^{-1})	$IA^{(1)}$ (cm^{-1})	height	FWHM (cm^{-1})	second peak (cm^{-1})	IA (cm^{-1})	height	FWHM (cm^{-1})	third peak (cm^{-1})	IA (cm^{-1})	height	FWHM (cm^{-1})	R^2
16	C-H stretch	2831.6	0.027	0.001	19.27	2814.1	0.033	0.0007	42.87					0.9892
	C-O stretch	1042.9	0.023	0.002	10.98	1032.6	0.09	0.005	16.28	1020.1	0.074	0.002	25.16	0.9981
17	C-H stretch	2829.7	0.12	0.005	21.26	2810.6	0.12	0.002	39.78					0.9986
	C-O stretch	1039.9	0.143	0.009	14.44	1027.2	0.407	0.021	17.88	1013.1	0.239	0.008	25.20	0.9994
18	C-H stretch	2834.0	0.028	0.001	19.31	2812.1	0.017	0.0004	33.20					0.9915
	C-O stretch	1041.5	0.018	0.001	10.74	1030.5	0.088	0.004	18.36	1019.3	0.069	0.002	26.84	0.9980

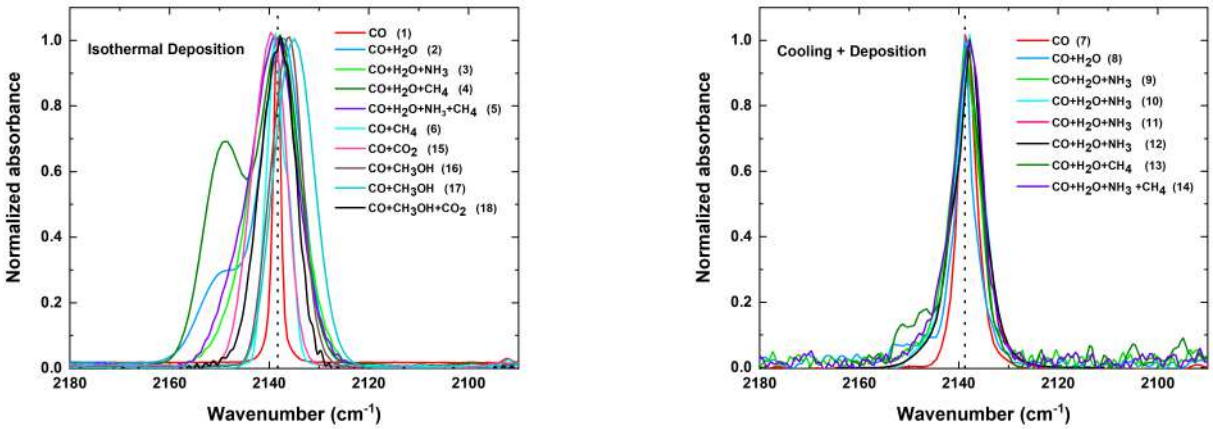

Figure 3.7: Normalized spectra for the whole set of experiments performed in mode 1 (left panel) and mode 2 (right panel). The vertical dashed black line marks the peak position of pure CO ice. Numbers refer to the experiment list reported in Table 3.1.

our analysis, each Gaussian component is treated as an independent tracer of a specific chemical–structural state of solid CO. By applying this component library to astronomical spectra, we overcome the limitations associated with fitting observations using global laboratory spectra alone. Although not all resolved environments are always clearly distinguishable or physically intuitive (some may be transient or only occur in particular configurations), the resulting fits may provide a robust test of physical coherence when compared against astrophysical spectra. For example, the presence of a strongly blue-shifted CO band (e.g., near 2150 cm^{-1}) in an environment dominated by pure CO and lacking polar species would be physically anomalous, thereby validating the environmental assignments. In this way, individual Gaussian components are elevated from simple fitting parameters to fundamental spectroscopic building blocks, enabling a direct translation of laboratory-determined physical and chemical conditions into the structural composition of interstellar and circumstellar ices. This framework is applied to observational data in the following section.

3.4.1 Mapping concurrent CO environments in astronomical ices

In this section we apply the laboratory library of Gaussian components to CO absorption features observed toward two molecular clouds and one protoplanetary disc. The aim is not to uniquely identify a specific ice morphology, but to determine which combinations of the experimentally calibrated CO environments are required, and which are excluded, by the astronomical spectra. By decomposing each feature into the same set of fundamental spectral indicators derived in the laboratory, we quantify the concurrent presence of segregated CO, CO mixed within polar matrices (e.g., CH_3OH- or H_2O-rich environments), and CO residing in disordered amorphous sites. Through this approach we may assess the degree of chemical and structural heterogeneity in the ices and to compare how these environments vary among quiescent molecular cloud material, more processed star-forming regions, and protoplanetary disc environments shaped by thermal and dynamical evolution. In this sense, the laboratory Gaussian library may in principle provide a physically grounded diagnostic framework for evaluating whether the observed ices are predominantly layered, fully mixed, or occupy intermediate structural configurations.

To this end, we have selected three sources observed with the JWST. The first two are the background stars NIR38, $A_V = 60$ mag, and J110621, $A_V = 95$ mag, in the Chameleon 1 star-forming region (McClure et al., 2023), which sample ice in dense, quiescent molecular clouds. The third source is the protoplanetary disc HH 48 NE (Bergner et al., 2024), which provides insight into ice composition in a more dynamically and thermally processed environment. These targets were chosen as representative examples of distinct astrophysical contexts, rather than for any specific shared physical property. Our analysis focuses on the CO ice absorption band centered near 2138 cm^{-1}, which is a sensitive tracer of both the molecular mixing matrix and

Table 3.4: Relative contributions of laboratory derived Gaussian components to the astronomical spectral fits

source	n_G	exp.	peak	wavenumber (cm^{-1})	$\sigma^{(a)}$ (cm^{-1})	${A_j}^{(b)}$ (%)	m (cm)	q	$(f_{\rm lab})_j$	$(f_{\rm obs})_j$
NIR 38	2	11	1	2140.0	2.53	0.8734	0.0	0.080	20	78
		17	2	2134.6	3.78	0.1605			91	22
J 110628	2	11	1	2140.0	2.53	0.8941	-0.0086	1.914	20	90
		17	2	2134.6	3.78	0.0614			91	10
HH 48 NE	4	9	1	2139.8	4.76	0.5058	0.0010	-2.334	33	57
		3	1	2139.7	6.41	0.1636			48	25
		11	1	2140.0	2.53	0.1589			20	10
		17	2	2134.6	3.78	0.0928			91	8

(a) FWHM $= 2.355 \times \sigma$; (b) spectra are normalized to their maximum value.

the thermal history of the ice. The observed absorption profile is modeled using our laboratory-calibrated Gaussian library. Specifically, the fitting function $F(\nu)$, where ν is the wavenumber in cm^{-1}, is defined as a linear combination of $n_G = 43$ Gaussian components derived from laboratory ice experiments, plus a linear baseline

$$F(\nu) = \sum_{j=1}^{n_G} A_j \, G_j(\nu;, \nu_j, \sigma_j) + m\nu + q \tag{3.1}$$

where each Gaussian G_j is fully characterized by a fixed central wavenumber ν_j and dispersion σ_j (or equivalently FWHM), as listed in Table 3.2. These parameters are determined independently from Gaussian decompositions of CO stretching profiles measured in pure and mixed laboratory ices and are held fixed in the astronomical fits. The only free parameters associated with the Gaussian components are their amplitudes A_j, which quantify the contribution of each laboratory-defined CO environment to the observed spectrum. Gaussian components that are not required by the data naturally converge to $A_j = 0$. The additional free parameters m and q account for a local linear baseline. With this approach, the astronomical CO ice profiles are not fit by arbitrarily adjusting band positions or widths, but instead by determining the optimal linear combination of experimentally calibrated spectral components, providing a physically grounded measure of the relative importance of different CO ice environments. Therefore, we employ an ordinary least squares regression technique with non-negativity constraints on the Gaussian amplitudes. Since all non-linear parameters of the model, namely the central wavenumbers and widths of the Gaussian components, are fixed a priori from laboratory measurements, this reduces the spectral decomposition to a linear problem, in which only the amplitudes of the Gaussian bases and the coefficients of the linear baseline are optimized. The resulting best-fit profiles are shown in Figure 3.8, and the corresponding fitting parameters are reported in Table 3.4. In this table, n_G denotes the number of components with positive amplitudes $A_j > 0$, while $(f_{\rm lab})_j$ and $(f_{\rm obs})_j$ represent the normalized contributions of the specific Gaussian features within the laboratory and astronomical spectra, respectively.

All sources are analyzed using the same library of 43 Gaussian components derived from the single, self-consistent set of laboratory experiments reported in Table 3.1. Applying this procedure, we find that only a small subset of the available laboratory-derived basis functions is required to reproduce the observed CO ice profiles. In particular, the NIR38 spectrum is adequately described by two Gaussian bases, as is J110621, while the protoplanetary disc HH 48 NE requires four components. Notably, the two molecular cloud sightlines are reproduced by the same pair of Gaussian profiles. These same two laboratory-defined components are also present in the fit to the disc spectrum, which additionally requires two further Gaussian bases to account for its increased spectral complexity. The final model therefore involves only four Gaussian components in total.

Two Gaussian components are common to all three sources: experiment 11 (peak 1) and experiment 17 (peak 2). This selection offers an interpretable chemical and structural picture of the ice mantles. Experiment 11 was produced to mimic a layered morphology in which a polar sub-layer (H_2O and NH_3) is overlain by a CO top-layer (an outcome of the chosen

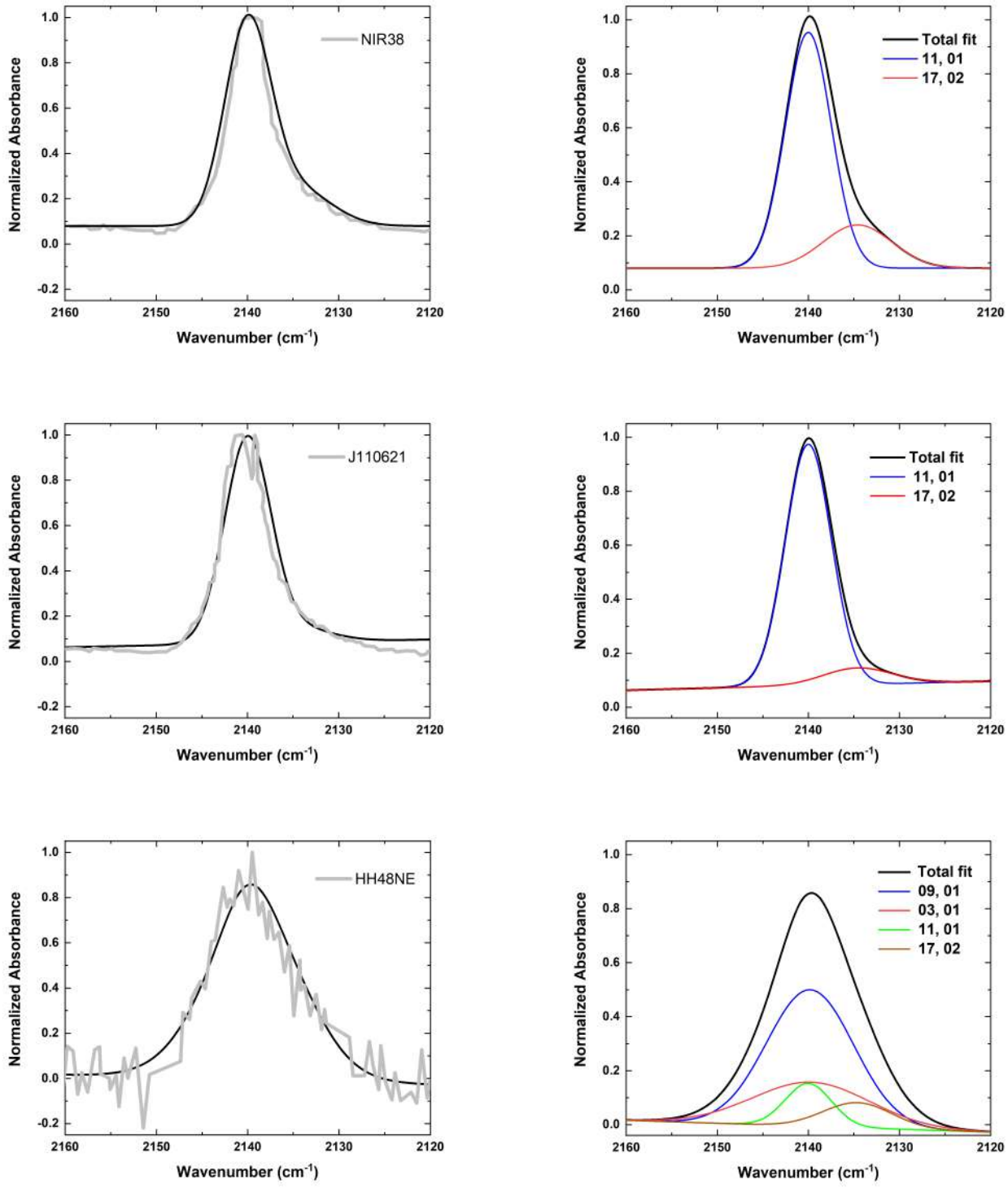

Figure 3.8: Left panels: fitting profiles for the CO ice absorption band toward three astronomical sources, the dense cloud sightlines NIR38 and J110621 (McClure et al., 2023), and the protoplanetary disc HH 48 NE (Bergner et al., 2024). The fit has been performed using the Gaussian decomposition, equation (3.1), based on our laboratory-derived ice components. The original JWST spectra are displayed as thick gray lines, while the total fitting profile (representing the sum of all Gaussian components) is shown as a solid black line. Right panels: individual Gaussian components constituting the total fit; labels identify the specific laboratory and the derived ice environment (the peak) selected by the fitting procedure.

deposition mode). The presence of the experiment 11 (peak 1) component in all fits therefore indicates a CO population that is interacting with water and ammonia primarily at the layer interface (mode 2). In the context of our non-negative least squares fits, the requirement of this component implies that CO embedded in a polar interfacial environment contributes significantly to the observed absorption; conversely, the fit does not demand a substantial contribution from the pure, non-polar bulk CO that would be expected from an unperturbed top layer (peaks 2 and 3). The requirement of experiment 17 (peak 2) further indicates that the CO residing in the top layer is not purely apolar but is mixed with methanol. Taken together, these results are most naturally interpreted as a layered ice structure with chemically distinct phases: a polar, H_2O/NH_3 interfacial region and a top-layer in which CO is mixed with significant amount of CH_3OH. In other words, experiment 17 (peak 2) substitutes experiment 11 (peaks 2 and 3). This description is consistent with a stratified ice mantle.

The CO ice profile observed toward the protoplanetary disc exhibits a substantially more complex and dynamically processed structure than those along the molecular cloud sightlines. While a layered ice morphology remains relevant, the dominant contribution arises from a component spectrally identical to experiment 11 (peak 1), but originating from experiment 9 (peak 1), where the same Gaussian profile is produced under markedly different deposition conditions. In experiment 9, the significantly lower deposition pressure results in a thinner CO layer, enhancing the relative contribution of CO molecules interacting with the underlying polar substrate. This component alone accounts for approximately $(f_{\rm obs})_{9,1} = 57\%$ of the total CO absorption in the disc. The second major contribution is associated with the mixed ice environment represented by experiment 3, indicative of CO trapped within a polar matrix (still with water and ammonia), $(f_{\rm obs})_{3,1} \sim 25\%$. In contrast, only a minor fraction of the signal ($< 20\%$) is attributable to chemically more evolved layered environments involving CO$-CH_3OH$ interactions (experiments 11 and 17). The fact that the same spectral component (peak 1) emerges both from a thick, layered ice (experiment 11) and from a thin, low-pressure deposition ice (experiment 9) underscores that this Gaussian profile traces CO molecules interacting with polar species at or near an interface, rather than uniquely encoding a specific ice thickness or deposition history. In the disc, the dominance of this component suggests that a large fraction of CO resides in interfacial or substrate-influenced environments, consistent with recent freeze-out onto pre-existing polar mantles. The smaller contribution from methanol-bearing components can be tentatively associated with a more chemically processed ice fraction, potentially inherited from earlier evolutionary stages, whereas the prevalence of interfacial and mixed components points to ongoing thermal or dynamical reprocessing within the disc. Overall, these results reinforce the conclusion that the CO ice band shape in discs is governed by a limited set of physical processes, interfacial interactions with polar species, matrix trapping due to mixing, and chemical hydrogenation, rather than by a wide diversity of distinct ice morphologies.

3.5 Conclusions

In this work, we have investigated how the infrared absorption profile of the solid-state CO stretching mode reflects the chemical and structural environments established during ice growth under astrophysically relevant conditions. Using two complementary deposition protocols, standard isothermal co-deposition at 12 K and a temperature-decreasing ramp that simulates accretion during grain cooling, we produced a comprehensive set of mixed and layered CO ices containing H_2O, NH_3, CH_4, CO_2, and CH_3OH. By systematically mapping laboratory conditions onto a Gaussian component library, we find that the CO line profile reflects both the structural state of the ice, ranging from ordered, layered configurations to disordered or mixed environments, and the specific chemical composition of the local CO molecular neighborhood.

The application of this laboratory-calibrated framework to astronomical CO ice spectra shows that both molecular cloud and protoplanetary disc environments can be described in terms of a limited number of dominant micro-architectures. All sources were analyzed using the same library of 43 Gaussian components derived from a single, internally consistent set of laboratory experiments. From this full basis, only a small subset of components is required to reproduce the observed profiles: the two molecular cloud sightlines (NIR38 and J110621) are each described by the same two Gaussian bases, while the protoplanetary disc HH 48 NE requires two additional components to account for its increased spectral complexity. The final model therefore involves only four Gaussian components in total, two of which are common to all three sources, indicating that the diversity of observed CO ice profiles can be traced back

to a small number of physically meaningful environments.

A key result emerging from this blind, non-negative least-squares fitting procedure is that one Gaussian component common to all three sources originates from a laboratory experiment that necessarily includes ammonia in the polar substrate. The selection of this component is not imposed a priori, but is driven by the data: no ammonia-free laboratory profile within the present library reproduces this spectral contribution with comparable fidelity. This finding does not imply that ammonia is abundant throughout the CO ice mantles, but rather that the local CO environments contributing most strongly to the observed absorption require a degree of polarity consistent with interactions involving NH_3, together with H_2O, at interfaces or within polar regions. In this sense, ammonia acts as a structural modifier of the polar matrix that measurably affects the CO vibrational response.

The disc spectrum further reveals a redistribution among these micro-environments, with a dominant contribution from interfacial CO formed under low-pressure, cooling-driven deposition conditions, a substantial fraction of CO trapped within mixed polar matrices, and only a minor contribution from chemically mature, methanol-bearing layered structures. This combination is consistent with an evolutionary scenario in which recently accreted CO ices coexist with more processed material and undergo ongoing thermal or dynamical reworking. While necessarily schematic, this interpretation highlights the physical and chemical processes, interfacial interactions with polar species, matrix trapping due to mixing, and chemical hydrogenation, that most strongly shape the CO ice band.

Finally, while the present experimental set provides clear indications on the nature of the CO micro-environment, it also highlights important limitations inherent to our approach. In this study, we restrict the analysis to the CO stretching mode near 2138 cm^{-1}, whereas a fully self-consistent reconstruction of astrophysical ice mantles requires the contemporaneous modeling of multiple ice absorption bands within a unified experimental and fitting framework. In this context, the results presented here should be viewed as a first, CO-centered step, providing a physically motivated reference for the design of future multi-component laboratory experiments aimed at constructing a comprehensive structural model of astrophysical ice mantles.

A. The role of substrate

Progress in the understanding of various grain–ice systems (e.g., Cuppen et al. 2017) has shown that obtaining clear clues about dust–ice interaction from laboratory experiments remains a significant challenge. This opens the way to investigate how the substrate dictates both the chemical evolution of the ice and its spectroscopic response. While laboratory studies often utilize infrared-transparent materials like KBr, CsI, or ZnSe, these standard substrates lack the complex surface properties of actual interstellar dust. Even without external irradiation, the presence of a realistic mineral substrate can fundamentally modify the interaction at the interface.

The electrostatic interactions, stemming from surface ions, dangling bonds, and local electric fields, polarize the molecular layers, directly perturbing their vibrational energy levels. Furthermore, the physical geometry of the surface, such as the roughness and porosity created e.g., by grinding a mineral, influences the orientation and packing of the ice. These factors are explicitly manifested in the spectroscopic line profiles, where the coupling between the ice and the mineral surface induces frequency shifts, inhomogeneous broadening, and changes in band symmetry. Consequently, the line profiles provide a direct probe of the structural and electronic influence of the grain, demonstrating that the substrate is not a passive carrier but a primary driver of the ice's observed spectroscopic signature. To explore these effects, we compared results obtained with a standard CaF_2 window with a substrate of ground meteoritic material (an H chondrite). As in the experiments described in the above Chapter, we used the two different deposition modes described in Section 3.2, selecting some chemical composition among the ones reported in Table 3.1.

A.1 The nature of the surface

To investigate the potential influence of the substrate on the formation of spectral line profiles, we deposited a pulverized meteorite sample onto an underlying CaF_2 window. Specifically, we utilized an ordinary H chondrite collected in the province of Tata, Morocco (Aboulahris et al., 2019). This class of meteorite is characterized by a high total iron content and a significant proportion of metallic Fe–Ni ($15-20\%$ by mass), alongside a silicate mineralogy predominantly composed of bronzite, olivine, pyroxene, and plagioclase distributed within relatively small chondrules (Ostrowski & Bryson, 2016). Furthermore, studies of H chondrites frequently reveal evidence of impact-induced shock metamorphism dating back to the first 100 million years of the Solar System (Amelin & Ireland, 2013). This asteroidal, highly crystalline material differs significantly from the largely amorphous, pristine dust particles characteristic of dense molecular clouds. Moreover, unlike carbonaceous chondrites, which formed in the outer, colder regions of the protoplanetary disc, H chondrites are believed to have originated in the inner Solar System, well within the water snow line. As a consequence, their parent bodies never accreted an ice mantle, and remained dry rocky-metallic aggregates. This is confirmed by the near-total absence of aqueous alteration products (like clays) and the preservation of abundant metallic iron, which would have oxidized rapidly had a substantial layer of ice melted and permeated the rock (Morbidelli et al., 2016). However, its complex history is highly advantageous for our laboratory simulations. The combination of metallic inclusions, varied silicate phases, and impact-induced micro-structural defects produces a highly irregular topography and an intricate electrostatic environment. We exploited this rich, heterogeneous mineral surface as a working example to explore whether the intrinsic structural and electronic properties of a natural substrate drive variations in the infrared line profiles through heterogeneous broadening, frequency shifting, or band asymmetry. On this meteoritic support, we replicated the deposition protocols previously performed on the bare reference window.

A.2 Experiments

The ice experiments described here were performed with the LIFE facility, using the diagnostic instrument suite described in Section 2.2. For this new set of experiments we exploited a ZnSe window, and we perform experiments with and without depositing the meteoritic powder on the window. The deposition pressure was set to 1.5×10^{-7} mbar.

The complete set of experiments, detailed in Table A.1, comprises a total of ten depositions designed to isolate the substrate's influence on the spectroscopic response of the ice. Each configuration was replicated across two distinct environments: a reference bare ZnSe window and the same support coated with ground meteoritic material. For pure CO, a set of four experi-

Table A.1: List of experiments and ice description with and without meteorite.

exp.	composition	pre-mixing ratio	final ratio	deposition mode	ice type	substarte	CO (ML)
1	CO			1	pure	ZnSe	86
2	CO			2	pure	ZnSe	84.3
3	CO			1	pure	ZnSe+meteorite	52
4	CO			2	pure	ZnSe+meteorite	50
5	CO, H_2O, NH_3		1 : 2 : 1	1	mixed	ZnSe	79
6	CO, H_2O, NH_3	3 : 2 : 1	1 : 1.8 : 1	2	layered	ZnSe	82.9
7	CO, H_2O, NH_3	6 : 2 : 1	1.3 : 1.7 : 1	2	layered	ZnSe	83.8
8	CO, H_2O, NH_3		1 : 1.3 : 1.2	1	mixed	ZnSe+meteorite	56.4
9	CO, H_2O, NH_3	3 : 2 : 1	1 : 2 : 1.1	2	layered	ZnSe+meteorite	102
10	CO, H_2O, NH_3	6 : 2 : 1	1.1 : 1.5 : 1	2	layered	ZnSe+meteorite	83.4

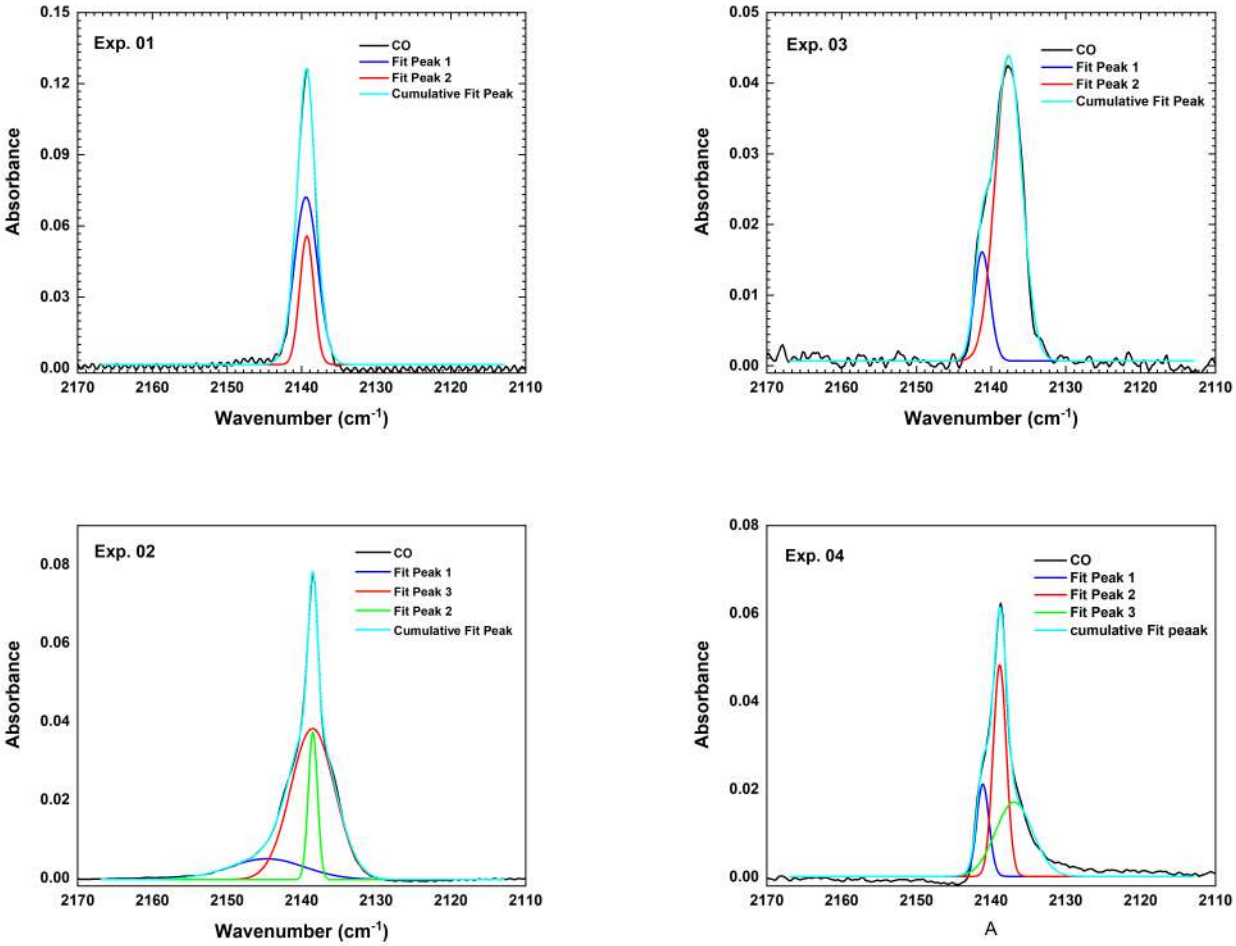

Figure A.1: Comparison of infrared absorption spectra for pure CO ices deposited at 10 K. The left column displays experiments performed on the bare ZnSe reference window, while the right column shows the corresponding depositions on the ground meteorite powder. The top panels correspond to mode 1 (direct deposition), and the bottom panels correspond to mode 2.

ments (experiments $1-4$) was performed by crossing both substrate types with two different deposition methods (mode 1 and mode 2). The investigation was further extended to a ternary mixture of H_2O, NH_3 and CO to observe more complex interactions. This subset includes two experiments conducted in mode 1, repeated on both substrates, and four experiments utilizing a layered approach (mode 2). For these layered depositions, two different initial CO ratios were tested to evaluate how concentration affects the ice structure when in contact with the mineral surface. This experimental design, combining the 4 pure CO runs, the 2 mixed ternary runs, and the 4 layered ternary runs, allows for a clear distinction between line profile variations caused by the molecular environment (pure vs. mixed vs. layered) and those specifically induced by the physical presence of the meteorite. The results of our experiments are presented in Figures A.1 and A.2, which visually compare the spectroscopic behavior of ices on a bare window versus a meteoritic substrate. As in Section 3.3.1 we applied a Gaussian deconvolution to all the experimental CO spectra. Results are reported in Table A.2, in which the various components are ordered from blue to red according to their central peak wavelengths.

When CO is deposited in a pure state on a flat, relatively inert ZnSe substrate, as done in experiments 1 and 2, the resulting profiles are remarkably sharp and symmetric. These peaks, centered near 2138 cm^{-1} , represent an ideal environment where CO molecules are surrounded by their own kind, leading to a crystalline-like arrangement with minimal spectral broadening. However, the introduction of the meteorite substrate in experiments 3 and 4 immediately disrupts this simplicity. Even with pure CO, the transition to the meteorite induces

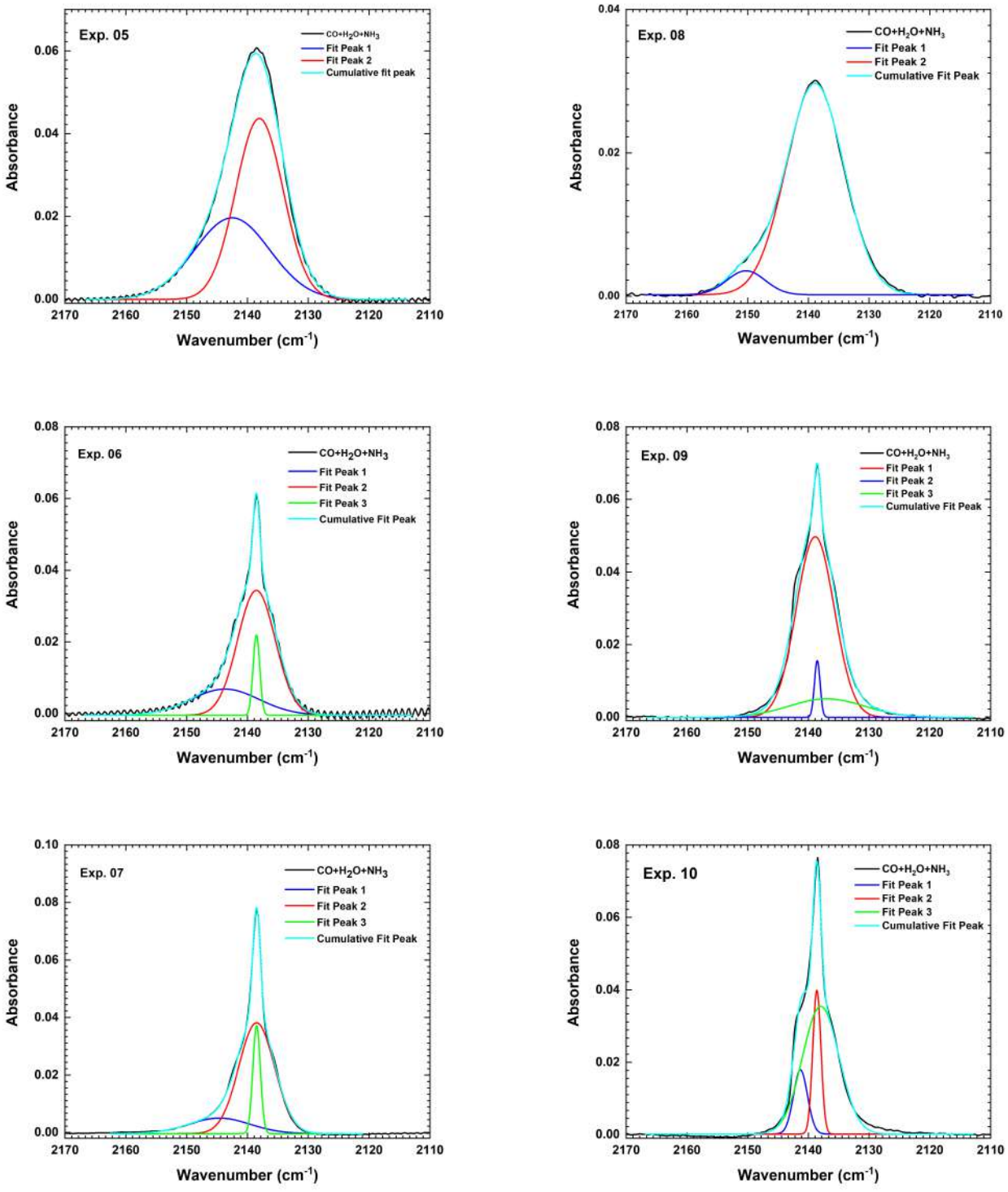

Figure A.2: Spectroscopic profiles of ternary ice mixtures CO, H_2O, and NH_3 across six experimental configurations. The left column illustrates the reference depositions on a bare ZnSe window, and the right column illustrates those on the meteorite powder substrate. The panels are organized by deposition protocol: the top row shows the mixed ices (mode 1), while the middle and bottom rows display the layered configurations (mode 2) with varying initial CO ratios.

Table A.2: Gaussian fitting of CO infrared profiles for the set of experiments described in Table A.1.

exp.	composition	first peak (cm^{-1})	IA (cm^{-1})	height	FWHM (cm^{-1})	second peak (cm^{-1})	IA (cm^{-1})	height	FWHM (cm^{-1})	third peak (cm^{-1})	IA (cm^{-1})	height	FWHM (cm^{-1})	R^2
without meteorite														
1	CO	2139.4	0.27	0.07	3.63	2139.3	0.12	0.05	2.21					0.9958
2	CO	2144.6	0.06	0.005	11.96	2138.5	0.28	0.03	6.93	2138.4	0.05	0.03	1.45	0.9917
5	CO, H_2O, NH_3	2142.5	0.30	0.019	14.62	2138.0	0.42	0.04	9.18					0.9997
6	CO, H_2O, NH_3	2143.6	0.10	0.006	13.28	2138.5	0.03	0.02	1.28	2138.5	0.27	0.03	7.29	0.9964
7	CO, H_2O, NH_3	2144.6	0.06	0.005	11.88	2138.4	0.05	0.03	1.45	2138.4	0.28	0.03	6.92	0.9994
meteorite														
3	CO	2141.1	0.04	0.01	2.51	2137.6	0.19	0.04	4.18					0.9942
4	CO	2141.1	0.04	0.02	1.65	2138.8	0.10	0.04	1.76	2136.9	0.10	0.01	4.97	0.9918
8	CO, H_2O, NH_3	2150.2	0.02	0.003	7.39	2138.9	0.35	0.02	11.27					0.9995
9	CO, H_2O, NH_3	2138.8	0.39	0.04	7.37	2138.5	0.01	0.01	1.09	2136.9	0.07	0.004	14.66	0.9967
10	CO, H_2O, NH_3	2141.3	0.05	0.01	2.74	2138.5	0.06	0.03	1.58	2137.9	0.26	0.03	7.10	0.9985

an asymmetric broadening characterized by a prominent shoulder at about 2142 cm^{-1}. This spectral feature is the direct signature of the meteorite's chemical and physical heterogeneity; the mineral grains and carbonaceous components offer a variety of high-energy adsorption sites that bind CO with varying strengths, shifting their vibrational frequencies and creating the distinct sub-peaks observed in the fit. The blue shift observed in the CO stretching frequency might thus be a diagnostic indicator of increasing tightness of the molecular environment, due to the topological roughness of the substrate powder. In vibrational spectroscopy, a shift toward higher wavenumbers occurs when the vibrational potential of the C≡O bond is steepened by external constraints. This is remarkably consistent with the confinement effect observed in astrophysical ice analogs, such as CO trapped in the water cages described by Zamirri et al. (2018). In such environments, the molecule is subjected to increased repulsive forces from its immediate surroundings, which effectively stiffens the bond and raises its vibrational frequency.

The influence of the deposition mode 1 (isothermal at 10 K) versus mode 2 (cooling the substrate during deposition), becomes the defining factor when the polar species H_2O and NH_3 are introduced. In experiment 8, which uses the isothermal mixed deposition mode on the meteorite, the profile is surprisingly smooth and the blue shoulder disappears entirely. This indicates a powerful chemical shielding effect facilitated by the stable thermal environment. At a constant 10 K, ammonia, which has a significantly higher affinity for active surface sites than CO, effectively primes the meteorite surface. As established by He et al. (2021), NH_3 outcompetes CO for high-energy binding sites. In this isothermal mixed mode, the NH_3 and H_2O molecules pacify the mineral surface, while the CO is trapped within the bulk of the H_2O:NH_3 hydrogen-bonded matrix. This chemical shielding effectively isolates the CO molecules from the underlying meteorite substrate, yielding the characteristically broad and symmetric Gaussian profile observed. Notably, the feature at ≈ 2150 cm^{-1} is absent in experiments $5-10$. Since this band is a known signature of CO interacting with dOH groups, its disappearance suggests that these surface sites are either occupied or structurally inaccessible under these conditions (see discussion in Section 3.3.

In the layered experiments on the meteorite (experiments 9 and 10), the blue-shifted shoulder unexpectedly reappears. We hypothesize that this behavior stems from a mechanism of topological inheritance. While deposition mode 2 involves active cooling and sequential layering, meaning the CO is chemically insulated from the meteorite by the H_2O:NH_3 buffer, it likely remains subject to the physical contours of the substrate. If the initial polar ice layer conforms to the irregular features of the meteorite rather than leveling them, the subsequent CO layer, lacking the thermal mobility to relax during active cooling, would be forced into high-strain coordination environments. This physical warping could effectively transmit the meteorite's roughness through the ice stack, recreating the tight vibrational environments that manifest as the blue-shifted shoulder.

The fact that we see a blue-shifted shoulder in the layered experiments 9 and 10 suggests that the meteoritic powder size is indeed much larger than the ice thickness. The ice layer is effectively a thin film draped over a rugged landscape. If the ice were thick enough to act as a leveling agent, the top surface would become smooth, and the C-O profile would revert to a standard bulk or mixed signature.

A.3 Conclusion and future perspectives

The preliminary experiments presented in this Appendix suggest that a mineral substrate may affect the spectroscopic response of the ice. We have identified two competing mechanisms that may govern the CO infrared profile. The first is chemical shielding, observed in isothermal mixed depositions, where polar species like ammonia outperforms CO for high-energy mineral sites, effectively priming the surface and resulting in symmetric profiles. The second is topological inheritance, where the rugged landscape of the meteorite is transmitted through the ice stack. In layered depositions, even when CO is chemically insulated from the mineral by a polar buffer, it remains physically warped by the underlying topography. This creates high-strain coordination environments that manifest as a characteristic blue-shifted shoulder, suggesting that the memory of the grain surface persists through several layers of ice.

For future investigations, we should explore the leveling threshold by systematically varying the ice thickness relative to the grain size (that is predetermined). Determining at what point the ice mantle becomes thick enough to act as its own smoothing agent would provide a diagnostic for interpreting the grain-ice relationship in different astrophysical environments.

Furthermore, while the H chondrite provides a high-iron, heterogeneous surface, repeating these protocols with amorphous silicates or carbonaceous materials would help differentiate between purely topographic effects and those driven by specific mineral chemistry. Finally, performing temperature-programmed studies could reveal whether chemical interactions could modify the desorption temperature.

4. The chemical architecture of ultraviolet-processed ice mantles

The scientific investigation into the formation and chemical evolution of interstellar ice mantles is a cornerstone of modern astrochemistry, as these solid structures serve as the primary reservoirs of volatile elements and the precursors to molecular complexity in the cosmos. This chapter describes the extension of a research line previously focused on the accretion dynamics and molecular segregation of a ternary mixture of water, ammonia, and carbon monoxide performed by Jiménez-Escobar et al. (2024). While the initial phase of the study established that ice mantle growth under slow cooling conditions leads to an intrinsically non-uniform and layered composition, the introduction of ultraviolet irradiation via a MDHL (see Section 2.3.1) opens a new analytical dimension. This transition from a purely thermodynamic regime to an energetic one is essential to simulate the environment of dense molecular cloud cores, where cosmic-ray-induced secondary ultraviolet radiation drives the synthesis of COMs and the non-thermal desorption of chemical species into the surrounding gas.

4.1 Non-uniform growth and the energetic processing

The methodological approach adopted in this study is central to the interpretation of the mantle's chemical and physical evolution, as the choice of experimental protocol is not merely a technical detail but a fundamental factor in determining the nature and astrophysical relevance of the resulting ice mantles. Much of the existing literature relies on a standard procedure involving ice deposition at extremely low temperatures, typically around 10 K, followed by a distinct phase of energetic processing. While this sequential method is useful for isolating individual processes, it deviates significantly from the dynamics of interstellar environments, where accretion, cooling, and exposure to ultraviolet radiation occur concurrently. Another alternative is isothermal deposition under simultaneous irradiation; however, this still fails to capture the thermal evolution inherent in the early stages of molecular cloud development. In this work, we utilize a procedure that more faithfully simulates space conditions by cooling the substrate while the gas mixture is deposited and simultaneously subjected to photolysis.

The simultaneous cooling, deposition, and irradiation protocol introduces a layer of chemical complexity that alters reaction efficiencies compared to static models. In a pre-formed ice, the diffusion of radicals produced by irradiation is severely restricted by the rigid solid matrix. Conversely, during simultaneous deposition, reactive species possess a degree of intrinsic mobility on the surface before being buried by subsequent layers. This scenario fosters a more dynamic surface chemistry where certain radical reactions might become more efficient, possibly leading to the synthesis of complex organic molecules, that otherwise can be damped or never occur in a traditional sequential deposition system. The final chemical architecture of the mantle is thus dictated by the competition between the timescales of thermal diffusion and those of photolysis.

Furthermore, the growth of the ice cannot be viewed anymore as a simple process of accumulation; it must be understood as a dynamic equilibrium between the injection of new material and mass loss driven by ultraviolet-induced photodesorption. This phenomenon is particularly critical for volatile species such as CO. In our experimental setup, the ultraviolet radiation continuously acts upon the forming surface, effectively acting as a brake on the growth of the mantle. A tight competition arises between accretion and photodesorption. While accretion must ultimately prevail, otherwise, we would observe no mantles at all, photodesorption actively shapes the thickness and stoichiometry of the ice, potentially limiting CO saturation and favoring the enrichment of less volatile species. Characterizing this balance is essential for accurately interpreting the stratification of interstellar ices and for evaluating how ultraviolet radiation influences the construction of icy mantles from their very earliest stages. Ultimately, this simultaneous irradiation induces significant chemical and structural modifications, redefining the construction of the ice mantle from its very inception.

Jiménez-Escobar et al. (2024) conducted a preliminary experiment in which they modified the mode 1 deposition protocol (as detailed in Section 2.4) into mode 2, specifically, a procedure involving simultaneous cooling and deposition without irradiation. This modification was designed to isolate the effects of the thermal gradient from those of energetic processing, providing a baseline for comparing how the ice structure evolves when the ultraviolet field is absent during the accretion phase. These authors replicated in the laboratory what has been inferred observationally over the last two decades (e.g., Pontoppidan et al. 2003), namely ice mantles are not homogeneous mixtures but stratified structures whose architecture is determined by the binding energy differences of their components. During the cooling of a substrate from

Table 4.1: Fit parameters for the accretion of the ternary ice mixture.

Molecule	E_b (K)	T_s (K)	α	γ (T_s/E_b)	Note
H_2O	4400 – 5165	136.0	15.0	0.031 – 0.026	first layer
NH_3	3070	106.5	6.4	0.035	polar phase
CO	890 – 980	29.5	4.5	0.030 – 0.033	apolar phase

200 K to 10 K in the presence of a gaseous H_2O:NH_3:CO mixture, water is the first species to condense (around 140 K), followed by ammonia (110 K), and finally carbon monoxide (below 40 K). Such physical segregation implies that molecules are not uniformly distributed, creating distinct chemical zones: an inner polar layer rich in water and ammonia and an outer apolar layer dominated by CO.

Because the condensation of a gas onto a surface is an inherently stochastic process, molecules do not all freeze out at a single, exact temperature. Instead, the transition from the gas phase to the solid phase occurs over a specific temperature range. Defining $\mathcal{Q}$ the normalized QMS signal, we identify the net deposition rate with $D(T) = 1 - \mathcal{Q}(T)$, and we represent it through the sigmoid function

$$D(T) = \frac{1}{2}\left[1 - \mathrm{erf}\left(\frac{T - T_s}{\sqrt{2\alpha^2}}\right)\right] \tag{4.1}$$

where T is the temperature, and T_s and α two fitting parameters, associated with the deposition temperature (and approximately the desorption temperature) and its variance. Fit results, obtained by Jiménez-Escobar et al. (2024), provide the critical parameters for interpreting the impact of ultraviolet radiation. The binding energies E_b and desorption temperatures T_s, measured for the ternary mixture components and reported in Table 4.1, indicate the thermal stability of each layer prior to energetic intervention. The deposition temperature $T_s \approx 30$ K inferred for CO is significantly lower than that derived by He et al. (2016). However, one must consider the fact that the values obtained in our experiments are not real sticking coefficients, as instead they are net deposition rates. In any case, this hierarchical stability ensures that the innermost layers of a grain mantle are dominated by the most refractory volatiles (water and ammonia), while the more volatile species like CO form an outer coating. Such a stratified composition is significantly more realistic than a mixed ice for the conditions typically found in interstellar molecular clouds.

Expanding this protocol to include ultraviolet irradiation is motivated by the necessity of understanding how such dynamic stratification governs chemical reactivity. In a naturally accreting system, ultraviolet photons do not interact with a simple statistical mixture; rather, they penetrate layers of varying physical and chemical properties, triggering photolysis and radical recombination processes that are strictly dictated by the local matrix environment. By employing a MDHL, we simulate the secondary ultraviolet radiation field characteristic of dense molecular cloud interiors, where the flux typically ranges between $10^3 - 10^4$ photons cm^{-2} s^{-1} (Cecchi-Pestellini and Aiello, 1992). This allows us to observe, in real-time, how the evolving architecture of the ice mediates the complex chemistry of the interstellar medium.

4.2 Experiments

The ice experiments were conducted using LIFE, the technical specifications of which are detailed in the experimental section in Chapter 2. To ensure comparability and provide a robust benchmark for our findings, we adopted boundary conditions and deposition protocols similar to those utilized by Jiménez-Escobar et al. (2024). This allows us to evaluate the structural evolution of ice mantles and the efficiency of chemical pathways under ultraviolet irradiation within a consistent experimental framework. Two deposition configurations were employed using a ternary gas mixture of H_2O:NH_3:CO in a ratio of 2:1:6. These configurations involved two constant inlet flux values corresponding to initial deposition pressures at 200 K of 1.5×10^{-7} and 6.6×10^{-8} mbar. After cooling the cryostat to 200 K, a 30-minute thermalization period was observed for the CaF_2 window. the gas mixture, prepared via a premixing chamber, was then introduced. Once the selected deposition pressure was reached, we initiated a dynamic process designed to simulate interstellar conditions more accurately than traditional sequential methods: the substrate was cooled to 10 K at a rate of 2 K min^{-1} while simultaneously undergoing ultraviolet irradiation via MDHL. High-purity reagents were used: GC-mass grade

Table 4.2: Wavenumber peak positions of the major vibrational bands of the ternary H_2O:NH_3:CO (2:1:6) ice mixture at 10 K.

wavenumber (cm^{-1})	assignment
1116	NH_3
1360	?
1389	$HCONH_2$
1485	NH_4^+
1504	H_2CO
1590	$HCOO^-$
1635	H_2O
1690	$HCONH_2$
1710	H_2CO
1845	?
2138	CO
2160	OCN^-
2244	HNCO
2342	CO_2

H_2O (Merck), purified via at least three freeze-pump-thaw degassing cycles, and CO and NH_3 (Matheson, 99.99% purity). Upon reaching the base temperature of 10 K, the irradiated samples were subjected to TPD by heating the substrate to room temperature in a controlled manner. The evolution of the ice was monitored in situ via FTIR transmittance spectroscopy, while the desorbing species were analyzed using a QMS.

The column density of the deposited species was determined using the standard integrated absorbance relationship (2.1). The band strengths adopted for the analysis are $A_{CO} = 1.1 \times 10^{-17}$ cm molecule^{-1} at 2136 cm^{-1} (Jiang et al., 1975), $A_{NH_3} = 1.7 \times 10^{-17}$ cm molecule^{-1} at 1070 cm^{-1} (d'Hendecourt & Allamandola, 1986), and $A_{H_2O} = 9.0 \times 10^{-18}$ cm molecule^{-1} at 1659 cm^{-1} (Bouilloud et al., 2015). Due to the spectral overlap between the H_2O bending mode near 1660 cm^{-1} and the NH_3 band at approximately 1625 cm^{-1}, the water column density was corrected by subtracting the ammonia contribution, which was determined by scaling the integrated absorbance of the independent NH_3 band at 1070 cm^{-1}.

4.3 Results

The energetic processing of ice mixtures composed of H_2O, NH_3, and CO via ultraviolet irradiation has been extensively reported in the literature (Öberg, 2016). The chemistry generated by the ultraviolet irradiation in this mixture at 10 K depends on the competitive dissociation of the parent molecules and the subsequent recombination of highly reactive radicals trapped in the solid matrix. Because water H_2O is the dominant component, its photolysis dictates the primary radical pool. The absorption of ultraviolet photons splits water into hydroxyl radicals and atomic hydrogen. The highly reactive OH radicals rapidly oxidize adjacent carbon monoxide molecules. This reaction sequence proceeds through a transient formyl radical intermediate HOCO and acts as the principal low-temperature pathway for the efficient synthesis of CO_2 (Hudson & Moore, 2001). Concurrently, the competitive photodissociation of ammonia yields amidogen radicals NH_2 and imidogen biradicals NH, alongside additional atomic hydrogen. The true chemical complexity of this ternary system emerges when these nitrogen-bearing fragments cross-react with the carbon-bearing species. The recombination of amidogen with formyl radicals HCO, the latter formed via direct hydrogen addition to CO, drives the synthesis of formamide $HCONH_2$, a crucial prebiotic building block. Further radical-radical and radical-molecule additions generate related complex species such as formaldehyde H_2CO, formic acid HCOOH, and urea H_2NCONH_2. The signature reaction of this specific mixture is the formation of the cyanate ion OCN^-. In the solid phase, the highly acidic radical networks and transiently formed isocyanic acid structures undergo a spontaneous, barrierless proton transfer to the surrounding basic ammonia matrix. This acid-base neutralization occurs efficiently even at 10 K, trapping the product as an ammonium cyanate $NH_4^+OCN^-$ ionic salt framework embedded within the bulk water ice structure.

This complex network of radical-recombination and acid-base reactions may be fundamen-

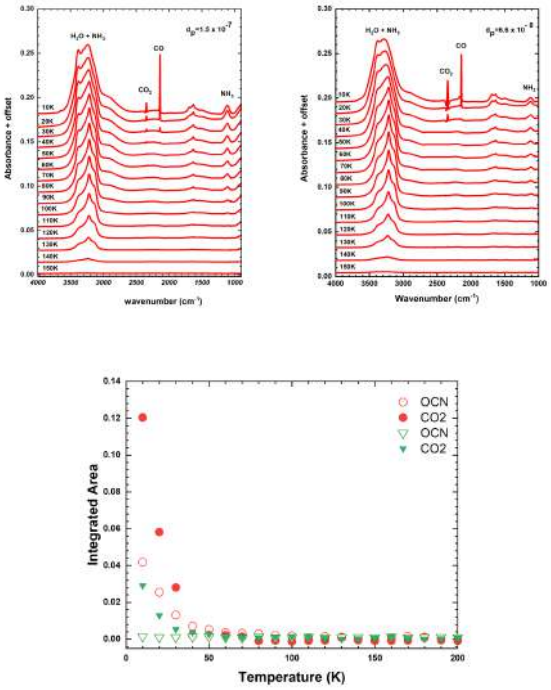

Figure 4.1: Infrared spectroscopic evolution of the ternary H_2O:NH_3:CO (2:1:6) ice mixture during concurrent molecular deposition, cryogenic cooling, and ultraviolet irradiation. The bottom panel displays the calculated integrated band areas for the two primary photoproducts, CO_2 (circles) and OCN^- triangles), following their accretion on the cooling window, under high (filled) and low (empty) deposition pressure regimes.

tally altered by employing a dynamic protocol that combines simultaneous molecular condensation, continuous cooling from 200 K down to 10 K, and concurrent ultraviolet irradiation. Under these dynamic conditions, the initial photochemistry is heavily surface-dominated. As the gaseous mixture condenses, the arriving molecules are immediately exposed to the ultraviolet photon flux at the vacuum-ice interface rather than within a rigid, pre-formed bulk matrix. This immediate exposure enhances the primary photodissociation of water into reactive hydroxyl radicals OH and atomic hydrogen, which rapidly oxidize the (initially transient) surface carbon monoxide to synthesize carbon dioxide or interact with ammonia photo-fragments to build complex organic architectures. Because the ice is actively growing under continuous deposition, it develops a noticeably porous macroscopic structure. This dynamic physical environment significantly extends the exposure time of individual molecules to the incoming ultraviolet radiation before they are buried, drastically boosting the overall efficiency of localized radical recombination. Furthermore, as new layers of the ternary mixture continually accrete over the irradiated surface, newly formed reactive intermediates and volatile photoproducts, such as the ammonium cyanate ion pairs generated from spontaneous low-temperature acid-base neutralizations, are immediately trapped and locked deep within the growing water-dominated matrix. This rapid, continuous burial protects these newly synthesized species from prolonged ultraviolet destruction and isolates them safely until subsequent thermal desorption. The resulting chemistry depends on the balance between the accretion rate and ultraviolet penetration (which in turn depends on the current composition of the ice, Cruz-Diaz et al. 2014a,b). Finally, because the substrate temperature drops steadily from 200 to a 10 K baseline throughout the deposition process, the growing ice mantle experiences deep thermal stratification. The foundational layers accreted at higher temperatures possess entirely different thermal mobility, radical diffusion rates, and sticking coefficients compared to the uppermost layers frozen rigidly at 10 K, meaning the resulting chemical complexity of the ice is deeply intertwined with the shifting physical and thermal state of the matrix at the exact moment of its structural formation.

The extensive, simultaneous alteration of the chemical network in the growing ice at 10 K is detailed progressively across Figure 4.1 and Figure 4.2, with all corresponding vibrational

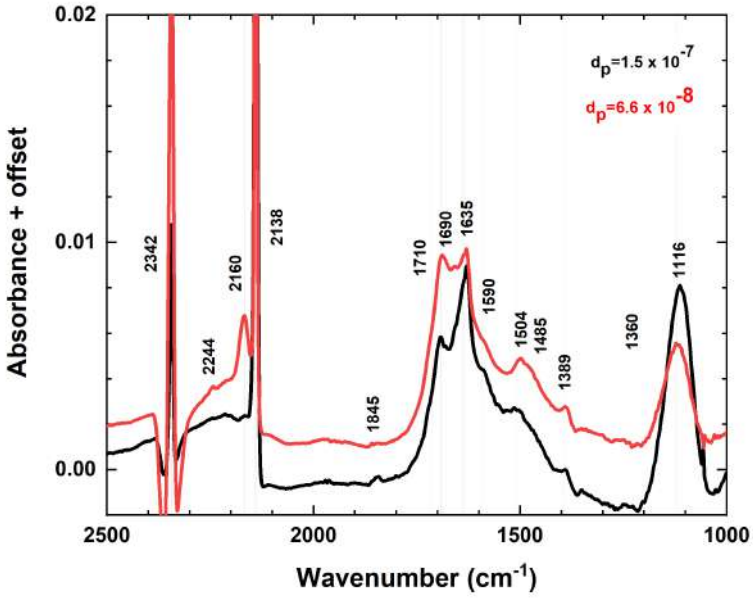

Figure 4.2: FTIR spectra of the ternary H_2O:NH_3:CO (2:1:6) ice mixture recorded at 10 K following concurrent cooling, molecular deposition, and ultraviolet irradiation, for two deposition pressure values.

frequencies listed in Table 4.2. The parent species are readily identified by their characteristic vibrational modes, including the strong carbon monoxide stretch centered at 2138 cm^{-1} and the ammonia umbrella mode peaking at 1116 cm^{-1}. The growth of new chemical species is monitored by a highly prominent absorption band at 2342 cm^{-1} (CO_2). Another indicator of successful ultraviolet synthesis is the feature appearing at 2160 cm^{-1}, identifying the OCN^- ion, the endpoint of low-temperature processing in ammonia- and carbon monoxide-bearing matrices, accumulating steadily even if its transient precursor states, such as HNCO, remain undetectable. Looking further down the spectrum, a complex arrangement of absorption features emerges within the $1700 - 1500$ cm^{-1} region. This specific envelope indicates the efficient low-temperature synthesis of diverse carbonyl-bearing networks, such as formaldehyde at 1504 and 1710 cm^{-1} alongside formic acid, while concentrations of ammonium ions appear near 1485 cm^{-1}, tracking acid-base proton transfers within the ice matrix. It should be noted that the sharp, variable feature occasionally observed around 2350 cm^{-1} is an experimental artifact stemming from external atmospheric CO contamination rather than an intrinsic product of the ice chemistry.

To complement the solid-state structural tracking, QMS gas-phase analysis conducted during the warm-up sequence provides a detailed look at the thermal desorption dynamics, as shown in the mass tracks of Figure 4.3. While the solid-state signature of HNCO remained completely obscured in the initial 10 K infrared spectra, its volatile sublimation is clearly confirmed in the gas phase by the appearance of the molecular ion at $m/z = 43$, with its characteristic fragmentation partners NCO ($m/z = 42$) and HCO ($m/z = 29$). The distinct desorption peaks recorded below 200 K represent classic co-desorption phenomena, where volatile photoproducts are physically swept out into the gas phase alongside the primary sublimation fluxes of escaping NH_3 and H_2O. Particular analytical value is found in the high-temperature window immediately following the bulk water sublimation. In this zone, the low-temperature $NH_4{}^+OCN^-$ salt synthesized via early acid-base interactions undergoes thermal decomposition, desorbing cleanly as volatile NH_3, HNCO, and HOCN. Finally, evaluating the broader fragmentation patterns highlights the deep molecular diversity achieved within the processed ice. The high relative signal intensities observed at $m/z = 29$ point to major sublimation contributions from complex backbones like formamide $HCONH_2$ or urea H_2NCONH_2, which readily synthesize in heavily irradiated mixtures. Together, these coupled spectroscopic data demonstrate that complex nitrogen- and carbon-bearing species form with high efficiency under interstellar conditions and

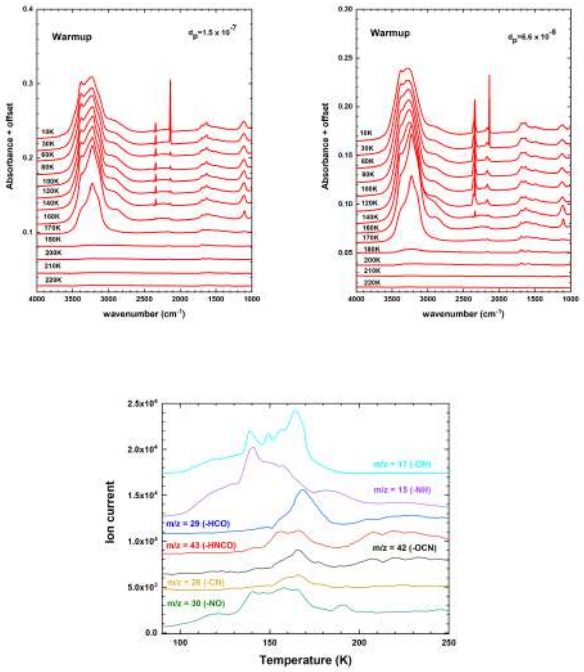

Figure 4.3: Thermal desorption profiles of the ternary H_2O:NH_3:CO (2:1:6) ice mixture. The top panels show the structural evolution of the FTIR transmission spectra as a function of the increasing temperature, while the bottom panels display the QMS tracks (m/z) corresponding to characteristic molecular fragments of parent species and synthesized photoproducts escaping into the gas phase.

remain securely stored within volatile ice reservoirs until released during warming-up. Tracking the subsequent thermal evolution of these irradiated samples via FTIR spectroscopy reveals a complex structural transition as a function of temperature, as illustrated in the QMS profiles of Figure 4.3. In the low-temperature regime extending from 10 to 80 K, the spectra are heavily dominated by the broad, massive absorption features spanning the $3200 - 3500$ cm^{-1} range, which represent the deeply integrated O$-$H and N$-$H stretching modes of the host water and ammonia matrix. As thermal energy is slowly introduced, these structural bands undergo major profile shifts and a steady reduction in intensity, signaling a progressive, microscopic restructuring of the extensive hydrogen-bonded network alongside the initial onset of molecular desorption. In the mid-infrared region ($2200-2000$ cm^{-1}), the key photoproduct feature OCN^- persist up to temperatures of $160 - 170$ K. This long-term survival indicates that these volatile species are effectively trapped, locked deep within the rigid cages of the water-dominated matrix. Once the temperature breaks past the 170 K threshold, a global sublimation of the water ice bulk drives a near-complete desorption of all trapped components by $200 - 220$ K.

4.4 Impact of ultraviolet irradiation on ice mantle stratification

A central problem in astrochemistry is understanding how the internal physical structure and chemical distribution of an ice mantle change while it is actively growing on a dust grain. Traditionally, laboratory simulations have investigated interstellar ice chemistry by depositing a bulk, uniform mixture of gases at a low base temperature (typically 10 K) and subsequently exposing it to ultraviolet photons or thermal warming. While this static method helps identify potential photoproducts, it fails to capture the true, dynamic environment of a dense molecular cloud. In interstellar space, ice mantles grow gradually over millions of years as molecules from the gas phase continuously collide with and freeze out onto dust grain surfaces. Crucially, this accretion occurs while the environment is simultaneously subject to continuous vacuum ultraviolet photoprocessing and cosmic-ray bombardment. This means that an ice mantle is never a static, pre-blended bulk structure; instead, it is an evolving physical network where surface layers are continuously processed before being buried by subsequent freeze-out material.

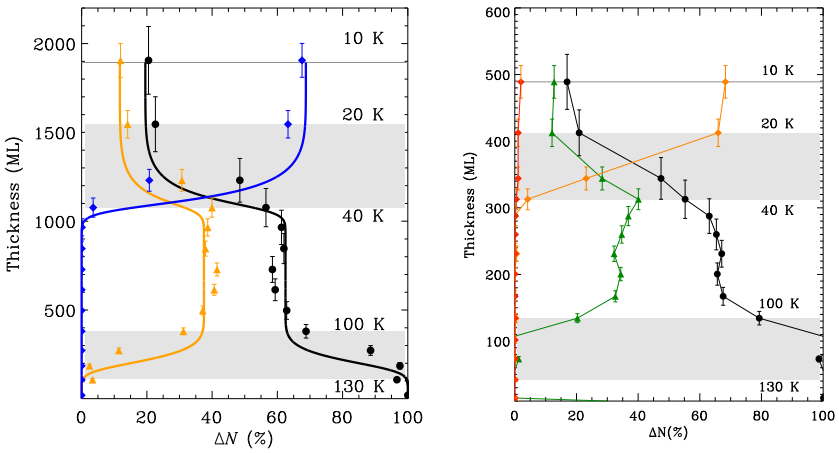

Figure 4.4: Comparative fractional abundance profiles versus ice thickness for parental species under non-irradiated (left panel) and irradiated (right panel) conditions. Solid lines on the non-irradiated data represent the analytical model developed by Jiménez-Escobar et al. (2024).

Disentangling how much of an ice mantle's internal stratification is driven by pure thermal accretion versus active, ongoing photon-driven conversion remains a major challenge when attempting to interpret astronomical observations. To establish a clear baseline and isolate one half of this problem, Jiménez-Escobar et al. (2024) developed a detailed physical model focused on mapping the pristine, non-uniform growth of interstellar ice mantles in the absence of an energetic radiation field. The goal of their study was to trace how a multi-component interstellar gas mixture naturally stratifies itself based on individual molecular properties when accreting under a dynamic temperature gradient.

In space, as a dense core collapses, dust grains slowly transition from warmer diffuse environments down to dense, shielded cryogenic zones. The deposition model exploited in Jiménez-Escobar et al. (2024) (and in this study) replicates this transition by mapping freeze-out while the substrate temperature continuously drops from 200 K down to a dense-core base temperature of 10 K. Through this detailed modeling protocol, these authors showed that the resulting interstellar ice mantle naturally organizes into a highly segregated, stratified architecture governed entirely by the sublimation temperatures and non-linear sticking coefficients of the parent species. Because different volatile species condense at entirely different temperatures, the freeze-out does not happen all at once; rather, the molecules freeze out sequentially as the environment cools. At higher temperatures, spanning roughly from 140 K down to 110 K, water molecules hitting the dust grain surface overcome thermal desorption first due to their high binding energy, achieving a sticking coefficient near unity and freezing out exclusively to lay down a highly pristine, uniform polar foundation that dominates the first several hundred monolayers of the ice's spatial profile. As the cooling continues its steady descent into the 110 K to 40 K regime, the thermal energy of the environment drops below the sublimation threshold of ammonia, causing its sticking coefficient to rise from zero. Within this intermediate zone, NH_3 begins to co-deposit efficiently alongside the ongoing water flux, and because this region forms across a dynamic thermal gradient, the fractional composition of ammonia changes progressively as a function of depth, transforming the pure water base into an intimately mixed, binary mixture. Even during this phase, carbon monoxide remains entirely in the gas phase, leaving the first 1000 to 1500 monolayers of the evolving ice profile completely devoid of carbon-bearing parent material. The final architectural transition occurs when the system drops below the 40 K threshold and approaches the 10 K baseline of a fully formed dense core. At these deep cryogenic temperatures, CO increases rapidly its sticking coefficient. Because the local abundance of CO in the surrounding gas is heavily dominant (replicating what actually occurs in space), it rapidly overwhelms the tail-end of the water and ammonia deposition, producing a stark structural inversion in the outermost layers of the ice mantle and capping the entire 2000 monolayer structure with a highly concentrated, non-polar, and nearly pristine CO-rich outer envelope. Because there are no ultraviolet photons or cosmic rays in this baseline model to cleave chemical bonds, inject radical fragments, or trigger non-thermal surface diffusion, the

molecules remain structurally locked exactly where they fell, providing a resulting profile that acts as a pristine physical archive of the dust grain's cooling history, showing a clear, unadulterated spatial separation from a purely polar, water-rich base to a completely non-polar, carbon monoxide-dominated crust.

To provide a benchmark for this dynamically processed environment, the distribution profiles of the remaining parental species obtained in the present study can be directly compared with the non-irradiated baseline model of Jiménez-Escobar et al. (2024), specifically evaluating the fractional ice compositions as a function of depth between the two systems. Without ultraviolet radiation, parent molecules accumulate continuously to yield a heavily stratified, segregated mantle where the parental layer equivalents reach a maximum tracking thickness of approximately 2000 ML. In sharp contrast, when concurrent ultraviolet irradiation is introduced here during the cooling and accretion sequence, the distribution curves of these same parent molecules are heavily compressed, reaching a maximum tracking thickness of only about 600 ML (Figure 4.4). It is important to note that this specific comparison strictly tracks the survival and spatial distribution of the primary parental precursors rather than representing the absolute physical thickness of the processed cryogenic film. In principle, the true physical thickness of the irradiated mantle must account for the volumetric contribution of the newly synthesized photoproducts, while photodesorbed species are removed from the ice, thereby enriching the gas phase. Applying the analytical model developed for the non-irradiated case to the ultraviolet irradiated experiment presents several difficulties. In the purely thermal scenario, the analytical model relies on a relatively straightforward balance between the incoming gas flux, temperature-dependent sticking coefficients, and thermal desorption rates. Introducing energetic irradiation disrupts this balance by triggering highly non-linear phenomena. First, radiation induces non-thermal photodesorption, physically ejecting newly deposited molecules back into the gas phase and fundamentally altering the effective rate of accumulation. Second, the incoming photons drive instantaneous photodissociation and radical recombination, meaning the mathematical framework would need to evolve from a simple physical deposition equation into a deeply coupled network of differential equations describing real-time chemical destruction and formation. Additionally, this active photochemistry generates a volume of new photoproducts that occupy physical space within the lattice, as evidenced by the red line in the right panel representing the chemical evolution of CO_2 during the manrle growth. Because carbon dioxide is one of the major products, the contribution of photo-products to the total thickness of the mantle is not particularly relevant.

5. Phosphorus activation on icy moons

5.1 The geochemical landscape of Enceladus and the Cassini discovery

The Cassini-Huygens mission, a joint endeavor by NASA and ESA that orbited Saturn from 2004 to 2017, utilized the moon Enceladus as a natural laboratory for probing the composition of an alien ocean. The spacecraft's trajectory through the south polar plumes and the E-ring, a diffuse structure primarily fed by Enceladean eruptions, allowed for the direct sampling of frozen ocean droplets. One of the most significant breakthrough in recent years, it is the study by Postberg et al. (2023), involving the identification of high concentrations of dissolved phosphorus in the form of sodium orthophosphates. The detection of phosphorus was not an immediate result of the mission's initial data processing but required a sophisticated re-analysis of the Cosmic Dust Analyzer (CDA) mass spectra collected during multiple flybys. The CDA was designed to measure the mass, velocity, and chemical composition of individual ice grains striking its target at high velocities. The resulting impact-ionization mass spectra revealed a subset of grains rich in salt, which provided a representative sample of the subsurface ocean's major solutes. Laboratory analogue experiments were essential to interpreting these spectra. Researchers utilized specialized setups to mimic the high-velocity impact of ice grains into the CDA detector, testing various chemical solutions to find a match for the space-borne data. The results demonstrated that only solutions containing sodium phosphates, specifically Na_3PO_4 and Na_2HPO_4, could reproduce the specific peaks observed in the Cassini data.

Prior to this discovery, geochemical models were largely divided on the availability of phosphorus within Enceladus. Traditional terrestrial-centric models suggested that phosphorus might be severely limited by the precipitation of calcium phosphates, such as hydroxyapatite $Ca_5(PO_4)_3OH$, which have extremely low solubilities in neutral to alkaline waters. These earlier studies hypothesized that phosphate would be sequestered in the seafloor minerals, leaving the ocean column depleted of this essential nutrient (Lingam & Loeb, 2018). However, the empirical evidence from Cassini confirms that the Enceladean ocean is a soda ocean, characterized by high concentrations of dissolved carbonates, $NaHCO_3$ and Na_2CO_3, and an alkaline pH. This chemistry is a primary driver for the high solubility of phosphorus. In the presence of high carbonate activity, calcium ions are preferentially sequestered as stable calcium carbonates $CaCO_3$, such as calcite. This removal of calcium prevents the formation of insoluble calcium phosphates, allowing phosphorus to accumulate in the aqueous phase as water-soluble sodium phosphates. The inferred phosphate concentration, reaching millimolar levels, is at least 100 times higher than that of terrestrial oceans and potentially 1,000 times higher in certain plume-forming regions. This abundance suggests that phosphorus is not a limiting factor for putative life on Enceladus, satisfying one of the strictest requirements for habitability (Cockell et al., 2016).

Table 5.1 summarizes the chemical composition of the subsurface ocean as inferred from the laboratory reproduction of CDA mass spectra of salt-rich ice grains. In the elemental and ionic inventory table, the ocean components are listed as individual ions rather than neutral salts (e.g., Na^+ instead of NaCl) to accurately reflect both the geochemical state of the Enceladean interior and the measurement technique used by the Cassini spacecraft. In the liquid environment of the subsurface ocean, salts exist in a state of complete dissociation, where they are separated into their constituent cations and anions. Sodium (Na^+) is classified as the major cation because it serves as the dominant balancing charge for a diverse pool of negative ions discovered in the plumes, including chloride (Cl^-), bicarbonate (HCO_3^-), carbonate (CO_3^{2-}), and the recently identified sodium phosphates (Na_3PO_4). Because the Enceladean soda ocean is defined by this collective ionic activity, referring to a single substance like NaCl would be geochemically incomplete, as Na^+ ions are associated with multiple anionic partners simultaneously in the aqueous phase. Furthermore, this ionic representation matches the direct detection method employed by Cassini's CDA. During plume fly-throughs, ice grains struck the instrument at velocities of approximately 10 km/s, causing them to instantly vaporize and ionize. The CDA then measured the mass-to-charge ratio of the resulting individual ions, providing a direct fingerprint of the ocean's ionic composition rather than detecting intact salt molecules. Finally, while organic molecules are extremely dilute in the global bulk ocean, they get highly concentrated in certain ice grains through a natural sweeping process. As gas bubbles rise through miles of ocean water, they act as chemical scavengers, stripping water-repelling organic compounds and carrying them to the surface. This creates a concentrated, oil-like organic film floating on top of the water surface inside the geyser vents. When these bubbles pop,

Table 5.1: Estimated composition of the bulk oceanic chemical environment in molarity (M).

element/ion	detected species	estimated concentration	notes
Sodium (Na^+)	major cation	0.05–0.2	dominant salt-forming cation
Potassium (K^+)	minor cation	$\sim 3.3 \times 10^{-3}$	100–200× less abundant than Na
Chloride (Cl^-)	major anion	0.05–0.2	key indicator of oceanic salinity
Carbonate ($CO_3{}^{2-}$)	$HCO_3{}^-$, $CO_3{}^{2-}$	0.02–0.1	maintains alkaline soda ocean pH
Phosphorus (P)	Na_3PO_4, Na_2HPO_4	10^{-3}–10^{-2}	100–1,000× terrestrial ocean levels
organics	dissolved organic carbon	10^{-6}–10^{-4}	micromolar bulk concentration(1)

(1) enriched up to 10^{-2} in specific plume grains (Postberg et al., 2023), see text.

they spray out droplets of this concentrated organic film, which freeze into specific ice grains that contain hundreds to thousands of times more organic material than the surrounding ocean water (Porco et al., 2017).

While the subsurface ocean provides the thermal and chemical stability necessary for prebiological chemistry, the surface of Enceladus serves as a high-energy reactor where these oceanic ingredients are processed by space radiation (Li et al., 2022). Approximately 90% of the material ejected in the plumes falls back onto the moon's surface, accumulating in thick deposits near the south pole. The surface of Enceladus is characterized by UHV conditions and extreme cold. Daytime high temperatures rarely exceed 100 K, while nighttime temperatures can drop significantly lower, preserving the chemical state of deposited species for geological timescales. Laboratory simulations of these conditions require chambers capable of reaching base pressures up to 10^{-10} mbar and cooling stages that can maintain temperatures between 10 K and 100 K. Under these conditions, water ice exists primarily in an amorphous or weakly crystalline state. ASW is particularly significant because its disordered structure and high porosity allow for the trapping of volatile gases and the efficient diffusion of radiation-induced radicals.

5.2 The magnetospheric radiation environment

Saturn possesses a massive and highly axisymmetric magnetic dipole with an equatorial field strength of approximately 21 μT (0.21 G). The magnetic dipole is strictly aligned with the planet's rotational axis, with an inclination of less than 0.5°. However, it is slightly shifted northward along the spin axis by approximately 0.037 R_S to 0.04 R_S (where R_S is the Saturn radius, measuring approximately 60,330 km). This planetary magnetic bubble traps solar wind and internally sourced plasma, creating a complex and dynamic radiation environment that continuously bombards the planet's inner icy satellites (Belenkaya et al., 2006).

The magnetosphere is generally divided into several distinct regions. The innermost region, located inside 3 R_S, is co-spatial with the main planetary rings. This zone features a strictly dipolar magnetic field but is heavily depleted of thermal plasma, which is efficiently absorbed by ring particles. The second region, extending from approximately 3 to 6 R_S, is the inner magnetosphere. It contains the cold plasma torus, which is the densest plasma region in the Saturnian system. The bulk of this plasma consists of water-group ions (O^+, H_2O^+, OH^+, H_3O^+, $HO_2{}^+$, and $O_2{}^+$) along with lighter protons and minor amounts of ionic nitrogen N^+. This toroidal plasma is continuously replenished by the massive cryovolcanic plumes fountaining from the south pole of Enceladus. Without entering into the detailed plasma physics of Saturn's magnetosphere, the essential point is that the material supplied by Enceladus is initially cold and largely neutral, consisting mainly of water vapor and icy grains emitted by the south polar plumes; once this material becomes ionized inside the rapidly rotating magnetic environment of Saturn, it is forced into corotation with the magnetic field and is therefore accelerated, producing the so-called pickup ions. Additional processes such as inward radial transport, wave–particle interactions, and magnetic reconnection further energize part of the plasma population, generating the trapped energetic particles responsible for the irradiation of the inner icy satellites. In this way, Enceladus simultaneously acts as a major source of magnetospheric plasma and as a body immersed in, and continuously exposed to, the energetic particle environment that the Saturnian magnetosphere itself creates from that material. A schematic representation of the main plasma populations and transport processes operating in the inner Saturnian magnetosphere together with the orbits of the inner moons is shown in Fig. 5.1.

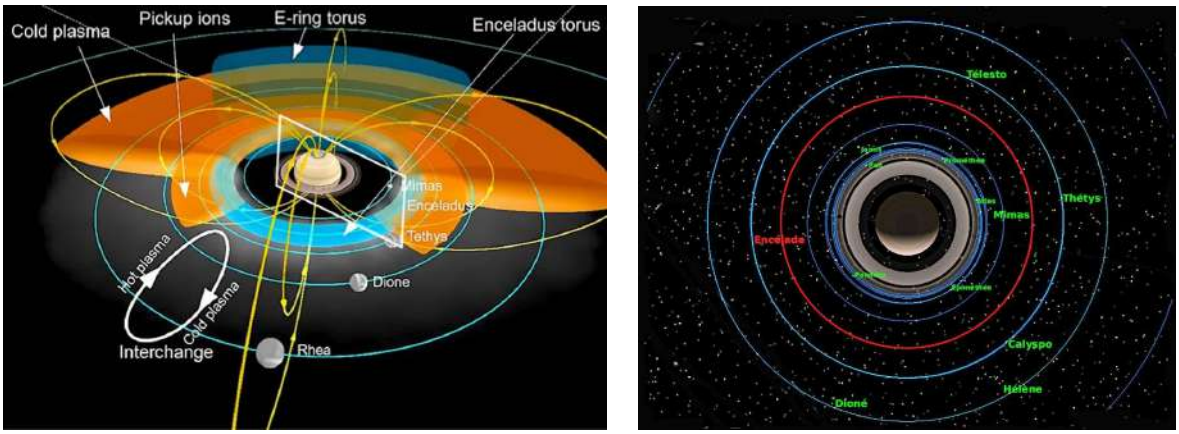

Figure 5.1: Schematic view of the inner magnetosphere of Saturn, illustrating the cold plasma (gas) torus associated with Enceladus, the pickup ion population generated from plume material, the E-ring torus (the doughnut-shaped outermost dust ring of Saturn created directly by Enceladus), and the interchange transport processes responsible for plasma redistribution and energization within the Saturnian system (left panel). The orbits of the major Saturn's moons are displayed in the right panel.

5.2.1 Mimas and Tethys

The bombardment of Saturn's inner moons by high-energy particles trapped in the radiation belts is not uniform. It is highly asymmetric and produces dramatic physical and thermal alterations on their surfaces, most famously observed as "Pac-Man" anomalies on Mimas and Tethys. While low-energy plasma particles rigidly corotate with Saturn's magnetic field and preferentially strike the trailing hemispheres of the moons, relativistic electrons (> 1 MeV) behave differently. Due to the strong radial gradient of Saturn's magnetic field, the gradient-curvature drift of these high-energy electrons forces them to travel in a direction opposite to the corotating plasma flow. Consequently, these MeV electrons preferentially bombard low latitudes on the leading hemispheres (the sides facing forward in their orbits) of the inner moons. This continuous deposition of high-energy electron dose alters the microstructural state of the surface water ice. Under normal conditions, the surface of these moons consists of highly porous, fluffy, micron-scale frost grains. However, when relativistic electrons penetrate centimeters into the subsurface, they excite and mobilize water molecules. These mobilized molecules migrate and recondense at the contact points between adjacent grains, a process known as radiolytic sintering. This sintering effectively "glues" the ice grains together, transforming a loose, porous regolith into a highly compacted, dense, crystalline ice layer. This mechanism increases the thermal conductivity and thermal inertia of the surface, producing regions that remain cooler during the day and warmer at night compared with the surrounding terrain. The characteristic "Pac-Man" shapes arise because the energetic electrons trapped in Saturn's magnetosphere do not impact the surfaces of Mimas and Tethys uniformly. Since Saturn's magnetospheric plasma corotates with the planet faster than the moons orbit Saturn, the electrons preferentially sweep onto the leading hemispheres of the satellites. However, the electron trajectories are also guided by the geometry of Saturn's magnetic field, causing the strongest bombardment to concentrate in a broad equatorial region while partially avoiding a wedge-shaped sector. The combination of concentrated irradiation and a relatively protected sector produces the circular thermal anomaly with a missing "mouth-like" section that resembles the classic "Pac-Man" shape (Figure 5.2). On Tethys, the anomaly is weaker because the surface is also continuously recoated by fresh icy particles originating from Enceladus, partially counteracting the sintering process. In addition to modifying thermal properties, the compacted ice alters the optical scattering behavior of the surface. Because the ice grains are tightly fused together by electron bombardment, they highly scatter solar short ultraviolet wavelengths, appearing as a bright, distinct bluish signature on false-color global maps. Conversely, the famous yellow and red signatures are produced by the thermal behavior of the surface; this compacted brick of ice has high thermal inertia, meaning it absorbs and conducts heat during the day rather than letting it escape. When the sun goes down, this region stays warmer for longer than the surrounding fluffy snow, glowing brightly in

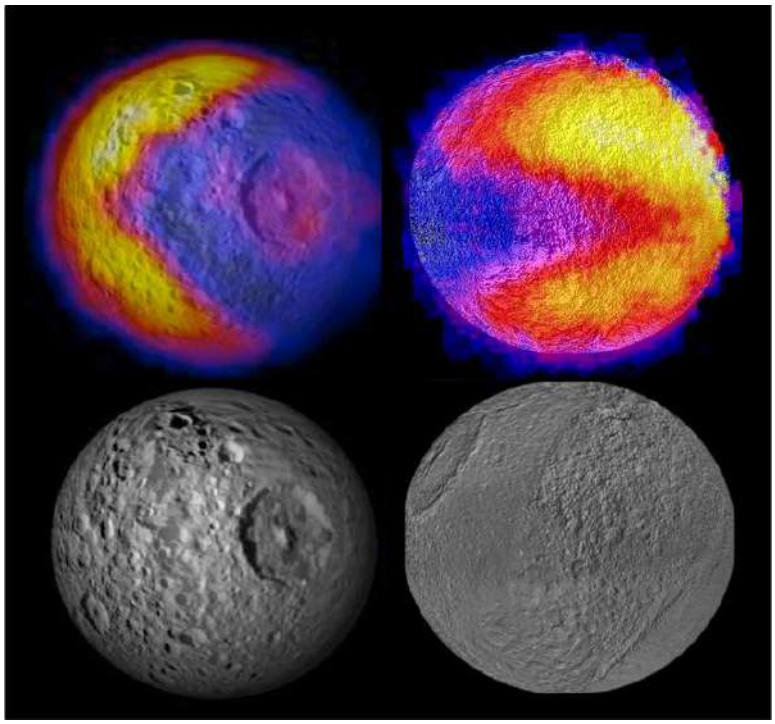

Figure 5.2: Thermal “Pac-Man” anomalies on the leading hemispheres of Mimas (left) and Tethys (right). The upper panels show thermal maps derived from Cassini observations, highlighting the characteristic wedge-shaped regions produced by the preferential bombardment of high-energy electrons trapped in Saturn’s rotating magnetosphere. The lower panels show corresponding visible-light images of the two satellites.

the long thermal infrared wavelengths.

5.2.2 Is Enceladus surface a chemical reactor?

Enceladus represents a unique case in Saturn’s magnetosphere. Rather than acting as a simple passive absorber of radiation, this active moon operates as a giant electrodynamic engine that fundamentally shapes the magnetospheric plasma, magnetic field, and energetic particle populations of the entire Saturnian system.The south polar terrains of Enceladus feature parallel tectonic fissures ("tiger stripes") that continuously vent up to 1000 kg/s of water vapor, ice grains, and minor volatiles (CO_2, CH_4, NH_3, and H_2) into space. Approximately 100 kg/s of this neutral gas is ionized through charge exchange, photoionization, and electron impact, creating a massive plasma loading rate. This mass-loading slows down the local corotating magnetospheric plasma. To analyze the physical boundary of this interaction, Cassini investigators established clear observational criteria to distinguish between the dense, active cryovolcanic plume region and the surrounding diffuse plasma torus (Teolis et al., 2017).

A significant fraction of the emitted water ice grains consists of sub-micrometer dust that populates the broad E-ring. As these dust grains traverse the plasma-rich environment, they collect free electrons due to their high electron affinity. Cassini measurements showed that up to 50% or more of the local electron population is attached to these dust grains. This creates a peculiar dusty plasma where the negative charge carriers are dominated by heavy, sub-micron dust particles rather than free electrons. Such icy water grains convey an important astrobiological information: while grains are compositionally dominated by relatively pure water ice, they do contain silica nanoparticles dissolved from the moon’s hot, rocky ocean floor, confirming that active hydrothermal vents exist inside Enceladus.

The energetic particle environment striking the surface of Enceladus is complex, consisting of both magnetospheric electrons and ions trapped within Saturn’s magnetic field. While the dense, charged plume environment can locally deflect or absorb suprathermal electrons and lower-energy ions, ultra-high-energy electrons and heavy water-group ions completely bypass this atmospheric shield to actively bombard the icy surface. Electrons span a broad energy

range from a few eV up to MeV energies. Cold and thermal electrons (a few eV to tens of eV) participate mainly in plasma charging and low-energy surface interactions. Suprathermal and energetic electrons (hundreds of eV to hundreds of keV) penetrate micrometers to millimeters into the surface ice, generating secondary electrons and radicals. Relativistic electrons (MeV range) are present in Saturn's radiation belts, though their flux at Enceladus is lower than in the inner magnetosphere. Simultaneously, low-energy (10 to 45 keV) water-group ions easily overcome local shielding to reach the surface, delivering a high flux of heavy-particle impacts.

Together, this combined ion and electron bombardment drives intense radiolysis of the surface water ice mixed with trace volatiles (CO_2, CH_4, NH_3). By breaking molecular bonds within the ice matrix, these energetic particles trigger complex chemical pathways. Under sustained irradiation, simple species such as carbon monoxide (CO), cyanate (OCN^-), and ammonium (NH_4^+) are rapidly produced from the irradiation of water-rich icy mixtures containing carbon- and nitrogen-bearing molecules. Alongside these primary radiolytic products, smaller amounts of more complex organic compounds, including formamide ($HCONH_2$), acetylene (C_2H_2), acetaldehyde (CH_3CHO), and hydroxymethyl radicals, can also form directly within the irradiated ice matrix. As the processed material subsequently experiences thermal warming, radicals trapped in the ice become mobile and undergo additional reactions that synthesize more chemically evolved compounds, such as carbamic acid (NH_2COOH), ammonium carbamate ($H_2NCOONH_4$), and several alcohol species. These processes are particularly important because the formation timescales of the radiolytic products are comparable to the exposure times of plume-derived material redeposited onto the surface. Consequently, the detection of organic molecules in data collected by the Cassini–Huygens does not necessarily imply an exclusive origin within Enceladus's subsurface hydrothermal ocean. At least part of the observed chemical complexity may instead result from ongoing surface processing induced by magnetospheric irradiation (Bergantini et al., 2014; Richards et al., 2025).

5.3 Ion and electron radiolysis of Enceladus's surface ice

A multi-scale energy down-conversion process drives the surface chemistry of Enceladus, dictated entirely by the nature and energy spectrum of the incoming magnetospheric particles. This radiation environment is divided into distinct plasma populations, beginning with a cold, low-energy thermal background consisting of electrons and ions under 1 keV. Because Enceladus lacks a global atmosphere or an internal magnetic field, this cold population is only deflected locally at the South Polar Terrain, where the cryovolcanic plume ionizes and induces a temporary magnetic draping barrier. The primary drivers of global surface radiolysis, however, are the higher-energy populations that easily bypass this regional polar shield due to their inherent physical properties. The first key population consists of energetic water-group ions, specifically O^+, OH^+, and H_2O^+, carrying kinetic energies between 10 and 45 keV. Despite the local magnetic draping caused by the plume, these heavy ions possess high mass-to-charge ratios that grant them immense gyroradii, allowing them to ignore the local electromagnetic disturbance and plow ballistically even into the southern and trailing ice. The second population comprises ultra-high-energy radiation belt electrons spanning from 10 keV to several MeV. Moving at relativistic velocities, these light but extraordinarily fast particles act as kinetic bullets, possessing far too much momentum to be deflected or attenuated by weak local fields or the tenuous plume gas. Consequently, while the localized polar plume filters out the low-energy background, the rest of Enceladus's naked surface stands entirely exposed to the full, unfiltered spectrum of both $10 - 45$ keV energetic ions and MeV electrons, driving continuous, deep radiolytic processing across the global icy regolith.

When primary water-group ions penetrate the dirty water-ice matrix, they drive radiolytic processes governed by electronic and nuclear stopping channels. At the beginning of the trajectory, the high-velocity ion loses energy predominantly through electronic stopping, transferring its kinetic energy via inelastic Coulomb interactions with the electron clouds of target molecules like H_2O, CO_2, CH_4, and NH_3. This creates a dense track of secondary electrons that triggers an extended ionization cascade and cleaves molecular bonds within nanometric volumes. This intense energy deposition yields a highly reactive matrix of radicals and ions, such as OH, H, O, NH_2, CH_3, and CO, inducing severe chemical non-equilibrium and structural disorder. As the projectile ion slows down and drops into the lower velocity regime, the dominant energy-transfer mechanism shifts to nuclear stopping. Here, the ion undergoes elastic collisions directly with target atomic nuclei, depositing momentum that causes collision cascades, molecular displace-

ment, and localized amorphization of the ice lattice. Near the very end of the ion track, where nuclear stopping power peaks, these elastic collisions can trigger sputtering by ejecting surface molecules into space. Ultimately, because these combined stopping mechanisms constrain the overall penetration depth of $10 - 45$ keV ions to the upper tens to hundreds of nanometers, the resulting radiolytic processing, molecular fragmentation, and lattice damage are strictly confined to a shallow surface layer of Enceladus's regolith.

Conversely, incoming high-energy primary electrons lose energy almost exclusively through electronic collisions, as their negligible mass prevents efficient momentum transfer to heavy atomic nuclei. This drives impact ionization, where the kinetic energy of the incoming primary electron overcomes the binding energy of target valence electrons, forcibly ejecting them and liberating thousands of secondary electrons along a deep penetration track extending millimeters to centimeters into the bulk ice. If any of these liberated secondary electrons retain kinetic energy greater than the ionization potential of water ice ($\sim$ 12 eV), they can trigger further ionization events. However, because electron-impact ionization is a probabilistic scattering process governed by quantum cross-sections, the probability of ionization drops to near zero at the bare threshold and peaks efficiently only when electron energies reach approximately 100 eV. Electrons traversing intermediate regimes instead induce purely electronic or vibrational excitations, gradually losing energy until the entire population settles into a cascade of low-energy tertiary electrons throughout the bulk ice radiolysis zone.

While a negligible fraction of the secondary electrons generated within the topmost 1 to 5 nanometers escapes back into space as secondary emission, the vast majority are driven deeper into the regolith, where they undergo a rapid thermalization cascade. This deceleration process begins efficiently when the cascading electrons drop into the sub-excitation regime, once their energies fall below the lowest electronic excitation threshold of ASW ($\sim$ 8.2 eV), so that electrons lose the capacity to induce further electronic transitions. Instead, they enter a prolonged cooling phase where they transfer kinetic energy in exciting intramolecular vibrations, such as H_2O stretching and bending modes at $0.1 - 0.5$ eV, and lattice phonons. Because the electrons slow down significantly during this regime, their prolonged interaction time with individual molecules makes the sub-excitation phase highly efficient for Dissociative Electron Attachment (DEA). This quantum-resonant process occurs when a low-energy electron is captured into an empty molecular orbital of a neutral target volatile, generating a short-lived, transient negative ion state. If the lifetime of this temporary state exceeds the vibrational period of the molecular bond, the molecule undergoes rapid, unimolecular dissociation before autodetachment can take place. For example, when interacting with the dominant water ice matrix, DEA directly cleaves the O–H bond to yield a stable negative ion and a highly reactive neutral radical fragment via the resonant pathway $e^- + H_2O \rightarrow (H_2O^-)^\star \rightarrow H^\star + OH^-$ (see Schmidt et al. 2022 for details). Electrons that bypass DEA continue to undergo inelastic phonon scattering, transferring the remainder of their kinetic energy directly into the vibrational and rotational modes of the surrounding ice lattice. This rapid cooling to thermal equilibrium brings the electrons into complete thermal equilibrium with the ambient temperature of Enceladus's surface ice ($60 - 80$ K). This final thermalization phase effectively drops their kinetic energies to the millielectronvolt scale, $k_B T \sim 5 - 10$ meV, stabilizing the particles before they localize into structural defects or cavities within the amorphous matrix.

Once fully thermalized, these low-energy electrons do not remain free but instead become solvated or trapped electrons. They localize within pre-existing structural defects, interstitials, or cavities inherent to the radiation-damaged, amorphous ice matrix, prompting surrounding water molecules to reorient their dipoles and construct a localized potential well around the charge. This trapping mechanism fundamentally alters both the surface chemistry and physical properties of the regolith. Chemically, these trapped electrons function as long-lived, localized reducing agents that remain suspended in the matrix until they undergo quantum tunneling reactions with nearby radiolytic radicals or migrating ions. Physically and optically, they act as color centers (F-centers), because their localized potential wells introduce discrete electronic states capable of absorbing light across the visible and near-infrared spectra. However, for Enceladus, spacecraft data do not provide clear evidence for a distinct trapped-electron absorption band or a strong colour-centre signature; any such effect appears at most subtle compared with grain-size changes, fresh ice exposure, and minor contaminants.

Table 5.2: List of the experiments and corresponding physical parameters. All experiments were performed using a $CaF_2 + Na_3PO_4$ substrate.

Exp.	ice	irradiation (keV)	irradiation time (s)	temperature (K)
1	no	no	0	10
2	no	no	0	300
3	no	1	10800	80
4	no	2	10800	80
5	H_2O	1	3600	11
6	H_2O	1	3600	80
7	H_2O	1	3600	100
8	H_2O	1	3600	130
9	H_2O	2	10800	11
10	H_2O	2	10800	80
11	H_2O	2	10800	100
12	H_2O	2	10800	130
13	H_2O,CO	1	3600	12
14	H_2O,CO	2	3600	12

5.4 Experiments

The experiments were carried out using the IEPS at the National Central University, Taiwan. The associated UHV chamber, irradiation sources, and diagnostic instruments have been described in detail in Chapter 2.

5.4.1 Substrate preparation and conditioning

Sodium phosphate (Na_3PO_4) powder (Sigma-Aldrich, 96% purity) was mixed with a small amount of water to form a paste, which was subsequently applied onto a CaF_2 window. After the mixture was thoroughly dried to ensure the evaporation of water molecules, the window was mounted onto the cryostat inside the UHV chamber. The entire system was then baked at 100°C for 48 hours to minimize background contamination. Prior to each experimental run, the system was stabilized for 1 hour at 200 K under UHV conditions, maintaining a fixed initial deposition pressure of 5×10^{-9} Torr.

5.4.2 Experimental procedure

The experimental sequence consists of four distinct phases: cooling, deposition, irradiation, and thermal desorption (mode 3, see Section 2.4). Initially, an infrared spectrum is recorded at room temperature to establish a baseline and verify standard system performance. The substrate is then cooled to the target temperature. Once the target temperature stabilizes, the ice mantle mixture is prepared within the gas-line system and introduced into the UHV chamber via a leak valve, condensing onto the cold substrate. Following the completion of the deposition phase, the ice layer is bombarded by the electron gun to induce and investigate photochemical and photophysical processes. Finally, during the warming-up phase, temperature-programmed desorption (TPD) is performed at a linear heating rate of 2 K min^{-1}. The thermally desorbed species are continuously monitored via QMS to identify and analyze the photoproducts synthesized during the irradiation phase. The complete set of experiments have been summarized in Table 5.2.

5.5 Results

The experimental investigation was carried out to evaluate the non-thermal, radiolytic alteration of sodium orthophosphate Na_3PO_4 and its chemical interaction with overlying volatile ice layers under simulated icy moon surface conditions. The condensed-phase evolution was monitored using mid-FTIR spectroscopy, complemented by gas-phase diagnostics via QMS during TPD.

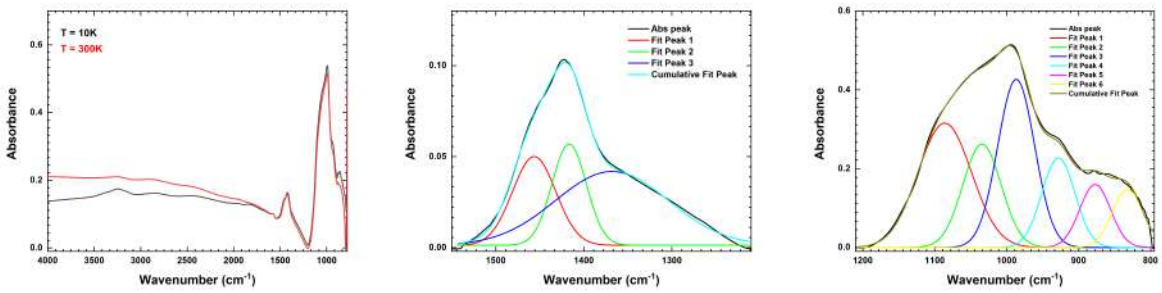

Figure 5.3: FTIR spectroscopic characterization of pristine Na_3PO_4. The left panel displays the raw absorbance spectra at 300 K and 10 K. Middle and right panels illustrate the multi-peak Gaussian deconvolution used to resolve individual structural and environmental vibrational modes.

5.5.1 Characterization of pristine Na_3PO_4

Initial infrared spectra of the pristine Na_3PO_4 substrate pasted onto a CaF_2 window were recorded at 300 K and 10 K prior to irradiation. prior to irradiation. As illustrated in Figure 5.3 (left panel), the spectra at both temperatures exhibit nearly identical absorption features within the $4000-800$ cm^{-1} spectral range, indicating that the baseline structure of the orthophosphate salt remains thermally stable across this regime.

The profile is dominated by an intense and broad envelope spanning 1200 to 780 cm^{-1}, which arises from multiple heavily overlapping vibrational modes of the phosphate structure. To isolate and identify individual vibrational contributions, a Gaussian deconvolution was applied to the spectral region and the adjacent high-wavenumber region $1560-1200$ cm^{-1} (Figure 5.3, middle and right panels). The specific peaks resolved from the Gaussian fit and their structural assignments are detailed as follows

- 832 cm^{-1}: attributed to the symmetric bending modes of P–O–P linkages coupled with the wagging modes of tightly bound or adsorbed water molecules (Nakamoto, 2009; Banach & Makara, 2011; Johnston, 2013));
- 877 cm^{-1}: assigned to the asymmetric bending vibrations of P–O–P bridges, with additional contributions from the librational modes of structured matrix water (Bellamy, 2013; Johnston, 2013);
- 928 cm^{-1}: designated as the symmetric stretching mode of bridging P-O-P units, characteristic of condensed polyphosphate or pyrophosphate arrangements (Tao, 2013; Baino & Kargozar, 2022);
- 986 cm^{-1}: corresponds to the symmetric stretching mode of terminal PO_3^{2-} groups, typical of Q^1 structural units in phosphate networks (Gunter et al., 1996; Tao, 2013; Swain, 2018);
- 1034 cm^{-1}: attributed to the asymmetric stretching mode of bridging P–O–P groups located in chain-like Q^2 metaphosphate units (Gunter et al., 1996; Xu et al., 2024);
- 1086 cm^{-1}: assigned to the asymmetric ν_3 stretching vibration of non-bridging P=O bonds within terminal PO_2^- or PO_3^{2-} architectures (Q^1 structures) (Tarte, 1967; Gunter et al., 1996; Tao, 2013; Trivedi et al., 2015; Xu et al., 2024);
- 1368 cm^{-1}: attributed to local P–OH deformation or isolated P=O stretching modes (Banach & Makara, 2011; Trivedi et al., 2015);
- 1416 cm^{-1} and 1456 cm^{-1}: associated with trace atmospheric carbonate contamination CO_3^{2-} substitution), secondary polyphosphate overtones, or combination bands (Johnston, 2013; Sakpal et al., 2019);

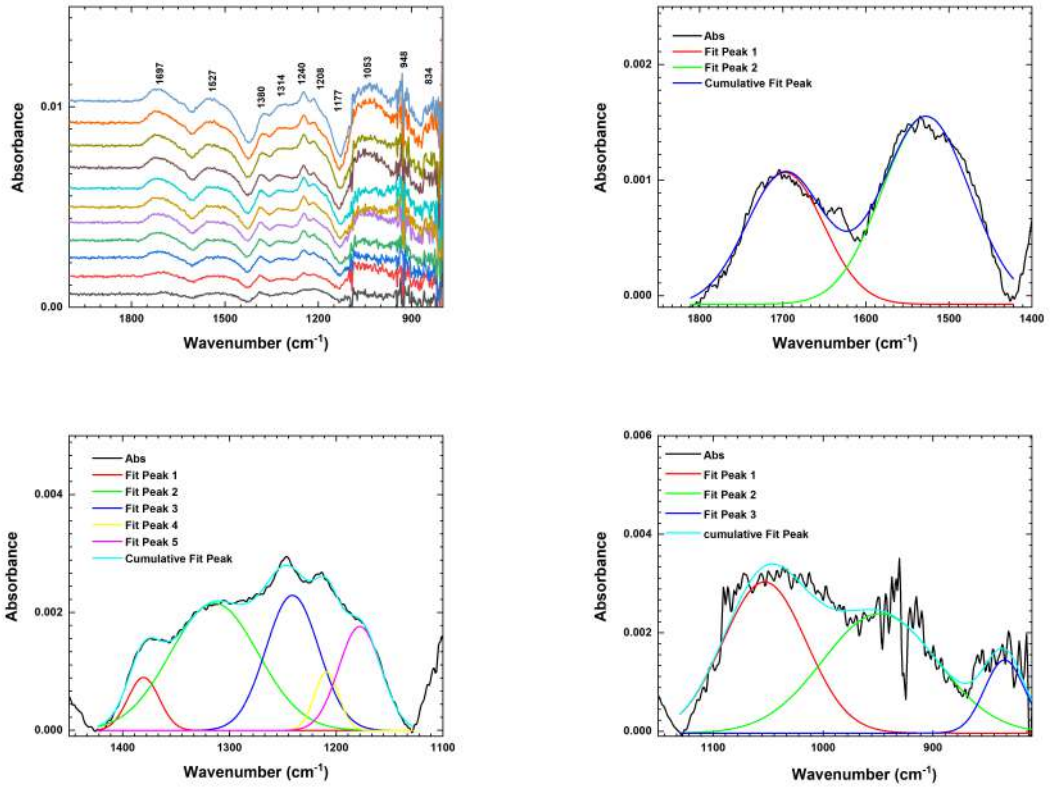

Figure 5.4: FTIR spectra of Na_3PO_4 recorded at different irradiation times (30, 90, 180, 360, 660, 1200, 2100, 3600, 5400, and 10800 s) under 1 keV electron irradiation. (a) Full spectral range ($2000 - 730$ cm^{-1}) showing the temporal evolution of the irradiated samples. (b) Expanded view of the 1800˘1400 cm^{-1} region. Gaussian deconvolution of the spectrum acquired after 10800 s irradiation in the regions (c) $1400 - 1100$ cm^{-1} and (d) 1100˘900 cm^{-1}. Labels indicate vibrational features reported in Table 5.3, highlighting the evolution and redistribution of absorption bands.

- 1572 cm^{-1} and 3246 cm^{-1}: assigned to the deformation/bending and stretching modes (ν_1, ν_3) of residual hydrogen-bonded structural water molecules, along with potential matrix-confined trace oxygen (Jha et al., 2015).

5.5.2 Electron irradiation of pristine Na_3PO_4

To assess the radiolytic stability and structural transformations of the mineral matrix, bare Na_3PO_4 thin films were subjected to high-vacuum electron bombardment at 80 K using 1 and 2 keV electrons. The baseline infrared profile undergoes clear, dose-dependent changes tracked across progressive time increments up to 10,800 seconds. The spectral changes induced by 1 keV electrons in 1 hour irradiation are displayed in Figure 5.4, while the corresponding time-resolved spectra for 2 keV electrons and 3 hours irradiation are shown in Figure 5.5. These post-irradiation intervals reveal the appearance of multiple additional bands, denoting structural lattice modifications and chemical pathways missing from the pristine material.

While the core framework of the phosphate matrix remains structurally intact after irradiation, the incoming energetic electrons break local symmetries. In an ideal, undisturbed orthophosphate crystal, fewer bands are active because the tetrahedra occupy highly symmetric local environments. Electron exposure introduces deep lattice defects, local mechanical strain, and sodium cation displacement. This interaction lowers the local site symmetry and lifts the vibrational degeneracy of the PO_4^{3-} units, causing the core profile to split into distinct, non-equivalent bonding environments visible in the post-irradiation profiles of Figure 5.4 and Figure 5.5. Specifically, the post-irradiation emergence of higher-wavenumber bands extending above 1120 cm^{-1} (such as 1129, 1131, 1159, 1177, and 1198 cm^{-1}) indicates the development

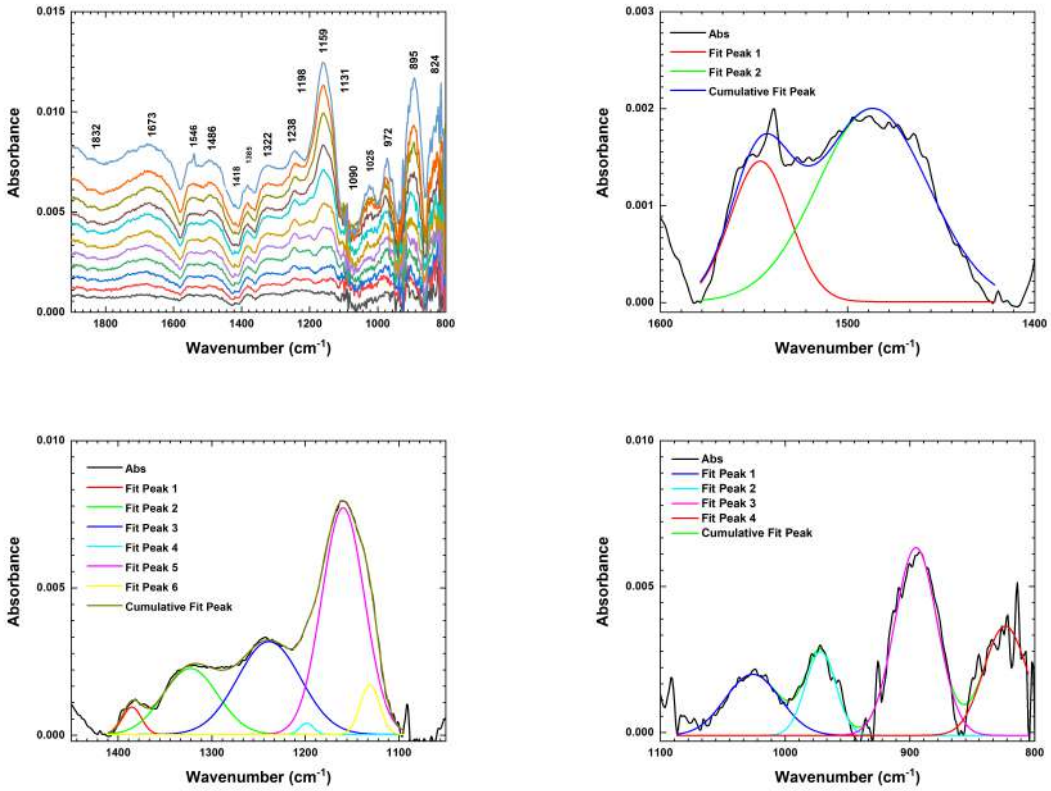

Figure 5.5: Same as in Figure 5.4, but for Na_3PO_4 irradiated with 2 keV electrons.

of increasingly asymmetric P−O bonds, defect-rich phosphate units, and altered non-bridging oxygen environments.

A direct comparison between the FTIR spectra obtained after 3 hours of irradiation with 1 keV and 2 keV electrons is shown in Figure 5.6. Irradiation at the higher energy of 2 keV results in enhanced band intensities and the appearance of new absorption bands compared to 1 keV processing. This energy dependence highlights that: higher-energy (2 keV) electrons penetrate deeper into the salt substrate film; this deeper penetration path produces a larger absolute volume of structural disorder; the increased electron interaction enhances local bond polarization and yields a higher total density of stabilized lattice defects.

Beyond internal structural changes within the bulk matrix, electron processing actively drives non-equilibrium chemical reactions at the outermost surface interface by interacting with residual vacuum background gases. Even under HUV conditions, trace amounts of atmospheric contaminants, predominantly residual water vapor and CO_2, unavoidably outgas from the chamber walls and adsorb onto the sample. Under 2 keV electron bombardment, the emergence of a distinct infrared absorption band at 824 cm^{-1} provides definitive evidence of surface hydroxylation, tracking the synthesis of new P−OH chemical groups formed when the radiolytically fractured, highly reactive surface phosphate units capture active hydrogen or hydroxyl fragments derived from the dissociation of residual background water molecules. Carbonyl and complex formation also occur: new absorption bands emerging between 1673 cm^{-1} and 1832 cm^{-1} can be assigned to C=O stretching vibrations, while the peak at 2043 cm^{-1} indicates the synthesis and stabilization of metal-carbonyl (metal–CO) complexes from contamination reactions inside the chamber. The observed band positions and their respective vibrational assignments before and after electron irradiation are reported in Table 5.3.

5.5.3 Deposition of H_2O ice over Na_3PO_4 at various temperatures and irradiation with 1 keV and 2 keV electrons

To simulate the complex molecular processing occurring within icy planetary bodies, we condensed a water ice onto the pristine sodium orthophosphate substrate. Substrate processing

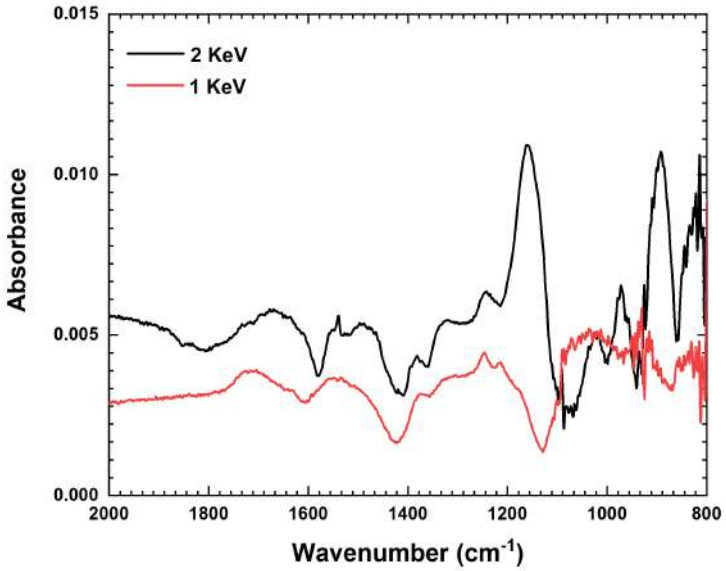

Figure 5.6: Comparison between the FTIR spectra of Na_3PO_4 obtained after 3 h of irradiation with 1 keV and 2 keV electrons.

Table 5.3: Infrared band positions and assignments for pristine and electron-irradiated Na_3PO_4.

No.	Na_3PO_4 (cm^{-1})	1 keV (cm^{-1})	2 keV (cm^{-1})	Assignment	Relevant references
1	—	—	824	P−OH	Banach & Makara (2011)
2	832	834	—	P−O−P	Banach & Makara (2011); Johnston (2013)
3	877	—	858	asym bend P−O−P	Bellamy (2013); Tao (2013)
4	—	—	895	P−O−P	Moustafa & El-Egili (1998)
5	928	—	—	sym stretch P−O−P	Tao (2013); Baino & Kargozar (2022)
6	—	948	948	sym PO_4^{3-} stretch	Gunter et al. (1996); Tao (2013)
7	—	—	972	sym P−O stretch	Johnston (2013)
8	986	—	—	sym stretch PO_2	Gunter et al. (1996); Swain (2018)
9	—	—	1026	asym PO_3 stretch	Gunter et al. (1996)
10	1034	—	—	asym stretch P−O−P	El-Meliegy & Van Noort (2011)
11	—	1053	—	asym PO_4^{3-} stretch	Zarif et al. (2022)
12	1086	—	—	asym stretch P=O	Tao (2013); Tarte (1967); Trivedi et al. (2015)
13	—	1129	1090	asym PO_3 stretch	Banach & Makara (2011)
14	—	—	1131	PO_2 stretch	Mohan Babu et al. (2020); Yang et al. (2015)
15	—	—	1159	P=O	Trivedi et al. (2015)
16	—	1177	—	P=O stretch	Trivedi et al. (2015)
17	—	—	1198	P−O stretch	Jastrzebski et al. (2011)
18	—	1208, 1240	1238	?	—
19	—	1314	1322	CO_3^{2-}/P−OH/P=O stretch	Tao (2013)
20	1368	—	1364	P−OH or P=O stretch	Banach & Makara (2011); Trivedi et al. (2015)
21	—	1380	1385	CO_3^{2-}/P−OH/P=O stretch	Tao (2013)
22	—	1421, 1608	—	—	Tao (2013)
23	1416, 1456	—	1418, 1486, 1410	carbonate/polyphosphate	Johnston (2013); Sakpal et al. (2019)
24	—	1527	1546	?	—
25	1572	—	—	OH stretch	Jha et al. (2015)
26	—	—	1580	—	—
27	—	1697	1673	C=O stretch/O−H bend	Hudson et al. (2018); Seki et al. (2020)
28	—	—	1832	C=O	Coates (2000)
29	—	—	2043	metal-CO	Ekou et al. (2016)

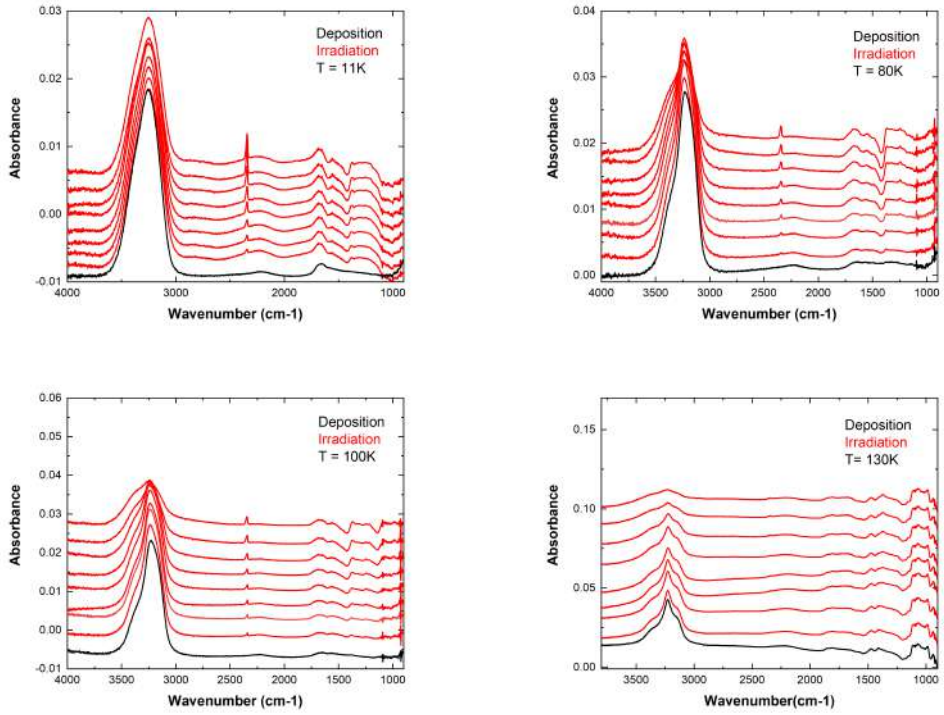

Figure 5.7: FTIR spectral evolution of H_2O ice overlayers on Na_3PO_4 substrates during 1 keV electron irradiation for a fixed duration of 1 hour, comparing the temperature-dependent behaviors of experiments 5 (11 K), 6 (80 K), 7 (100 K), and 8 (130 K). The profiles illustrate the progressive radiolytic depletion of the parent H_2O matrix alongside the concomitant synthesis of major irradiation products.

involved milling high-purity Na_3PO_4 salt (96% analytical purity, Sigma Aldrich) into a homogeneous microcrystalline powder, suspending it in an aqueous slurry, and casting a thin, uniform layer onto a calcium fluoride optical window. To drive off residual hydration layers and volatile atmospheric contaminants, the optical window assembly was subjected to an in-vacuo thermal baking cycle at 100 °C for a duration of 48 hours within the UHV chamber. As detailed in Table 5.2, in this Section we present experiments 5 to 12. The mid-infrared spectroscopic profiles of pure solid-state water ice overlayered onto sodium orthophosphate substrates, acquired both prior to and following non-thermal processing via electron radiolysis, are systematically illustrated in Figures 5.7 and 5.8. To highlight the temperature dependence of these physical processes, independent experimental sequences (experiments 5, 6, 7, 8) at 1 keV for 1 hour, and (experiments 9, 10, 11, 12) at 2 keV for three hours, were executed across 4 temperatures: 11, 80, 100, and 130 K. In the pre-irradiation baseline spectra, the condensed water matrix displays its characteristic ν_2 bending mode near 1655 cm^{-1} and a broad ν_1/ν_3 stretching envelope around 3255 cm^{-1}. As the deposition temperature increases from 11 K to 130 K, this stretching profile undergoes a distinct redshift, narrowing, and sharpening, serving as a direct spectroscopic indicator of the structural phase transition from disordered ASW to an ordered crystalline ice lattice.

Electron bombardment drives fluence-dependent modifications across all matrix configurations (experiments $5-12$), where the continuous decay in the parent H_2O integrated area confirms radiolytic matrix destruction alongside the synthesis of identical byproducts, varying only in relative intensities and minor spectral shifts. Hydrogen peroxide H_2O_2 synthesis is monitored via its 2871 cm^{-1} combination band (Loeffler et al., 2006), with its 1455 cm^{-1} asymmetric bending mode resolved exclusively in the highest-temperature experiment 8 (130 K), while remaining below detection thresholds in colder setups. Conversely, the 1142 cm^{-1} feature of the oxonium radical OH_3 (Mejía et al., 2022) cannot be clearly resolved due to severe spectral overlap with the intense 1171 cm^{-1} P−O stretching band of the underlying phosphate substrate. Concurrently, an intense feature emerges at $\sim$ 1550 cm^{-1}, growing monotonically

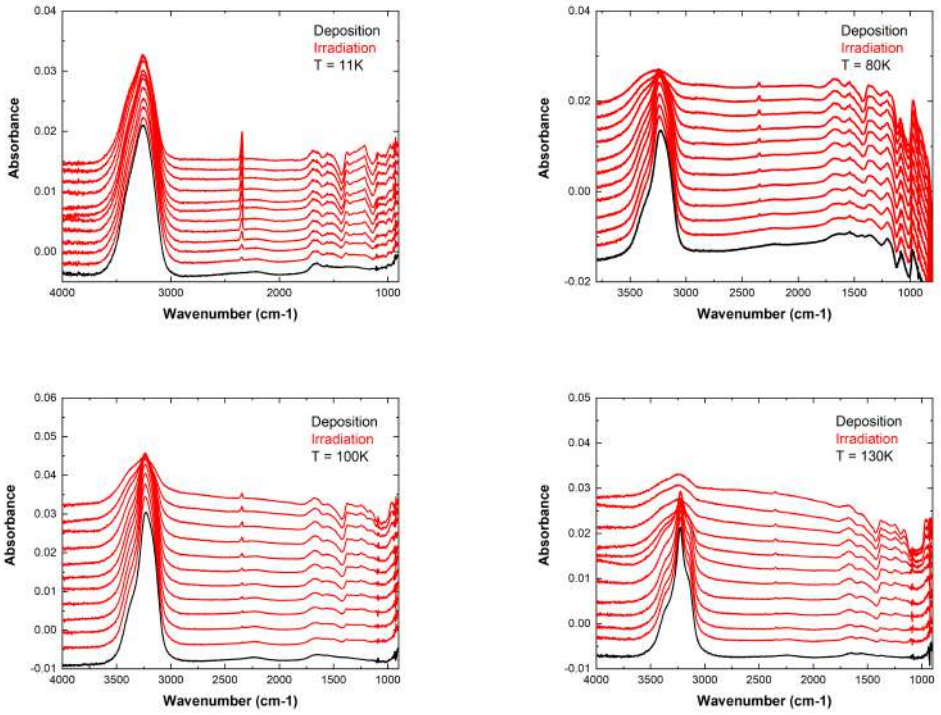

Figure 5.8: Same as for Figure 5.7 for 2 keV electrons and 3 hour irradiation time.

and sharpening with fluence, which is assigned to trapped molecular oxygen O_2. Although normally infared forbidden, severe symmetry breaking induced by irradiation defects, localized pores, and strong interfacial electric fields generates a non-zero dipole moment, rendering the O_2 transition weakly infrared active (Loeffler et al., 2006b). This assignment is validated by previous observations of perturbed O_2 in water matrices near 1551 cm^{-1} (Müller et al., 2018) and H_2O-O_2 complexes spanning the $1548-1590$ cm^{-1} range (Cooper et al., 2008). Other potential carriers in the $1500-1600$ cm^{-1} domain, such as perturbed HO_2 bending states, isolated hydroxyl radicals, or active ionic complexes, are excluded by the thermal stability of this band and the total absence of accompanying structural features (Cooper et al., 2008; Lo et al., 2022). Finally, the ionic Na_3PO_4 core enhances defect density which acts to stabilize the trapped O_2 at the salt-ice interface, while the narrowing of the 1550 cm^{-1} feature at elevated temperatures reflects the thermal annealing of heterogeneous defect sites, which redistributes the trapped O_2 into a highly uniform, thermodynamically favored trapping environment. Minor features between 1374 and 1382 cm^{-1} correspond to a superposition of the altered substrate's fundamental P−OH stretch and localized formate anions $HCOO^-$ produced via thesecondary electron cascade (Banach & Makara, 2011). Finally, a weak residual band at 1088 cm^{-1} tracks the asymmetric P=O modes of the underlying salt structure.

Trace vacuum contamination introduces minor reaction channels, beginning with a discrete carbon dioxide feature at 2344 cm^{-1}. Interactions between this condensed carbon and reactive water radiolysis fragments synthesize trace organic structures, evidenced by neutral formic acid bands growing around 1676 and 1244 cm^{-1}.

The kinetic decay profiles of parent water ice display a non-linear trend, where the 11 K environment demonstrates the highest cross-sectional resistance to radiolytic destruction across both energy regimes, confirming that extreme cryogenic conditions structurally lock the lattice and limit molecular mobility. Interestingly, the high-flux 2 keV beam drives a drastically enhanced depletion of water ice at elevated temperatures (80 K and 130 K), collapsing the absolute ice thickness down to ~ 20 ML compared to the ~ 40 ML residual baseline observed under 1 keV exposure. Concurrently, the synthesis kinetics of secondary species diverge heavily based on beam energy and product stability. The 2 keV regime is highly efficient at generating molecular oxygen, nearly doubling the 1 keV yield at 11 K with an integrated band area of ~ 0.20. Conversely, hydrogen peroxide accumulation is favored under the lower-energy 1 keV

regime, achieving column densities between $0.7 - 0.8$ ML against $\lesssim 0.4$ ML at 2 keV, while its significant statistical scatter reveals it behaves as a transient intermediate subjected to competing synthesis and electron-induced dissociation channels. Ultimately, while the high flux and enhanced energy of 2 keV projectiles maximize water ice loss and O_2 generation, they severely limit the stable accumulation of H_2O_2, whereas the less destructive 1 keV regime proves highly conducive to stable H_2O_2 preservation. In Figure 5.9, we report the column density evolution of H_2O, and H_2O_2, as functions of the fluence.

Following irradiation, TPD annealing up to 300 K at 2 K/min tracked phase transitions, molecular desorptions, and stable residues. Results are shown in Figure 5.10, and line assignments reported in Table 5.4. While pure multilayer water ice sublimates completely near 160 K under ultra-high vacuum, water signatures within this configuration anomalously persist up to 300 K. This extreme thermal stability highlights water-phosphate interactions, where the high hygroscopicity of sodium orthophosphate efficiently coordinates a tightly bound monolayer of hydration water and surface hydroxyl groups via strong ion–dipole interactions with Na^+ cations and non-thermal interfacial dissociation that forms desorption-resistant P−OH groups. Similarly, the O−H stretch in hydrogen peroxide at 2871 cm^{-1} sharpens and intensifies during initial warm-up due to matrix crystallization rearranging the local electrostatic environment, while strong interactions with Na^+ ions and surface hydroxyl sites stabilize the peroxide fraction to survive at elevated temperatures. Spectroscopically, the Na_3PO_4 Na substrate is initially obscured by the large optical depth and dielectric screening of the low-temperature ice, leaving the $1130 - 1200$ cm^{-1} region dominated by librational and combination modes of interfacial H_2O hydrogen-bonded to $PO_4{}^{3-}$ tetrahedra. Above ~ 170 K, bulk water sublimation unmasks the substrate, allowing the asymmetric phosphate stretching modes ν_3 to emerge at 1136, 1171, and 1200 cm^{-1}. Compared to the radiolysis of bare, dry Na_3PO_4 (where defects generate a PO_2 stretch at 1131 cm^{-1} and an unhindered terminal P=O stretch at 1177 cm^{-1}, see Table 5.3), the overlayered ice experiments shift these features to 1136 cm^{-1} and 1171 cm^{-1}. This frequency divergence provides definitive evidence of local dielectric and coordination alterations at the solid-ice boundary: the 5 cm^{-1} blue-shift of the 1131 cm^{-1} mode tracks the efficient protonation of damaged orthophosphate units into stable $HPO_4{}^{2-}$ architectures driven by mobile water radiolytic fragments, while the 6 cm^{-1} red-shift of the P=O mode to 1171 cm^{-1} confirms localized hydrogen-bonding interactions (P=O$\cdots$H−O−H) sustained by the residual interfacial hydration water. Meanwhile, the absolute structural persistence of the high-frequency component near 1200 cm^{-1} across both environments confirms that the core condensation pathways of the phosphate backbone remain robust, with rising intensities reflecting optical unmasking and thermal relaxation rather than new species. The defect-activated O_2 feature at 1551 cm^{-1} persists up to 300 K, indicating deep interfacial trapping sites at the salt boundary that inhibit molecular escape. Finally, a carbonyl C=O stretching band appearing at 1833 cm^{-1} survives to room temperature, assigned to formyl ·HCO or HOCO radical complexes stabilized through electrostatic interactions with the ionic Na_3PO_4 surface.

Minor contaminant bands also evolve during annealing; the $HCOO^-$ features at 1382 cm^{-1} (2 keV) and 1374 cm^{-1} (1 keV) disappear near 180 K as molecular mobility promotes protonation or desorption, yielding sharper bands at 1423, 1440, and 1519 cm^{-1} from stabilized HCOOH networks, while the broad HCOOH feature at 1676 cm^{-1} persists throughout the warm-up. While trace background vacuum impurities undergo secondary radiolytic processing to yield a variety of minor organic features (such as formaldehyde and formic acid networks), they remain minor sub-monolayer components. The thermal and structural evolution of the system remains fundamentally governed by the robust chemical interaction, hydration profiling, and defect-trapping mechanisms operating at the Na_3PO_4 interface.

5.5.4 Radiolytic processing and kinetic evolution of mixed H_2O:CO ices on Na_3PO_4 substrates

The co-condensation of a three-to-one H_2O:CO ice mixture was performed at 12 K over a coupled CaF_2 + Na_3PO_4 substrate. This low-temperature deposition process yields a highly porous, amorphous ice matrix.The disordered, porous nature of the initial framework is spectroscopically verified by the distinct presence of a water absorption feature at 3639 cm^{-1}, which corresponds directly to the dangling O−H bonds of water molecules localized along the internal pore surfaces. Immediately following deposition, the primary precursor vibrations are clearly established, featuring dominant H_2O ice matrix bands at 3264 cm^{-1} and 1653 cm^{-1}, alongside

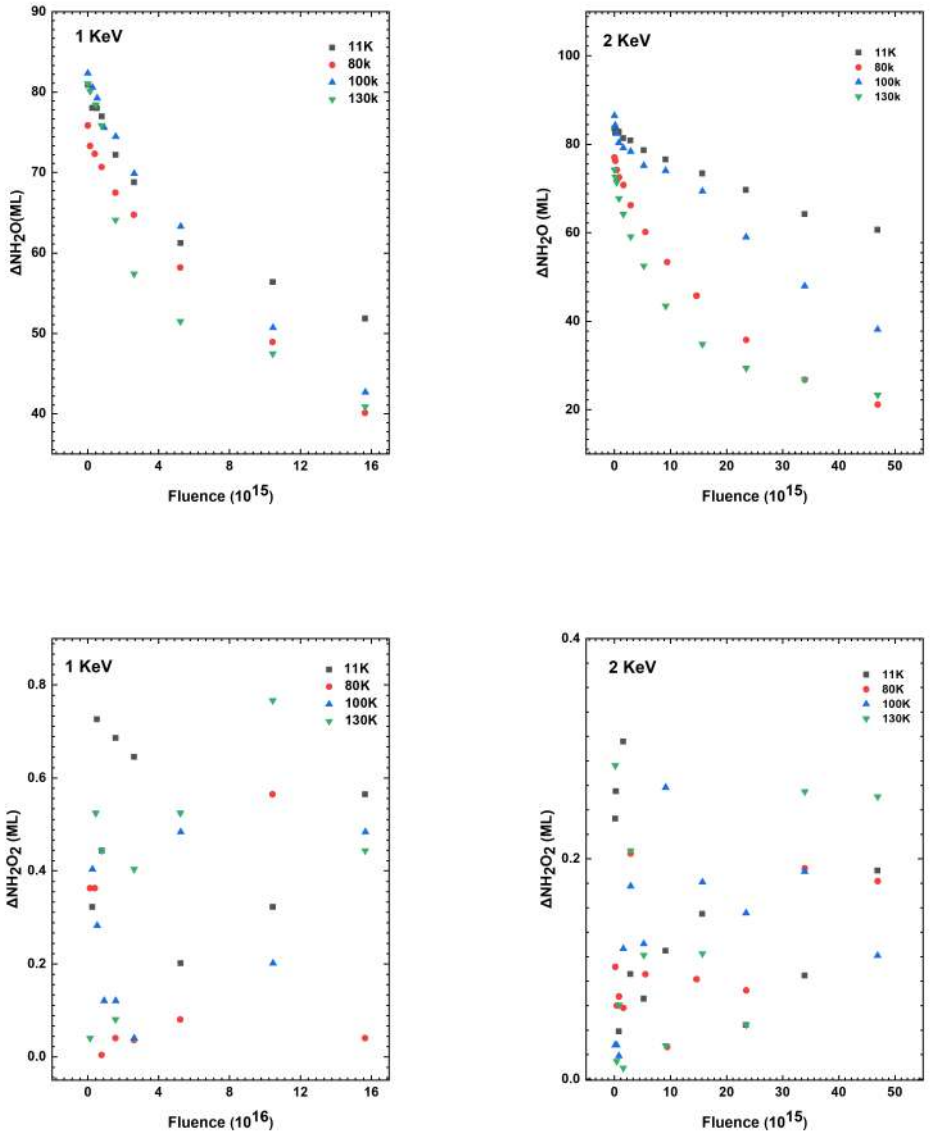

Figure 5.9: Radiolytic column density evolution of H_2O, and H_2O_2 under 1 KeV (1 hour) and 2 KeV (3 hour) electron irradiation

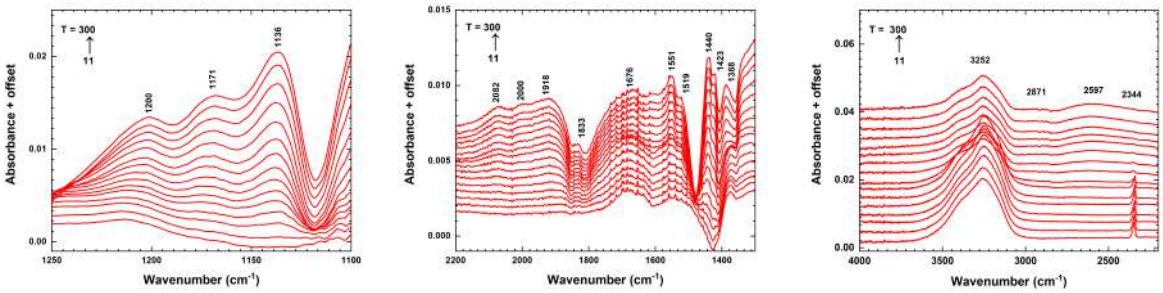

Figure 5.10: Temperature-dependent FTIR spectra captured during the systematic TPD warm-up (11 K to 300 K at 2 K/min) of H_2O ice overlayers on Na_3PO_4 substrates following 1 keV and 2 keV electron irradiation. Labels indicates band locations (their assignemnts is in Table 5.4).

Table 5.4: FTIR features measured during the warming up of H_2O ice after 1 keV and 2 keV irradiation.

wavenumber (cm^{-1})	chemical assignment	vibrational mode, structural attribution
1136	HPO_4^{2-} / HCOOH	ν_3 asymmetric P−O stretch (protonated orthophosphate)
1171	HCOOH / P=O	P=O stretching mode (shifted via localized hydrogen-bonding)
1200	H_2CO / HCOOH / O−P−O	Symmetric O−P−O stretch (condensed metaphosphate framework)
1374 / 1382	$HCOO^-$ / P−OH / P=O	Superposition of fundamental P−OH stretch and localized formate anions
1388	H_2O_2	Asymmetric bending vibration
1423	H_2CO	Formaldehyde matrix network deformation
1440	H_2CO	Formaldehyde matrix network deformation
1519	H_2CO	Formaldehyde matrix network deformation
1551	O_2	Defect-activated molecular oxygen (deeply trapped at interface)
1676	HCOOH	Neutral formic acid network stretching vibration
1833	·HCO / HOCO /H_2CO	C=O stretch / hydroperoxyl radicals
1918	—	Residual unassigned matrix mode
2000	—	Residual unassigned matrix mode
2082	—	Residual unassigned matrix mode
2344	CO_2	Discrete trace carbon dioxide background contaminant
2597	—	Residual unassigned matrix mode
2871	H_2O_2	O−H stretching mode (thermally annealed crystalline cages)
3251	H_2O	Bulk and interfacial water ice O−H stretching envelope

the sharp, characteristic CO stretching mode at 2138 cm^{-1} (Figure 5.11). The evolution of these coupled matrices was monitored via infrared spectroscopy across three distinct experimental benchmarks: prior to irradiation, continuously throughout the electron bombardment phase, and during the subsequent thermal annealing and sublimation sequence.

To evaluate the radiolytic transformation of the ice-salt interface, the samples were subjected to energetic processing using either 1 keV or 2 keV electron beams. The incoming electrons interact with the parent H_2O and CO molecules through a combination of impact ionization, discrete electronic excitations to higher energy states, and resonance electron attachment pathways that generate short-lived transient negative ions. This energetic processing drives the steady depletion of the parent species and fuels the synthesis of structurally diverse radiolytic products. Interestingly, while the initial abundance of carbon monoxide is three times lower than that of water, both precursor molecules exhibit remarkably similar absolute depletion volumes, indicating highly efficient processing of the carbonaceous volatile fraction. Figure 5.12 shows the spectra of the irradiated ice with 1 keV and 2 keV electrons. The main band positions and their spectroscopic assignments are reported in Table 5.5.

Table 5.5: Infrared wavenumber assignments and molecular products identified in mixed H_2O:CO ices overlying Na_3PO_4 after 1 keV and 2 keV electron irradiation.

1 keV (cm^{-1})	2 keV (cm^{-1})	chemical assignment, vibrational mode attribution
986	986	O−P−O framework stretching mode (substrate residue)
1096	—	$(CH_2OH)_2$ / CH_3OCH_3 / CH_3CH_2OH / ·HCO / Asymmetric P−O_3 stretch
1148	—	HPO_4^{2-} (altered substrate) / CH_3OH product overlap
1206	—	Residual unassigned matrix mode
—	1215	HCOOH altered framework vibration
1244	—	H_2CO / HCOOH complex structural blend
1267	—	Residual unassigned matrix mode
1305	1305	CH_4 deformation mode product
1378	1378	$HCOO^-$ (formate anion) secondary ionization signature
1498	1498	H_2CO (formaldehyde) primary matrix feature
1556	—	Defect-activated molecular species / interfacial trapping mode
—	1635	HCOOH network stabilization mode
1653	—	H_2O ice bending fundamental mode
1673	1676	HCOOH multi-molecular hydrogen-bonded network stretch
1716	1716	H_2CO / HCOOH / H_2CO_3 (carbonic acid) blended carbonyl envelope
1848	1848	C=O stretch of transient ·HCO / HOCO radical complexes
2138	2138	CO stretching fundamental mode (precursor matrix)
2277	2277	$^{13}CO_2$ minor radiolytic isotopologue product
2341	2341	CO_2 principal radiolytic byproduct stretching vibration
2576	2576	HCOOH unambiguous chemical network identifier
2730	—	HCOOH secondary matrix configuration stretch
—	2837	H_2O_2 matrix-trapped radiolytic product
3264	3256	H_2O bulk stretching envelope (amorphous vs compacted matrix)
3639	3639	O−H dangling molecules (surface states within ice pores)
3703	—	CO_2 matrix combination / combination band

Consistent with comparable laboratory simulations utilizing electron, proton, ultraviolet, and X-ray processing, carbon dioxide is the dominant radiolytic product with an absorption feature at 2341 cm^{-1} alongside a minor isotopic $^{13}CO_2$ band at 2277 cm^{-1}. Concurrently, an array of secondary reaction pathways unfolds within the ice matrix. The formyl radical (·HCO)

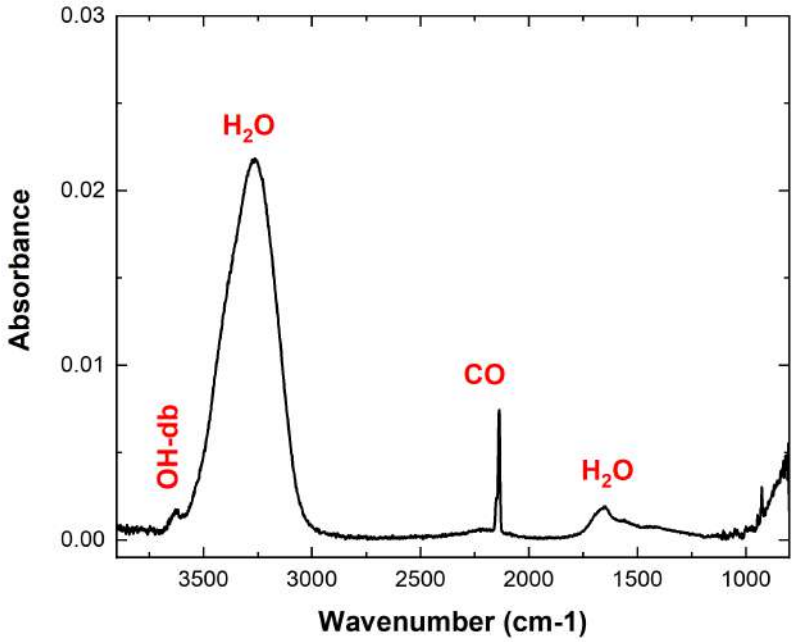

Figure 5.11: Infrared spectra of the unirradiated H_2O:CO ice mixture at 12 K.

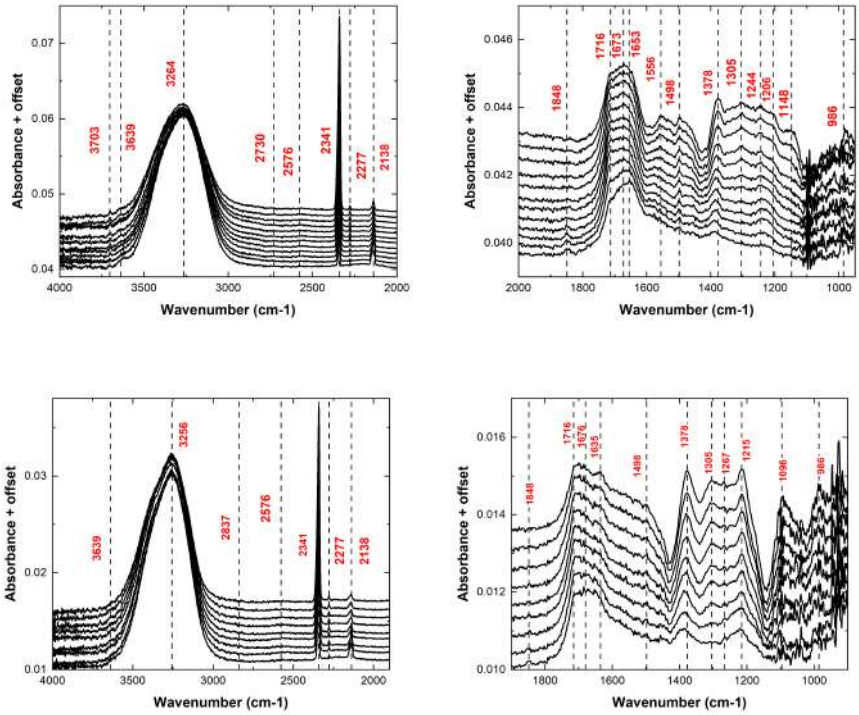

Figure 5.12: FTIR difference spectra of the Na_3PO_4+H_2O:CO matrix taken at progressive intervals during 1 keV electron irradiation at 12 K (both top panels) and during 2 keV electron irradiation at 12 K (both bottom panels). Traces are arranged chronologically from bottom to top, corresponding to exposure times of 15, 30, 60, 90, 120, 180, 240, 360, 540, 900, 1800, 2700, and 3600 seconds. Spectral profiles are plotted as a function of wavenumber (cm^{-1}) after subtracting the initial, unirradiated ice spectrum from each subsequent trace.

is successfully identified via its vibration at 1848 cm^{-1} following both 1 keV and 2 keV exposure. Under 1 keV electron irradiation, this radical feature becomes less prominent and undergoes a noticeable red-shift as the electron fluence increases, whereas under the higher energy 2 keV flux, the band is nearly completely destroyed after 60 minutes of exposure, demonstrating the rapid destruction of transient species under high-energy processing. This 1848 cm^{-1} feature also contains overlapping contributions from the hydrocarboxyl radical HOCO. Formaldehyde H_2CO formation is verified by a primary band at 1498 cm^{-1}, with complementary modes appearing at 1716 cm^{-1} (blended with carbonic acid, H_2CO_3) and 1244 cm^{-1} (overlapping with formic acid, HCOOH). The synthesis of neutral formic acid is unambiguously confirmed by its twin infrared signatures at 2730 and 2576 cm^{-1}, alongside associated bands at 1673 and 1215 cm^{-1}, while its ionized counterpart, the formate anion $HCOO^-$, is detected at 1378 cm^{-1}. Additionally, methane CH_4 accumulation is marked by a feature at 1305 cm^{-1}.

The underlying sodium orthophosphate substrate participates directly in this radiation-driven chemistry, yielding distinct spectroscopic signatures that would be completely absent in an ice mixture processed on an inert substrate. In the 1 keV electron irradiation experiments, a distinct peak emerges and steadily grows at 1148 cm^{-1}, providing a signature of direct chemical cross-talk at the interface. This feature represents the efficient protonation of the salt matrix into stable HPO_4^{2-}, driven by the substrate actively capturing mobile H^+ or ·H fragments generated from the radiolysis of the overlying water ice. This region also contains an overlapping contribution from synthesized methanol CH_3OH near 1133 cm^{-1}; interestingly, this combined $1148 - 1133$ cm^{-1} feature is notably absent in the 2 keV irradiation trials. Nearby, the spectral region around 1096 cm^{-1} exhibits a low signal-to-noise ratio, reflecting a complex, multi-component profile that represents a superposition of ethylene glycol $(CH_2OH)_2$, dimethyl ether CH_3OCH_3, ethanol CH_3CH_2OH, secondary ·HCO radical modes, and the asymmetric $P-O_3$ stretch of the underlying salt. Meanwhile, a minor hydrogen peroxide band is resolvable at 2837 cm^{-1} under 2 keV conditions. The structural persistence of the substrate throughout the bombardment is tracked by a stable peak at 986 cm^{-1}, which corresponds directly to the internal framework stretching modes of the substrate's $O-P-O$ groups. The ionic nature of this Na_3PO_4 substrate fundamentally alters the local matrix environment and the subsequent thermal evolution of the system. While volatile radiolytic products and water ice would normally sublimate entirely from an inert substrate below 160 K, the powerful electrostatic field and ion-dipole interactions originating from the surface Na^+ cations secure a robust, thin-film hydration network at the interface. This stabilizing mechanism prevents molecular escape into the vacuum, allowing tightly bound hydration water, surface hydroxyl groups, and heavily shifted organic networks, such as the formaldehyde matrix components, to survive at elevated temperatures up to 300 K. The column density evolution for the major species is shown in Figure 5.13.

Evolutionary trends in the molecular column densities reveals distinct kinetic trends between the 1 keV and 2 keV processing regimes. As expected, the parent H_2O and CO profiles exhibit steady depletion as a function of electron fluence. This depletion trend is initially steep at low fluences but transitions to a significantly slower rate at higher fluences, indicating the presence of a residual ice fraction that is structurally resistant to further radiolysis, stabilized by the strong electrostatic anchoring to the Na_3PO_4 substrate and radiation-induced ice compaction. At all recorded fluences, the 2 keV electron beam induces a more pronounced drop in water column density compared to the 1 keV trials, confirming a higher overall processing efficiency at higher projectile energies. The CO_2 column density rises rapidly during the early stages of exposure before exhibiting a classic saturation plateau at elevated fluences, followed eventually by slow radiolytic destruction that proceeds much faster under the higher energy 2 keV flux. Finally, the transient formyl radical ·HCO acts as a critical kinetic intermediate. It forms rapidly at very low electron fluences, quickly reaching a localized maximum abundance; as the electron fluence continues to accumulate, its column density steadily drops as it is efficiently consumed and converted into more complex, stable daughter species like formaldehyde and formic acid, or directly destroyed by the ongoing electron cascade. Consistent with the global energetics of the system, the higher 2 keV electron energy yields a significantly larger maximum abundance of the formyl radical, directly reflecting the enhanced radical production efficiency of the higher energy electron beam.

Following the low-temperature electron bombardment phase, the interstellar ice analogs were subjected to TPD, ramping from 12 K to 300 K at a linear rate of 2 K per min. This thermal

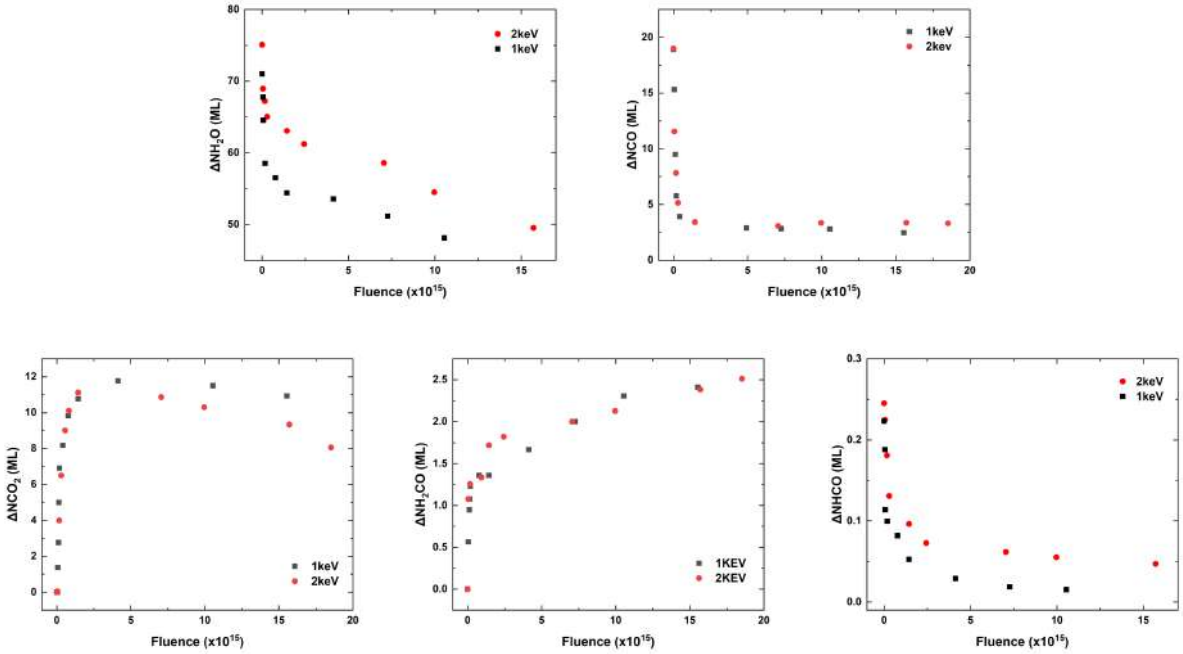

Figure 5.13: Column density evolution of precursor molecules H_2O and CO, and synthesized radiolysis products, CO_2, H_2CO and ·HCO. plotted against electron fluence for 1 keV and 2 keV irradiation regimes.

processing phase drives structural phase transitions, matrix reorganization, and molecular sublimation events that are dramatically regulated by the underlying ionic sodium orthophosphate substrate. The primary spectroscopic assignments tracked across the 1 keV and 2 keV processing runs during this thermal profile are listed to understand both desorption and conversion pathways of precursors and synthesized radiolytic daughter products (see Table 5.6). As the temperature increases progressively, the infrared spectral footprints shift dynamically, revealing how tightly the volatile phase interacts with the salt core. Temperature-resolved infrared spectra evolution during the warm-up are show in Figure 5.14.

The primary volatile carbon monoxide precursor stretching mode at 2138 cm^{-1} shows an interesting thermal dynamics, persisting well past its typical sublimation threshold of approximately 30 K due to direct coordination with hydrated phosphate sites. Concurrently, while bulk water ice undergoes a distinct sublimation event near 160 K, the broad, primary O – H stretching envelope (centered at 3264 cm^{-1} for 1 keV and 3254 cm^{-1} for 2 keV) remains unattenuated all the way up to 300 K. This remarkable room temperature survival provides definitive evidence

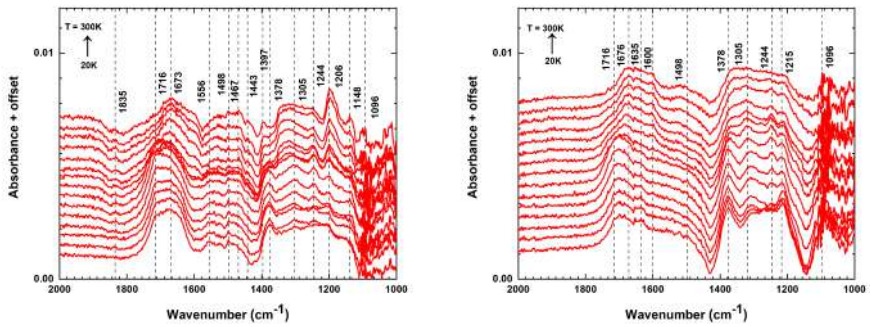

Figure 5.14: FTIR spectral evolution (2000 – 1000 cm^{-1}) of electron-irradiated H_2O:CO ice during annealing from 20 to 300 K at 20 K intervals. The left and right panels correspond to processing under 1 keV and 2 keV electron bombardment, respectively.

Table 5.6: Infrared band assignments and observed wavenumbers (cm^{-1}) for the H_2O:CO mixture during the warm-up phase.

1 keV (cm^{-1})	2 keV (cm^{-1})	molecular assignment
1019	—	CH_3OH
1096	—	$(CH_2OH)_2$, CH_3OCH_3, CH_3CH_2OH
1138	—	CH_3OH
1199	—	?
1217	—	?
1245	1246	H_2CO, HCOOH
1305	1305	CH_4
1319	—	?
1377	1375	$HCOO^-$
1397	—	HCOOH, CH_3CH_2OH
1442	—	?
1467	—	?
1498	—	HCOOH
1510	—	?
1545	—	O_2
1600, 1636	—	HCOOH
1666	1672	HCOOH
1700	1701	HCOOH
1835	—	HCO
2138	2138	CO
2277	2277	$^{13}CO_2$
2341	2341	CO_2
3264	3254	H_2O

that a robust fraction of water remains chemically bound as an interfacial hydration layer to the polar Na_3PO_4 surface rather than evaporating as free ice. The major radiolytic products exhibit clear structural modifications inside the relaxing matrix during heating. The principal carbon dioxide feature at 2341 cm^{-1}, along with its asymmetric isotopic $^{13}CO_2$ counterpart at 2277 cm^{-1}, sharpen considerably upon warming, reflecting thermal segregation and structural stabilization as the molecules migrate and nest directly over the surface Na^+ cation sites. Similarly, methane, identified via its 1305 cm^{-1} band, shows an initial increase in intensity and sharpening at lower temperatures. This trend corresponds to the structural relaxation and partial crystallization of the surrounding water ice cage, which generates a more homogeneous local environment for the trapped methane before the bulk sublimation of the water ice matrix past 160 K releases these crystalline cages and causes a rapid decrease in the 1305 cm^{-1} band as the liberated methane desorbs into the vacuum. In the 1 keV electron irradiation profile, the formyl radical reappears during the warm-up sequence at a red-shifted position of 1835 cm^{-1} and survives up to 300 K. This behavior reflects a change in the local chemical environment; as the bulk ice collapses and sublimates, the ·HCO radical is driven to the ice-substrate boundary. Here, the electrostatic fields of the Na_3PO_4 surface and reduced hydrogen-bonding constraints modify its vibrational frequency, trapping the radical and inhibiting both its thermal desorption and its recombination. A parallel trapping mechanism is observed for molecular oxygen that has been detected at 1545 cm^{-1} during the 1 keV warm-up and persists up to 300 K. These profiles demonstrate that electron processing followed by controlled thermal annealing can simultaneously suppress and subsequently regenerate reactive radicals, proving that their high-temperature survival is a product of deep surface trapping rather than preservation within bulk ice. Simultaneously, complex organic products show varying degrees of volatility and chemical conversion. Formaldehyde bands at 1498, 1245, and 1700 cm^{-1} drop significantly in intensity during warming, yet trace residual quantities remain anchored to the salt surface at 300 K. Methanol features at 1138 and 1019 cm^{-1} (evident in the 1 keV experiment) become clearer and more pronounced upon warming due to the clearing away of overlapping bulk ice bands. The presence of complex fragments like ethylene glycol, dimethyl ether, and ethanol is suggested via the multi-component profile at 1096 cm^{-1}. Most notably, the weak, neutral formic acid signatures at 2576 and 2730 cm^{-1} completely disappear during heating, while the formate ion $HCOO^-$ absorption band at 1377 cm^{-1} blue-shifts to 1397 cm^{-1} upon heating. This spectral evolution demonstrates that as the matrix warms, synthesized formic acid loses its hydrogen protons (deprotonates) to the substrate. The resulting negative formate ions then lock tightly onto the positive sodium sites of the Na_3PO_4 surface, forming highly stable surface salts that resist evaporation up to 300 K.

Comparing these findings to the thermal warm-up phase of pure water ice exposed to identical electron irradiation reveals several profound differences in both the reaction pathways

Table 5.7: Comprehensive experimental matrix for the comparative irradiation of ice-substrate systems.

experiment	substrate	ice	ice thickness (ML)	irradiation time (min)	temperature (K)
1	MgF_2	H_2O	100	210	10
2	MgF_2	H_2O	100	210	80
3	MgF_2	H_2O	100	210	100
4	MgF_2	H_2O	100	210	130
5	MgF_2	H_2O,CO	100	210	10
6[1]	MgF_2 + Na_3PO_4	—	—	—	10
7	MgF_2 + Na_3PO_4	—	—	210	10
8	MgF_2 + Na_3PO_4	H_2O	100	210	10
9	MgF_2 + Na_3PO_4	H_2O	100	210	80
10	MgF_2 + Na_3PO_4	H_2O	100	210	100
11	MgF_2 + Na_3PO_4	H_2O	100	210	130
12	MgF_2 + Na_3PO_4	H_2O,CO	100	210	10

and the resulting interfacial properties. In the pure H_2O ice experiment, the lack of an abundant carbon source prevents the synthesis of formyl ·HCO or hydroperoxyl HOCO radicals, meaning that the radical chemistry is dominated almost exclusively by ·OH and ·H fragments which primarily recombine into hydrogen peroxide or escape. In contrast, introducing carbon monoxide opens up a dominant radical-trapping network. This mechanism successfully drives the formation of various stable organic derivatives whose thermal desorption is suppressed by strong anchoring to the Na_3PO_4 substrate, allowing them to persist at room temperature. Furthermore, while the experiments with pure water ice show a simple, isolated reaction where water fragments merely transfer protons to turn the substrate into HPO_4^{2-} at 1148 cm^{-1}, the addition of CO completely transforms this interfacial chemistry. The introduced carbon source might trigger a complex cascade of reactions, building a crowded boundary zone where newly synthesized organic products and the inorganic salt substrate blend together. This direct chemical cross-talk is proven by the prominent shifting of the formate band 1377 → 1397 cm^{-1}, which tracks the organic molecules losing their protons and anchoring directly to the surface sodium sites as a stable salt layer. Consequently, heavy synthesized molecules like methanol, formaldehyde, ethylene glycol, and dimethyl ether do not freely evaporate at their expected volatility thresholds; instead, they are held tightly by the substrate's powerful electrostatic forces, clustering together directly at the interface up to room temperature.

5.5.5 Comparative electron and X-ray radiolysis of interfacial ices on Na_3PO_4 substrates and their thermal evolution

To evaluate the specific role of photon-mediated processing, the experimental focus was shifted to X-ray irradiation utilizing LIFE in Palermo. Transitioning from electron bombardment to an X-ray source fundamentally alters the energy deposition mechanism within the ice-substrate matrix. While high-energy electrons induce direct kinetic ionization along their track, X-ray photons interact primarily through the photoelectric effect, generating a widespread cascade of low-energy secondary electrons. The comprehensive matrix of these experiments, including ice compositions and deposition temperatures, is systematically cataloged in Table 5.7. or these photon-processing runs, X-rays were generated using a SPECS XR 50 NAP dual-anode source (see Section 2.3.2) mounted on the chamber flange and aligned directly toward the sample holder at a nominal working distance of 20 mm. Accelerated under an electric field of up to 15 kV, electrons hit the aluminum-coated anode face to generate the characteristic Al Kα emission line at 1486.6 eV. At the target surface, the source delivers a calibrated photon flux of 5.1×1010 photons s^{-1} across a beam spot size of $s_X \approx 80$ mm, safely larger than the FTIR spectrometer's infrared probing beam (see Section 2.2), so that the spectrometer exclusively samples ice that has been uniformly processed by the X-ray flux.

Before exposure, the baseline infrared signature of the pristine, unirradiated salt is captured in Figure 5.15. When applied to the bare Na_3PO_4 substrate at 10 K, X-ray exposure drives local lattice distortion and lowers the site symmetry of the phosphate tetrahedra. This environment lifts their vibrational degeneracy and splits the asymmetric P–O stretching mode into distinct components at 1099, 1138, 1160, 1191, and 1217 cm^{-1}. Unlike the more destructive electron beams delivered by the electron gun at the IEPS facility, which operates at a higher particle flux density of 3.2×10^{11} electrons cm^{-2} s^{-1} over a 2 cm^2, spot, the X-rays

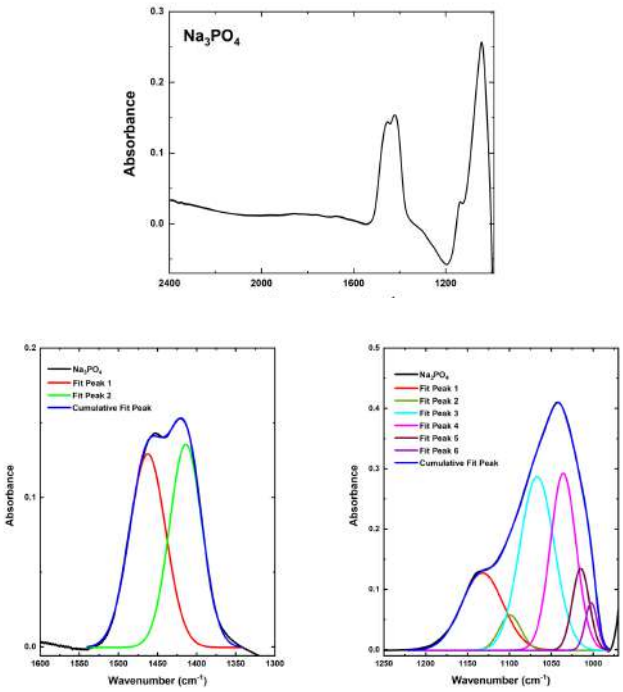

Figure 5.15: Top panel: FTIR absorbance spectrum of the pristine Na_3PO_4 substrate at 10 K before irradiation; bottom panels: Gaussian decomposition of the two main features.

do not degrade the core orthophosphate structure. Instead, X-rays selectively alter the surface chemistry by destroying pre-adsorbed atmospheric carbonate contaminants. As monitored in the sequential spectral profiles of Figure 5.16, this photon-induced depletion is marked by a prominent negative absorbance feature centered at 1430 cm^{-1} (due to the subtraction from the blank spectrum without irradiation, experiment 6). Because this specific band is diagnostic of the ν_3 asymmetric stretching vibration of the carbonate CO_3^{2-} ion, its systematic inversion below the baseline confirms the continuous, radiation-driven destruction of the ambient sodium carbonate crust that naturally encapsulates the highly alkaline Na_3PO_4 matrix during open-air preparation. Under the continuous Al Kα X-ray flux, these surface-bound carbonate impurities are radiolytically cleaved, driving the carbon atoms down two distinct chemical pathways. The first pathway involves the direct fragmentation and ultimate desorption of volatile carbon oxides into the ultra-high vacuum environment, effectively clearing them from the analytical footprint. Simultaneously, the remaining fragments undergo a proton-assisted chemical migration, trapping liberated carbon species into an alternative, stable interfacial sink. This secondary pathway is confirmed by the simultaneous growth of a positive absorption complex between 1675 and 1684 cm^{-1}. While this spectral region exhibits some overlap with the characteristic ν_2 bending mode of residual or amorphous matrix water, its distinct morphology and coupled growth kinetics reveal the formation of stable bicarbonate intermediates and synthesized carbonic acid networks, which remain anchored to the substrate boundary. Consequently, the localized inversion of the 1430 cm^{-1} profile does not indicate an experimental artifact or uncompensated baseline drift, but rather provides definitive spectroscopic evidence of a photon-mediated surface-cleaning mechanism, wherein the X-ray flux systematically strips ambient carbonaceous contaminants from the mineral interface and locks the residues into a stable, protonated acidic matrix.

When the salt is capped with a 100 ML ice layer, either pure H_2O or a 3:1 H_2O:CO mixture, this X-ray-induced interfacial chemistry becomes significantly more pronounced. The water layer acts as an active chemical mediator; photon radiolysis of the ice generates a rich flux of protons, hydrogen atoms, and hydroxyl radicals that readily migrate to the salt boundary. This drives a highly efficient, proton-assisted restructuring of the substrate interface, converting the surface layers into a complex network of distorted hydrogen phosphate HPO_4^{2-} and $H_2PO_4^-$ units. As visualized across the different temperature and time regimes in Figure 5.17, the

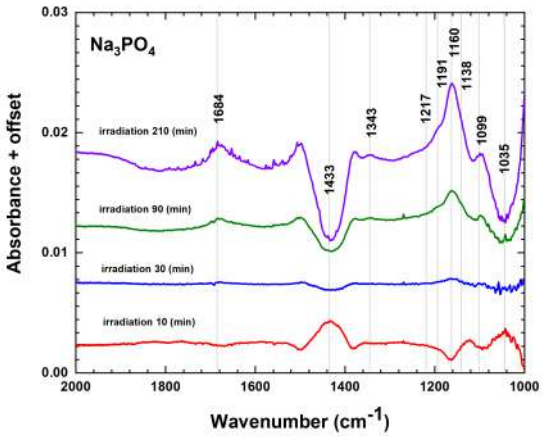

Figure 5.16: FTIR absorbance spectrum of the bare Na_3PO_4 substrate at 10 K taken at different times during the irradiation.

Table 5.8: Quantitative transport and energy deposition parameters for electron and X-ray radiolysis.

radiation source	primary energy	flux density	range in ice	range in Na_3PO_4
	keV	particles cm^{-2} s^{-1}	nm ($\rho \approx 0.93$ g/cm^3)	nm ($\rho \approx 2.5$ g/cm^3)
electron gun (IEPS)	1.0	3.20×10^{11}	$\approx 30 - 40$	stopped within the ice
electron gun (IEPS)	2.0	3.20×10^{11}	> 50	$\approx 30 - 40$
X-ray source (LIFE)	1.486	5.13×10^{10}	> 50	$\approx 800 - 1100$

efficiency of this X-ray-mediated pathway is strictly regulated by the initial ice deposition temperature, showing a distinct behavior compared to electron-irradiated samples. At 10 K, the rigid, amorphous ice matrix locks the radiolytic fragments in place, maximizing spectral complexity and structural trapping at the interface. As the deposition temperature is raised through 80 K, 100 K, and up to 130 K, the increased thermal mobility permits the partial recombination of radical intermediates and drives the structural relaxation of the ice cages. Consequently, the higher temperature X-ray runs exhibit smoother, cleaner spectral profiles where volatile products desorb, ultimately leaving behind an annealed, exceptionally stable, and well-ordered protonated phosphate layer anchored firmly to the substrate.

5.5.6 Why X-rays exhibit reduced localized chemical efficiency compared to electron bombardment

To interpret the observed variations in interfacial chemistry, the distinct spatial profiles of energy deposition across the different irradiation configurations must be quantified. Because the characteristic photon energy of the X-ray source (1.486 keV) sits precisely between the two selected electron kinetic energies (1.0 keV and 2.0 keV), individual particle energy is effectively held constant as an experimental variable. Consequently, the stark divergence in radiolytic efficiency must be rationalized primarily through the differences in raw particle flux density and the particle-dependent penetration depth within the target matrix.

On a purely collisional basis, the particle delivery rates vary significantly between the two architectures. The electron gun delivers a sustained flux density of 3.2×10^{11} electrons cm^{-2} s^{-1} to the target surface. In contrast, the X-ray source delivers an absolute output of 5.3×10^{10} photons cm^{-2} s^{-1}. Therefore, the electron beam impacts the ice mantle with roughly 6.2 times more particles per second per square centimeter than the X-ray source. When evaluating the total energetic payload delivered to the sample surface over identical 210-minute exposure intervals, the electron gun deposits roughly six times more raw kinetic energy per unit area than the photon flux. The definitive driver of the chemical divergence, however, is the pervasiveness of the photon flux compared to the highly localized stopping power of the electron beam. This fundamental physical contrast is quantified in Table 5.8, which outlines the ballistic parameters and spatial distribution of energy within the respective target matrices.

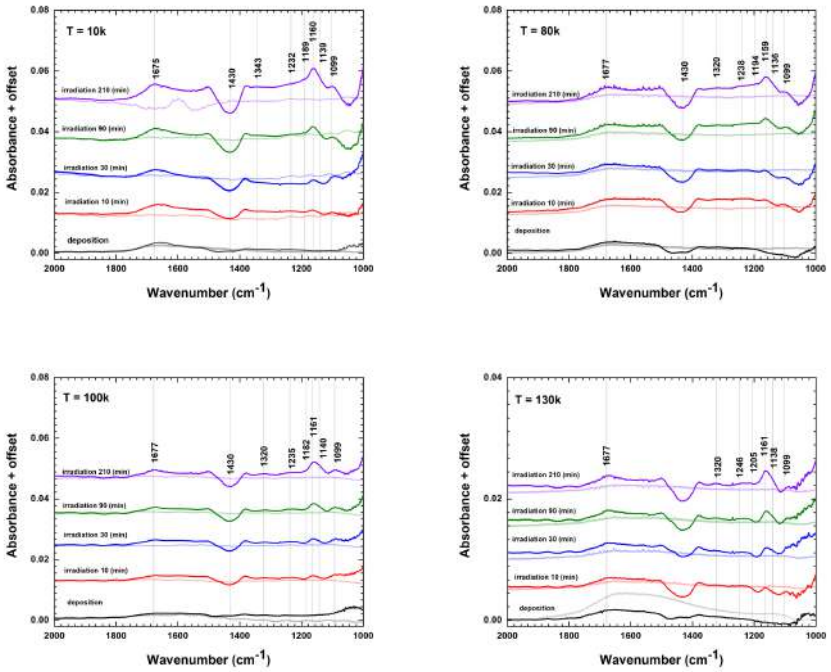

Figure 5.17: FTIR absorbance spectra of a 100 ML H_2O ice mantle deposited on the Na_3PO_4 substrate, recorded at progressive irradiation intervals (10, 30, 90, and 210 minutes). The panels track the structural and chemical evolution of the system across four distinct deposition temperature regimes: 10 K, 80 K, 100 K, and 130 K.

As demonstrated by these values, kinetic electrons lose energy aggressively via continuous, localized Coulomb scattering off the electronic clouds of the target atoms. Within the low-density amorphous water ice mantle, a 1.0 keV electron possesses a maximum penetration range that matches the physical thickness of the one hundred monolayer ice mantle, dumping 100% of its energy directly inside the ice layer. When the electron energy is increased to 2.0 keV, the electrons penetrate through the 30 nm ice film and enter the dense trisodium phosphate substrate. Due to the high density of the salt matrix, these 2.0 keV electrons are brought to a violent, abrupt halt within a shallow, ultra-thin sub-surface pocket spanning just ~ 5 to 35 nm below the chemical interface. Conversely, X-ray photons are fundamentally more pervasive, traveling through matter unimpeded until a discrete photoelectric absorption event occurs. Because the attenuation coefficient of a 1.486 keV photon in light-element matrices is remarkably low, the thin 30 nm water ice layer is practically invisible to the X-ray flux. Upon crossing the interface into the dense salt substrate, the characteristic attenuation length of these photons extends to a depth between 800 and 1100 nm. This means that while the 2.0 keV electron beam compresses its remaining energy into a microscopic 30 nm interfacial zone, the pervasive X-ray photons dilute their energy across a vast, three-dimensional bulk column that is nearly thirty times deeper.

This pronounced spatial volume-averaging directly accounts for the significantly lower radiolytic efficiency observed during X-ray processing. A comparison of the respective penetration depths reveals that the local energy density, the energy deposited per unit volume, delivered by the electron beam at the immediate interface is roughly two orders of magnitude greater than that of the X-ray flux. Consequently, when a deeply penetrating X-ray photon ionizes a phosphate tetrahedron within the bulk substrate, the surrounding rigid crystal lattice acts as a physical cage. Lacking both reactive chemical partners and the spatial freedom to escape, the shattered molecular fragments undergo rapid geminate recombination, effectively self-healing back into stable trisodium phosphate. Permanent, irreversible chemistry is therefore structurally restricted to the two-dimensional ice-substrate interface. At this boundary, mobile radiolytic protons generated within the overlying ice column can readily migrate to cap open, under-coordinated oxygen sites on the radiation-perturbed surface salt molecules. Ultimately,

because the infrared spectrometer integrates the entire vertical profile of the film, it records two entirely different chemical regimes: a chaotic, high-density molecular rearrangement in the electron-irradiated datasets due to the extreme local energy dump, contrasted against a clean, highly selective, and strictly localized surface-protonation sequence in the deeply pervasive, lower-density X-ray datasets.

5.6 Conclusions and future developments

The experimental investigation in this work established a foundation for understanding the non-thermal, radiation-driven alteration of sodium orthophosphate substrates under simulation conditions resembling the harsh, cryogenic environments of Saturn's icy moons. By exposing pristine sodium orthophosphate to localized $1 - 2$ keV electron bombardment and soft X-ray irradiation beneath layers of pure and mixed carbon monoxide–water ices, this phase of the research tracked the active role of the substrate in surface chemistry. Rather than acting as an inert support, sodium orthophosphate directly interacted with mobile radiolytic fragments generated in the volatile ice overlayers. This chemical exchange promoted the efficient synthesis of simple organic molecules, including formaldehyde, formyl radicals, and formic acid, while simultaneously modifying the underlying substrate into protonated phosphate phases. In addition, strong ion–dipole interactions between surface sodium cations and the surrounding volatiles helped stabilize an electrostatically bound hydration network, slowing the sublimation of water and newly formed organic molecules and allowing them to persist at temperatures well above typical vacuum desorption thresholds.

Despite these useful empirical insights, the structural yields also reveal an intrinsic limitation in the energetic efficiency of the radiation sources employed. Although electron processing and soft X-rays altered the near-surface region and induced partial protonation to form monohydrogen phosphate species, they were not energetic enough to overcome the strong thermodynamic stability of the orthophosphate anion. The high lattice energy and chemical robustness of the orthophosphate structure remained largely intact under these conditions, with the main effects confined to shallow amorphization and surface protonation rather than deeper disruption of the phosphorus–oxygen framework. As a result, direct non-thermal synthesis of covalent organophosphorus linkages, such as sugar phosphates or nucleotide-like frameworks, was not observed. This points to a central bottleneck: low-energy surface processing alone cannot easily overcome the inertia of pristine sodium orthophosphate to drive primordial biochemical synthesis. To address this limitation, the next stage of the research will focus on understanding how sodium orthophosphate itself can be fragmented under more extreme irradiation conditions. Future experiments will therefore employ higher-energy X-rays, specifically exploiting the advanced capabilities of the Taiwan Photon Source (TPS) synchrotron, together with substantially thicker phosphate samples in order to probe deeper energy deposition regimes and investigate whether the orthophosphate lattice can be efficiently disrupted. The objective is to identify the nature of the phosphorus-bearing fragments produced during irradiation and determine whether reactive intermediates, potentially capable of participating in subsequent prebiotic chemistry, can be generated directly from Na_3PO_4. Establishing the fragmentation pathways of orthophosphate under intense irradiation conditions will provide the necessary basis for a second experimental phase aimed at exploring the chemistry of activated phosphorus species in more complex cryogenic organic environments.

By first identifying the reactive phosphorus fragments that can emerge from irradiated orthophosphate, subsequent experiments will be able to investigate their interaction with increasingly complex organic reactants, including ribose, simple amino acids, and nitrogenous bases, thereby exploring possible pathways toward phosphorus-bearing prebiotic molecular networks. A key horizon of this continuous research line involves investigating the mechanisms required to synthesize primordial energy-currency analogs. If mechanical and electronic disruptions within the phosphate network successfully yield condensed or activated phosphorus compounds, such as pyrophosphates or highly reactive polyphosphates, it becomes plausible to explore the direct condensation of these fragments with adenosine precursors. Overcoming the thermodynamic barriers of orthophosphate decomposition opens a possible chemical pathways leading to the formaton of adenosine triphosphate (ATP) precursors. By evaluating how these radiation-activated fragments assemble alongside nitrogenous bases and sugar structures, the upcoming phase of this project will directly assess the feasibility of generating the foundational bio-energetic units necessary to power emergent metabolic networks on icy celestial bodies.

6. The prebiotic thread: from cosmic ices to the foundations of astrobiology

The structural, chemical, and energetic investigation of astrophysical ices presented in this thesis addresses a diverse framework of technical questions. Throughout the preceding chapters, our narrative has been anchored in the rigorous discipline of laboratory astrochemistry and molecular spectroscopy. We have navigated the highly specialized regimes of ultra-high vacuum technology, decrypted the complex morphology of thin ice films via Fourier-transform infrared spectroscopy, and quantified the physical chemistry governing gas-grain interactions. We explored how the narrow infrared profiles of carbon monoxide can serve as a sensitive remote proxy for structural stratification in protoplanetary discs or molecular clouds. We examined the subtle shifts in absorption bands that occur when volatile molecules are locked within polar or apolar matrices. Furthermore, we extended this analytical framework to planetary scales, analyzing the radiolytic activation of inorganic salts beneath water-ice overlayers to map the potential geochemical fate of phosphorus on the ocean worlds of the outer solar system.

Yet, behind every single experiment or calculation, lies an implicit, unifying aim. The underlying architecture of this research, and indeed, of astrochemistry as a whole, is driven by a profound and ultimate human question: *how does life emerge from the inanimate matter of the universe?* Every specialized thermodynamic, physical, or optical mechanism exploited in this work does not exist in isolation. Instead, each represents a distinct thread in a singular prebiotic tapestry, tracing the historical and chemical continuum that connects the dark, dilute gas of interstellar space to the emergence of habitable worlds.

6.1 The continuum of molecular complexity: from molecular clouds to discs

The early phases of this work focused on the cosmic chemical cycle and the transition of volatile species from pristine interstellar clouds into the structured environment of protoplanetary discs. At first glance, investigating whether a carbon monoxide ice layer is thoroughly mixed with methanol or physically segregated into a distinct apolar phase appears to be a purely technical question of solid-state physics. We used mathematical tools like the Levenberg-Marquardt algorithm to untangle these micro-environments, mapping how molecules can assemble at the very low temperatures in space. However, this structural stratification is the fundamental starting point for prebiotic evolution. The physical architecture of an ice mantle directly dictates its chemical destiny under energetic processing. When a protoplanetary disc undergoes vertical mixing, ices are lofted from the cold, shielded midplane into upper layers irradiated by stellar ultraviolet light and X-rays. If carbon monoxide remains trapped within a polar water-ice matrix, it undergoes fundamentally different chemical pathways than if it rests in a pure, apolar phase. The preservation of these molecular micro-environments, whether inherited directly from the interstellar medium or reprocessed by the young star, determines the efficiency with which simple precursors are synthesized into complex organic molecules like formaldehyde, formic acid, and alcohols. These are the identical building blocks that are eventually incorporated into planetesimals, comets, and asteroidal bodies. By mapping the precise lineshapes of accreting volatiles, we are not just validating astronomical observations; we are reconstructing the chemical inventory available to terrestrial planets during their formation.

6.2 Energetic triggers and the synthesis of prebiotic structure

In our experimental simulations using the LIFE and IEPS facilities, we subjected interstellar ice analogues to vacuum-ultraviolet lamps, X-ray sources, and electron guns. These energetic sources break stable chemical bonds, creating a cascade of reactive radicals and secondary low-energy electrons within the ice lattice. From a physical standpoint, we carefully monitored the cross-sections, stopping powers, and thermalization cascades that govern how energy is distributed through these cryogenic solids. The broader astrobiological implications of these experiments are profound. Space is an environment characterized by extreme kinetic inhibition; without external energetic triggers, the chemistry of life would stall before it could begin. Ionizing radiation and ultraviolet photons act as the cosmic engines that overcome these activation barriers. Our laboratory observations tracked the direct synthesis of species such as formaldehyde and formic acid from simple mixtures of water and carbon monoxide. These are not merely interstellar curiosities; they are indispensable precursors to the formose reaction and amino acid synthesis. Formaldehyde serves as the critical stepstone toward ribose, the sugar backbone of RNA, while formic acid is a vital intermediate in primordial metabolic pathways.

Consequently, studying the non-equilibrium chemistry of irradiated ices is an investigation into the universal mechanism that generates the foundational materials of genetic and metabolic architecture across the cosmos.

6.3 The phosphorus bottleneck and the habitability of ocean worlds

The final chapter of this exploratory path shifted our focus from the diffuse regions of star formation to the inner boundaries of our solar system, specifically the geochemical landscape of Saturn's icy moon, Enceladus. Here, the astrobiological objective becomes explicitly apparent. Enceladus possesses a global subsurface liquid ocean, rich in organic molecules and driven by hydrothermal activity, making it one of the prime targets in the modern search for extraterrestrial life. However, life as we know it cannot exist on liquid water and carbon compounds alone; it strictly requires the biogenic elements carbon, hydrogen, nitrogen, oxygen, phosphorus, and sulfur. Among these elements, phosphorus represents a notoriously difficult prebiotic bottleneck. On Earth, and presumably on other water worlds, phosphorus is heavily sequestered within highly insoluble, unreactive inorganic minerals, such as apatite or orthophosphate salts. The transition from this locked, inert state to a bioavailable form, capable of building adenosine triphosphate, nucleic acids, and phospholipid cellular membranes, is a primary missing link in origin-of-life models. Our research addressed this question by simulating the interfacial chemistry between sodium orthophosphate substrates and overlying water-ice sheets under magnetospheric electron bombardment. The technical results revealed a fascinating mechanism of direct "chemical cross-talk" at the solid-state interface. High-energy electron radiolysis fragments the water molecules, liberating highly mobile protons and hydrogen radicals. The underlying phosphate matrix actively captures these fragments, driving the efficient protonation of the salt into hydrogen phosphate and potentially opening pathways toward more reactive, reduced phosphorus species. When we analyze this process, we are evaluating the operational efficiency of a planetary-scale chemical reactor. If magnetospheric radiation can continuously alter and activate phosphorus on the surface of an icy moon, subsequent impact gardening and cryovolcanic cycling can transport these bioavailable nutrients back down into the subsurface ocean. This experimental phase directly tests whether the environmental conditions of the outer solar system can overcome the phosphorus bottleneck, establishing the necessary conditions for prebiotic chemistry to transition into biology in environments far removed from the warmth of the Sun.

6.4 Final perspectives: the unbroken thread

Ultimately, astrochemistry is defined by its multidisciplinary nature. It demands an appreciation for quantum mechanical interactions, the precision engineering of ultra-high vacuum chambers, the mathematical constraints of astronomical telescope datasets, and the vast geological timescales of planetary evolution. It is easy for an investigator to become entirely absorbed by the isolated complexities of these individual fields. Yet, as shown throughout the chapters of this thesis, an unbroken prebiotic thread connects them all. We study the micro-scale stratification of carbon monoxide in a disc because it influences the macro-scale delivery of volatile carbon to a young planet. We study the cross-sections of electron-impact ionization in water ice because those identical electrons drive the activation of life-limiting nutrients on an ocean world. Every technical milestone achieved in the laboratory is a step toward mapping the cosmic history of our own origins. We investigate the physics and chemistry of cosmic ices not merely to understand the cold, silent spaces between the stars, but to decipher the universal laws that allowed the universe to awaken, contemplate itself, and give rise to life.

Bibliography

Aboulahris M., Chennaoui Aoudjehane H., Rochette P., Gattacceca J., Jull A. J. T., Laridhi Ouazaa N., Folco L. and Buhl S., 2019, *Characteristics of the Sahara as a meteorite recovery surface*, Meteorit. Planet. Sci., 54, 2908.

Amelin Y. and Ireland T. R., 2013, *Dating the Oldest Rocks and Minerals in the Solar System*, Elements, 9, 39.

Baino F. and Kargozar S., 2022, *Bioactive Glasses and Glass-Ceramics: Fundamentals and Applications*, John Wiley & Sons.

Banach M. and Makara A., 2011, *Thermal decomposition of sodium phosphates*, J. Chem. Eng. Data, 56, 3095.

Barone V., Latouche C., Skouteris D., Vazart F., Balucani N., Ceccarelli C. and Lefloch B., 2015, *Gas-phase formation of the prebiotic molecule formamide: insights from new quantum computations*, MNRAS, 453, L31.

Belenkaya E. S., Alexeev I. I., Kalegaev V. V. and Blokhina M. S., 2006, *Definition of Saturn's magnetospheric model parameters for the Pioneer 11 flyby*, Ann. Geophys., 24, 1145.

Bellamy L. J. F. C., 2013, *The Infra-red Spectra of Complex Molecules*, Springer Science & Business Media.

Bennett C. J., Hama T., Kim Y. S., Kawasaki M. and Kaiser R. I., 2010, *Laboratory studies on the formation of formic acid (HCOOH) in interstellar and cometary ices*, ApJ, 727, 27.

Bergantini A., Pilling S., Nair B. G., Mason N. J. and Fraser H. J., 2014, *Processing of analogues of plume fallout in cold regions of Enceladus by energetic electrons*, A&A, 570, A120.

Bergner J. B. and Ciesla F., 2021, *Ice Inheritance in Dynamical Disk Models*, ApJ, 919, 45.

Bergner J. B., Sturm J. A., Piacentino E. L., et al., 2024, *ApJ*, 975, 166.

Boogert A. C., Gerakines P. A. and Whittet D. C. B., 2015, *Observations of the icy universe*, ARA&A, 53, 541.

Bouilloud M., Fray N., Bénilan Y., Cottin H., Gazeau M.-C. and Jolly A., 2015, *Bibliographic review and new measurements of the infrared band strengths of pure molecules at 25 K: H_2O, CO_2, CO, CH_4, NH_3, CH_3OH, HCOOH and H_2CO*, MNRAS, 451, 2145.

Bouwman J., Ludwig W., Awad Z., Öberg K. I., Fuchs G. W., van Dishoeck E. F. and Linnartz H., 2007, *Band profiles and band strengths in mixed H_2O:CO ices*, A&A, 476, 995.

van Broekhuizen F. A., Groot I. M. N., Fraser H. J., van Dishoeck E. F. and Schlemmer S., 2006, *Infrared spectroscopy of solid CO-CO_2 mixtures and layers*, A&A, 451, 723.

Cecchi-Pestellini C. and Aiello S., 1992, *Cosmic ray induced photons in dense interstellar clouds*, MNRAS, 258, 125.

Cecchi-Pestellini C., Iatì M. A. and Williams D. A., 2012, *The nature of interstellar dust as revealed by light scattering*, JQSRT, 113, 2310.

Chen Y.-J., Chuang K.-J., Muñoz Caro G. M., Nuevo M., Chu C.-C., Yih T.-S., Ip W.-H. and Wu C.-Y. R., 2014, *Vacuum Ultraviolet Emission Spectrum Measurement of a Microwave-discharge Hydrogen-flow Lamp in Several Configurations: Application to Photodesorption of CO Ice*, ApJ, 781, 15.

Chuang K.-J., Fedoseev G., Ioppolo S., van Dishoeck E. F. and Linnartz H., 2016, *H-atom addition and abstraction reactions in mixed CO, H_2CO and CH_3OH ices - an extended view on complex organic molecule formation*, MNRAS, 455, 1702.

Ciaravella A., Chen Y.-J., Cecchi-Pestellini C., Jiménez-Escobar A., Muñoz Caro G. M., Chuang K.-J. and Huang C.-H., 2016, *Chemical Evolution of a CO Ice Induced by Soft X-Rays*, ApJ, 819, 38.

Ciaravella A., Jiménez-Escobar A., Cosentino G., et al., 2018, *Chemical Evolution of Interstellar Methanol Ice Analogs upon Ultraviolet Irradiation: The Role of the Substrate*, ApJ, 858, 35.

Ciaravella A., Muñoz Caro G. M., Jiménez-Escobar A., Cecchi-Pestellini C., Hsiao L.-C., Huang C.-H. and Chen Y.-J., 2020, *X-ray processing of a realistic ice mantle can explain the gas abundances in protoplanetary disks*, Proc. Natl. Acad. Sci., 117, 16149.

Coates J., 2000, *Interpretation of infrared spectra, a practical approach*, Encycl. Anal. Chem., 12, 10815.

Cockell C. S., Bush T., Bryce C., et al., 2016, *Habitability: A Review*, Astrobiology, 16, 89.

Collings M. P., Anderson M. A., Chen R., Dever J. W., Viti S., Williams D. A. and McCoustra M. R. S., 2004, *A laboratory survey of the thermal desorption of astrophysically relevant molecules*, MNRAS, 354, 1133.

Collings M. P., Dever J. W. and McCoustra M. R. S., 2014, *The interaction of carbon monoxide with model astrophysical surfaces*, Phys. Chem. Chem. Phys., 16, 3479.

Cooke I. R., Fayolle E. C. and Öberg K. I., 2016, *ApJ*, 832, 5.

Cooper P. D., Moore M. H. and Hudson R. L., 2008, *Radiation chemistry of H_2O + O_2 ices*, Icarus, 194, 379.

Cottin H., Gazeau M.-C., Doussin J.-F. and Raulin F., 2000, *J. Photochem. Photobiol. A*, 135, 53.

Cruz-Diaz G. A., Muñoz Caro G. M., Chen Y.-J. and Yih T.-S., 2014, *Vacuum-UV spectroscopy of interstellar ice analogs. I. Absorption cross-sections of polar-ice molecules*, A&A, 562, A119.

Cruz-Diaz G. A., Muñoz Caro G. M., Chen Y.-J. and Yih T.-S., 2014, *Vacuum-UV spectroscopy of interstellar ice analogs. II. Absorption cross-sections of nonpolar ice molecules*, A&A, 562, A120.

Cuppen H. M., Walsh C., Lamberts T., Semenov D., Garrod R. T., Penteado E. M. and Ioppolo S., 2017, *Grain Surface Models and Data for Astrochemistry*, Space Sci. Rev., 212, 1.

Cuppen H. M., Linnartz H. and Ioppolo S., 2024, *Laboratory and Computational Studies of Interstellar Ices*, ARA&A, 62, 243.

Daranlot J., Hincelin U., Bergeat A., Costes M., Loison J.-C., Wakelam V. and Hickson K. M., 2012, *Elemental nitrogen partitioning in dense interstellar clouds*, Proc. Natl. Acad. Sci., 109, 10233.

Dartois E., Noble J. A., Ysard N., Demyk K. and Chabot M., 2022, *Influence of grain growth on CO_2 ice spectroscopic profiles. Modelling for dense cores and disks*, A&A, 666, A153.

Dawes A., Mason N. J. and Fraser H. J., 2016, *Using the C-O stretch to unravel the nature of hydrogen bonding in low-temperature solid methanol-water condensates*, Phys. Chem. Chem. Phys., 18, 1245.

d'Hendecourt L. B. and Allamandola L. J., 1986, *Time dependent chemistry in dense molecular clouds. III. Infrared band cross sections of molecules in the solid state at 10K*, A&AS, 64, 453.

Draine B. T., 2011, *Physics of the Interstellar and Intergalactic Medium*, Princeton University Press, Princeton and Oxford.

Ehrenfreund P., Boogert A. C. A., Gerakines P. A., Tielens A. G. G. M. and van Dishoeck E. F., 1997, *Infrared spectroscopy of interstellar apolar ice analogs*, A&A, 328, 649.

Ekou T., Ekou L., Lafaye G., Especel C. and Marécot P., 2016, *Characterization of Rh-Ge/TiO_2 and Pt-Ge/TiO_2 Catalysts by Fourier Transform Infrared Spectroscopy of Adsorbed CO*, Res. Rev. J. Chem.

El-Meliegy E. and Van Noort R., 2011, *Glasses and Glass Ceramics for Medical Applications*, Springer Science & Business Media.

Escribano B., del Burgo Olivares C., Carrascosa H., Martín-Doménech R., Gómez P. C. and Muñoz Caro G. M., 2025, *Estimating the infrared band strengths of amorphous interstellar ice analogues using density functional theory*, A&A, 701, A146.

Escribano R. M., Muñoz Caro G. M., Cruz-Diaz G. A., Rodriguez-Lazcano Y. and Mate B., 2013, *Proceedings of the National Academy of Science*, 110, 12899.

Fraser H. J., Collings M. P., Dever J. W. and McCoustra M. R. S., 2004, *Using laboratory studies of CO-H_2O ices to understand the non-detection of a 2152cm^{-1} (4.647μm) band in the spectra of interstellar ices*, MNRAS, 353, 59.

Gail H.-P. and Sedlmayr E., 2013, *Physics and Chemistry of Circumstellar Dust Shells*, Cambridge University Press, Cambridge.

Germain A., Tinacci L., Pantaleone S., Ceccarelli C. and Ugliengo P., 2022, *Computer Generated Realistic Interstellar Icy Grain Models: Physicochemical Properties and Interaction with NH_3*, ACS Earth Space Chem., 6, 1286.

Gorai P., Sil M., Das A. et al., 2020, *Systematic Study on the Absorption Features of Interstellar Ices in the Presence of Impurities*, ACS Earth Space Chem., 4, 920.

Gould R. J. and Salpeter E. E., 1963, *The Interstellar Abundance of the Hydrogen Molecule. I. Basic Processes.*, ApJ, 138, 393.

Gunter G. C., Craciun R., Tam M. S., Jackson J. E. and Miller D. J., 1996, *FTIR and ^{31}P-NMR spectroscopic analyses of surface species in phosphate-catalyzed lactic acid conversion*, J. Catal., 164, 207.

He J., Acharyya K. and Vidali G., 2016, *Binding Energy of Molecules on Water Ice: Laboratory Measurements and Modeling*, ApJ, 825, 89.

He J., Toriello F. E., Emtiaz S. M., Henning T. and Vidali G., 2021, *Phase Transition of Interstellar CO Ice*, ApJL, 915, L23.

He J., Perotti G., Emtiaz S. M., Toriello F. E., Boogert A., Henning T. and Vidali G., 2022, *Ammonia, carbon dioxide, and the non-detection of the 2152 cm^{-1} CO band*, A&A, 668, A76.

Herbst E. and Klemperer W., 1973, *The Formation and Depletion of Molecules in Dense Interstellar Clouds*, ApJ, 185, 505.

Herbst E., Vidali G. and Ceccarelli C., 2020, *Complex Organic Molecules (COMs) in Star-Forming Regions: A Virtual Special Issue*, ACS Earth Space Chem., 4, 488.

Huang C.-H., 2019, *Chemical Evolution of Interstellar Ice Mantles Under X-rays and Electrons Processing*, PhD thesis, National Central University, Jhongli District, Taoyuan City (Taiwan).

Huang C.-H., Ciaravella A., Cecchi-Pestellini C., Jiménez-Escobar A., Hsiao L.-C., Huang C.-C., Chen P.-C., Sie N.-E. and Chen Y.-J., 2020, *Effects of 150-1000 eV Electron Impacts on Pure Carbon Monoxide Ices Using the Interstellar Energetic-Process System (IEPS)*, ApJ, 889, 57.

Hudson R. L. and Moore M. H., 2001, *Radiation chemical alterations in solar system ices: An overview*, J. Geophys. Res., 106, 33275.

Hudson R. L., Gerakines P. A. and Ferrante R. F., 2018, *IR spectra and properties of solid acetone, an interstellar and cometary molecule*, Spectrochim. Acta A, 193, 33.

Ioppolo S., Cuppen H. M., Romanzin C., van Dishoeck E. F. and Linnartz H., 2008, *Laboratory Evidence for Efficient Water Formation in Interstellar Ices*, ApJ, 686, 1474.

Ivlev A. V., Giuliano B. M., Juhász Z., et al., 2023, *Bombardment of CO Ice by Cosmic Rays. I. Experimental Insights into the Microphysics of Molecule Destruction and Sputtering*, ApJ, 944, 181.

Jha P. K., Pandey O. P. and Singh K., 2015, *FTIR spectral analysis and mechanical properties of sodium phosphate glass–ceramics*, J. Mol. Struct., 1083, 278.

Jastrzebski W., Sitarz M., Rokita M. and Bulat K., 2011, *Infrared spectroscopy of different phosphate structures*, Spectrochim. Acta A, 79, 722.

Jiang G. J., Person W. B. and Brown K. G., 1975, *Absolute infrared intensities and band shapes in pure solid CO and CO in some solid matrices*, J. Chem. Phys., 62, 1201.

Jiménez-Escobar A., Ciaravella A., Cecchi-Pestellini C. et al., 2022, *X-Ray-induced Diffusion and Mixing in Layered Astrophysical Ices*, ApJ, 926, 176.

Jiménez-Escobar A., Ciaravella A., Cecchi-Pestellini C., Sie N.-E., Lee C.-Y., Huang C.-H., Muñoz Caro G. M. and Chen Y.-J., 2024, *Laboratory simulations of ice growth in space: An expected nonuniform ice mantle composition*, A&A, 686, A39.

Johnston J. M., 2013, *Sodium phosphate solubility in electrolyte solutions at elevated temperatures: impact on Hanford waste tank chemistry*, PhD thesis, Washington State University.

Jonusas M., Leroux K. and Krim L., 2020, *N + H surface reaction under interstellar conditions: Does the $NH/NH_2/NH_3$ distribution depend on N/H ratio?*, J. Mol. Struct., 1220, 128736.

Karteyeva V., Nakibov R., Petrashkevich I., Medvedev M. and Vasyunin A., 2026, *Identification of solid N_2O in interstellar ices using open JWST data*, A&A, 706, L4.

Leemker M., Tobin J. J., Facchini S., Curone P., Booth A. S., Furuya K. and van't Hoff M. L. R., 2025, *Pristine ices in a planet-forming disk revealed by heavy water*, Nature Astronomy, 9, 1486.

Li J., Gudipati M. S., Mishra Y. N., Liang M.-C. and Yung Y. L., 2022, *Oxidant generation in the ice under electron irradiation: Simulation and application to Europa*, Icarus, 373, 114760.

Lingam M. and Loeb A., 2018, *Is extraterrestrial life suppressed on subsurface ocean worlds due to the paucity of bioessential elements?*, AJ, 156, 151.

Lippok N., Launhardt R., Semenov D., Stutz A. M., Balog Z., Henning Th., Krause O., Linz H., Nielbock M., Pavlyuchenkov Ya. N., Schmalzl M., Schmiedeke A. and Bieging J. H., 2013, *Gas-phase CO depletion and N_2H^+ abundances in starless cores*, A&A, 560, A41.

Lo J.-I., Lu H.-C., Hung W.-H., Ogilvie J. F. and Cheng B.-M., 2022, *Visible, near-infrared and mid-infrared spectra of solid O_2 at 6–33 K*, MNRAS, 514, 2815.

Loeffler M. J., Teolis B. D. and Baragiola R. A., 2006, *A model study of the thermal evolution of astrophysical ices*, ApJ, 639, L103.

Loeffler M. J., Raut U., Vidal R. A., Baragiola R. A. and Carlson R. W., 2006, *Synthesis of hydrogen peroxide in water ice by ion irradiation*, Icarus, 180, 265.

McClure M. K., Rocha W. R. M., Pontoppidan K. M. et al., 2023, *An Ice Age JWST inventory of dense molecular cloud ices*, Nature Astronomy, 7, 431.

McGuire B. A., 2022, *2021 Census of Interstellar, Circumstellar, Extragalactic, Protoplanetary Disk, and Exoplanetary Molecules*, ApJS, 259, 30.

Meisner J., Lamberts T. and Kästner J., 2017, *Atom Tunneling in the Water Formation Reaction H_2 + OH → H_2O + H on an Ice Surface*, ACS Earth Space Chem., 1, 399.

Mejía C., De Barros A. L. F., Rothard H., Boduch P. and Da Silveira E. F., 2022, *Swift heavy ions irradiation of water ice at different temperatures: hydrogen peroxide and ozone synthesis and sputtering yield*, MNRAS, 514, 3789.

Mohan Babu M., Syam Prasad P., Venkateswara Rao P., Hima Bindu S., Prasad A., Veeraiah N. and Özcan M., 2020, *Influence of ZrO_2 addition on structural and biological activity of phosphate glasses for bone regeneration*, Materials, 13, 4058.

Molpeceres G., Enrique-Romero J. and Aikawa Y., 2023, *Cracking the puzzle of CO_2 formation on interstellar ices. Quantum chemical and kinetic study of the CO + OH → CO_2 + H reaction*, A&A, 677, A39.

Molpeceres G., Enrique-Romero J., Ishibashi A., Oba Y., Hidaka H., Lamberts T., Aikawa Y. and Watanabe N., 2025, *Hydrogenation of HOCO and formation of interstellar CO_2: a not so straightforward relation*, MNRAS, 538, 1565.

Mokrane H., Chaabouni H., Accolla M., Congiu E., Dulieu F., Chehrouri M. and Lemaire J. L., 2009, *Experimental Evidence for Water Formation Via Ozone Hydrogenation on Dust Grains at 10 K*, ApJL, 705, L195.

Morbidelli A., Bitsch B., Crida A., Gounelle M., Guillot T., Jacobson S., Johansen A., Lambrechts M. and Lega E., 2016, *Fossilized condensation lines in the Solar System protoplanetary disk*, Icarus, 267, 368.

Mousis O., Petetin C., Benest Couzinou T., Schneeberger A. and Bennacer Y., 2026, *Formation and Survival of Complex Organic Molecules in the Jovian Circumplanetary Disk*, PSJ, 7, 41.

Moustafa Y. M. and El-Egili K., 1998, *Infrared spectra of sodium phosphate glasses*, J. Non-Cryst. Solids, 240, 144.

Muñoz Caro G. M., Jiménez-Escobar A., Martín-Gago Á, et al., 2010, *A&A*, 522, A108.

Muñoz Caro G. M., Carrascosa de Lucas H. and Martín-Doménech R., 2025, *Photochemistry of interstellar ice forming complex organic molecules*, Nat. Rev. Chem., 9, 537.

Müller B., Giuliano B. M., Bizzocchi L., Vasyunin A. I. and Caselli P., 2018, *O_2 signature in thin and thick O_2-H_2O ices*, A&A, 620, A46.

Müller B., Giuliano B. M. and Goto M., 2021, *Spectroscopic measurements of CH_3OH in layered and mixed interstellar ice analogues*, A&A, 652, A126.

Nakamoto K., 2009, *Infrared and Raman Spectra of Inorganic and Coordination Compounds, Part B: Applications in Coordination, Organometallic, and Bioinorganic Chemistry*, John Wiley & Sons.

Nazari P., 2025, *Overview of complex organic molecule observations in protostellar systems*, arXiv:2508.15771.

Noble J. A., Fraser H. J., Smith Z. L. et al., 2024, *Detection of the elusive dangling OH ice features at 2.7 μm in Chamaeleon I with JWST NIRCam*, Nature Astron., 8, 1169.

Oba Y., Watanabe N., Kouchi A., Hama T. and Pirronello V., 2010, *Experimental Study of CO_2 Formation by Surface Reactions of Non-energetic OH Radicals with CO Molecules*, ApJL, 712, L174.

Öberg K. I., Boogert A. C. A., Pontoppidan K. M. et al., 2011, *The Spitzer Ice Legacy: Ice Evolution from Cores to Protostars*, ApJ, 740, 109.

Öberg K. I., 2016, *Photochemistry and Astrochemistry: Photochemical Pathways to Interstellar Complex Organic Molecules*, Chem. Rev., 116, 9631.

Ostrowski D. R. and Bryson K., 2016, *Physical Property Comparison of Meteorite Classes*, in AGU Fall Meeting Abstracts, NH13A-1752.

Palumbo M. E., Baratta G. A., Collings M. P. and McCoustra M. R. S., 2006, *The profile of the 2140 cm^{-1} solid CO band on different substrates*, Phys. Chem. Chem. Phys., 8, 279.

Park J.-Y. and Woon D. E., 2006, *Theoretical Modeling of Formic Acid (HCOOH), Formate ($HCOO^-$), and Ammonium (NH_4^+) Vibrational Spectra in Astrophysical Ices*, ApJ, 648, 1285.

Pérez-Sánchez G., González-Salgado D., Piñeiro M. M. and Vega C., 2013, *Fluid-solid equilibrium of carbon dioxide as obtained from computer simulations of several popular potential models: The role of the quadrupole*, J. Chem. Phys., 138, 084506.

Pontoppidan K. M., Fraser H. J., Dartois E., Thi W.-F., van Dishoeck E. F., Boogert A. C. A., d'Hendecourt L., Tielens A. G. G. M. and Bisschop S. E., 2003, *A 3-5 μm VLT spectroscopic survey of embedded young low mass stars I. Structure of the CO ice*, A&A, 408, 981.

Porco C. C., Dones L. and Mitchell C., 2017, *Could It Be Snowing Microbes on Enceladus? Assessing Conditions in Its Plume and Implications for Future Missions*, Astrobiology, 17, 876.

Postberg F., Sekine Y., Klenner F., et al., 2023, *Detection of phosphates originating from Enceladus's ocean*, Nature, 618, 489.

Prasad S. S. and Tarafdar S. P., 1983, *UV radiation field inside dense clouds - Its possible existence and chemical implications*, ApJ, 267, 603.

Puzzarini C. and Alessandrini S., 2026, *Chemistry in Extreme Environments: The Mystery of Molecular Complexity in Space*, ACS Cent Sci., 12, 174.

Qasim D., Chuang K.-J., Fedoseev G., Ioppolo S., Boogert A. C. A. and Linnartz H., 2018, *Formation of interstellar methanol ice prior to the heavy CO freeze-out stage*, A&A, 612, A83.

Qasim D., Fedoseev G., Chuang K.-J., He J., Ioppolo S., van Dishoeck E. F. and Linnartz H., 2020, *An experimental study of the surface formation of methane in interstellar molecular clouds*, Nature Astronomy, 4, 781–785.

Redondo P., Pauzat F., Ellinger Y. and Markovits A., 2020, *Reconstruction of water ice: the neglected process OH + OH → H_2O + O*, A&A, 638, A125.

Richards G., Rácz R., Kovács S. T. S., Pearson V., Morgan G., Patel M. R., Sheridan S., Mifsud D. V., Sulik B., Biri S., Mason N. J., McCullough R. W. and Juhász Z., 2025, *Water-group ion irradiation studies of Enceladus ice analogues: Can radiolysis account for material in and around the south polar plume?*, Planet. Space Sci., 266, 106179.

Rocha W. R. M., van Dishoeck E. F., Ressler M. E. et al., 2024, *JWST Observations of Young protoStars (JOYS+): Detecting icy complex organic molecules and ions. I. CH_4, SO_2, $HCOO^-$, OCN^-, H_2CO, HCOOH, CH_3CH_2OH, CH_3CHO, CH_3OCHO, and CH_3COOH*, A&A, 683, A124.

Sakpal T., Kumar A., Aman Z. M. and Kumar R., 2019, *Carbon dioxide capture from flue gas using tri-sodium phosphate as an effective sorbent*, Energies, 12, 2889.

Sandford S. A., Allamandola L. J., Tielens A. G. G. M. and Valero G. J., 1988, *Laboratory Studies of the Infrared Spectral Properties of CO in Astrophysical Ices*, ApJ, 329, 498.

Santos J. C., Chuang K.-J., Lamberts T., Fedoseev G., Ioppolo S. and Linnartz H., 2022, *First Experimental Confirmation of the CH_3O + H_2CO → CH_3OH + HCO Reaction: Expanding the CH_3OH Formation Mechanism in Interstellar Ices*, ApJL, 931, L33.

Schmidt F., Borrmann T., Mues M. P., Benter S., Swiderek P. and Bredehöft J. H., 2022, *Mechanisms of Electron-Induced Chemistry in Molecular Ices*, Atoms, 10, 25.

Scibelli S., Shirley Y., Megías A. and Jiménez-Serra I., 2024, *Survey of complex organic molecules in starless and pre-stellar cores in the Perseus molecular cloud*, MNRAS, 533, 4104.

Seki T., Chiang K.-Y., Yu C.-C., Yu X., Okuno M., Hunger J., Nagata Y. and Bonn M., 2020, *The bending mode of water: a powerful probe for hydrogen bond structure of aqueous systems*, J. Phys. Chem. Lett., 11, 8459.

Sturm J. A., McClure M. K., Beck T. L. et al., 2023, *A JWST inventory of protoplanetary disk ices. The edge-on protoplanetary disk HH 48 NE, seen with the Ice Age ERS program*, A&A, 679, A138.

Swain T., 2018, *Synthesis, characterization and thermal property of {$Cu_3(PO_4)_2{\cdot}2H_2O$; Na_3PO_4; $NaHSO_4{\cdot}H_2O$}*, Sol. Energy, 159, 369.

Tao J., 2013, *FTIR and Raman studies of structure and bonding in mineral and organic–mineral composites*, in *Methods in Enzymology*, Vol. 532, Elsevier, pp. 533–556.

Tarte P., 1967, *Infra-red spectra of inorganic aluminates and characteristic vibrational frequencies of AlO_4 tetrahedra and AlO_6 octahedra*, Spectrochim. Acta A, 23, 2127.

Teolis B. D., Perry M. E., Hansen C. J., Waite J. H., Porco C. C., Spencer J. R. and Howett C. J. A., 2017, *Enceladus Plume Structure and Time Variability: Comparison of Cassini Observations*, Astrobiology, 17, 926.

Terwisscha van Scheltinga J., Ligterink N. F. W., Bosman A. D., Hogerheijde M. R. and Linnartz H., 2022, *The formation of CO_2 through consumption of gas-phase CO on vacuum-UV irradiated water ice*, A&A, 666, A35.

Tielens A. G. G. M. and Hagen W., 1982, *Model calculations of the molecular composition of interstellar grain mantles*, A&A, 114, 245–260.

Tielens A. G. G. M., Tokunaga A. T., Geballe T. R. and Baas F., 1991, *Interstellar Solid CO: Polar and Nonpolar Interstellar Ices*, ApJ, 381, 181.

Trivedi M. K., Branton A., Trivedi D., Nayak G., Bairwa K. and Jana S., 2015, *Spectroscopic characterization of disodium hydrogen orthophosphate and sodium nitrate after biofield treatment*, J. Chromatogr. Sep. Tech., 6.

van Dishoeck E. F., Tychoniec L., Rocha W. R. M. et al., 2025, *JWST Observations of Young protoStars (JOYS): Overview of program and early results*, A&A, 699, A361.

Williams D. A. and Cecchi-Pestellini C., 2015, *The Chemistry of Cosmic Dust*, Royal Society of Chemistry, Cambridge.

Wang J., Sun B.-J., Bergantini A., Wang Z., McAnally M., Marks J. H., Chang A. H. H., Eckhardt A. K. and Kaiser R. I., 2026, *Non-equilibrium preparation of (E)-phosphinimine (HPNH, X^1A') – a precursor to prebiotic phosphorylating agents*, Chem. Sci., 17, 9446.

Williams D. A., Hartquist T. W., Rawlings J. M. C., Cecchi-Pestellini C. and Viti S., 2017, *Dynamical Astrochemistry*, Royal Society of Chemistry, Cambridge.

Xu S., Cheema A. I., Zhang Y. and Dong B., 2024, *Phosphate-Based Binders for Stabilization and Solidification of Soils Contaminated with Multiple Heavy Metals: Mechanisms and Efficacy Evaluation*, Preprints.

Yang C., Lin K. and Chang J., 2015, *A simple way to synthesize 3D hierarchical HAp porous microspheres with sustained drug release*, Ceram. Int., 41, 11153.

Zamirri L., Casassa S., Rimola A., Segado-Centellas M., Ceccarelli C. and Ugliengo P., 2018, *IR spectral fingerprint of carbon monoxide in interstellar water-ice models*, MNRAS, 480, 1427.

Zarif M. E., Yehia-Alexe S. A., Bita B., Negut I., Locovei C. and Groza A., 2022, *Calcium phosphates–chitosan composite layers obtained by combining radio-frequency magnetron sputtering and matrix-assisted pulsed laser evaporation techniques*, Polymers, 14, 5241.